

Globally time-reversible fluid simulations with smoothed particle hydrodynamics [☆]

Ondřej Kincl ^{*}, Michal Pavelka

ARTICLE INFO

Article history:

Received 2 May 2022

Received in revised form 1 November 2022

Accepted 7 November 2022

Available online 21 November 2022

Keywords:

SPH

Reversibility

Symplectic integrator

Stability

Entropy

ABSTRACT

This paper describes an energy-preserving and globally time-reversible code for weakly compressible smoothed particle hydrodynamics (SPH). We do not add any additional dynamics to the Monaghan's original SPH scheme at the level of ordinary differential equation, but we show how to discretize the equations by using a corrected expression for density and by invoking a symplectic integrator. Moreover, to achieve the global-in-time reversibility, we have to correct the initial state, implement a conservative fluid-wall interaction, and use the fixed-point arithmetic. Although the numerical scheme is reversible globally in time (solvable backwards in time while recovering the initial conditions), we observe thermalization of the particle velocities and growth of the Boltzmann entropy. In other words, when we do not see all the possible details, as in the Boltzmann entropy, which depends only on the one-particle distribution function, we observe the emergence of the second law of thermodynamics (irreversible behavior) from purely reversible dynamics.

© 2022 Elsevier B.V. All rights reserved.

Contents

| | |
|---|----|
| 1. Introduction | 1 |
| 2. WCSPH for inviscid fluids | 2 |
| 3. Treatment of free surfaces | 3 |
| 3.1. Solving the equation for ρ_a with an appropriate integration constant | 3 |
| 3.2. Initial state correction (ISC) | 3 |
| 3.3. Wall modelling | 4 |
| 4. Symplectic integrator and fixed-point arithmetic | 5 |
| 5. Dissipativity vs. decrease in mechanical energy | 6 |
| 6. Emergence of the second law of thermodynamics | 8 |
| 7. Conclusion | 9 |
| Declaration of competing interest | 9 |
| Data availability | 9 |
| Acknowledgements | 9 |
| Appendix A. Gresho vortex benchmark | 9 |
| Appendix B. The Maxwell-Boltzmann entropy | 10 |
| B.1. The reduced Boltzmann entropy in terms of the Maxwell-Boltzmann distribution | 10 |
| B.2. Equilibrium Boltzmann entropy | 11 |
| Appendix C. Energy budget in the dam-break simulation | 12 |
| References | 12 |

1. Introduction

The original smoothed particle hydrodynamics (SPH) scheme, now called weakly compressible SPH (WCSPH), was developed in 1970s by R. Gingold and J. Monaghan [1]. The scheme used the

[☆] The review of this paper was arranged by Prof. David W. Walker.

^{*} Corresponding author.

E-mail address: ondrej.kincl@gmail.com (O. Kincl).

leap-frog time integration and relied on an artificial term stabilizing the fluid in the presence of shocks. Many other stabilization strategies were conceived. In the δ -SPH method [2], diffusion terms are added to the continuity equation, and methods based on Riemann solvers [3]. These approaches often provide results in reasonable agreement with experimental data or other numerical methods. Unfortunately, they often come at the cost of increased complexity and necessity to fine-tune additional numerical parameters [4].¹ Failure in such fine-tuning can result in unrealistic dissipation, or large energy oscillations unless a convenient limiter is used [7].

Another problem of SPH (especially in solid mechanics) is the so called tensile instability, where simulations are unable to withstand a dilation of volume (leading to clamping of particles inside the solid body) [8]. A solution is to use the Lagrangian kernels, which depend on the Lagrangian distances between the particles instead of the Eulerian distances [9][10]. The price to pay is that the Lagrangian kernels become too distorted for large deformations, which can be avoided by switching between the Lagrangian and Eulerian iterations [11]. In this manuscript, we do not consider solid mechanics, which is why we can work with the standard Eulerian kernels.

Novelty of this manuscript lies mainly (to our best knowledge) in the global reversibility of the SPH scheme and in the thermodynamic interpretation of the results (growth of Boltzmann entropy despite the reversibility). To achieve the global reversibility, we had to formulate SPH as a symplectic system, to correct the way density is typically treated, to use the fixed-point arithmetic, and to implement a conservative wall-fluid interaction. Each of these steps is necessary for the global reversibility. The second main point lies in the thermodynamic interpretation of the emergence of irreversibility that we observe. Although the underlying dynamics is reversible and the Liouville entropy (that takes into account positions of all particles) does not grow, the Boltzmann entropy (that no longer takes into account the individual particles) grows. This emergence of the second law of thermodynamics is caused by the information loss between the complete Liouville description and the averaged Boltzmann description of the particle system.

Although the reversible (non-dissipative) terms in the SPH simulations typically do not alter the total energy appreciably, they can cause a sort of irreversibility. WCSPH simulations contain the evolution equation for the discrete density and can also contain an evolution equation for particle energy, but if the underlying numerical integrator is not symplectic, it changes the phase volume, which causes irreversible evolution of the distribution function [12,13]. In this manuscript, we construct a globally reversible symplectic SPH scheme, which can be used also for backward simulations and leads to the initial state of the particles, and thus it does not introduce numerical dissipation in the above sense.

The symplecticity can be achieved by a particular way to calculate the pressure. There are essentially two different ways, how pressure can be calculated in WCSPH [14]. A commonly used approach is to update the density iteratively, using the velocities obtained from the discretized balance of momentum. Alternatively, one can compute density directly as an SPH interpolation of particle masses [15]. The latter approach is less common, but it leads to a symplectic structure of the system of SPH differential equations, which makes the WCSPH discretization completely stable even in the absence of viscosity or stabilization. Although the former method leads also to a Hamiltonian system, it is not symplectic,

but only Poisson, which makes it harder to construct a structure-preserving geometrical numerical integrator [12]. Another a bit more complicated symplectic scheme was proposed in [16], where the density is coupled with another field (similarly as position is coupled with momentum).

However, standard symplectic WCSPH shows unphysical behavior at free surfaces, where constant functions are not correctly interpolated [14]. We suggest two ways how to correct this issue. The first method modifies the density by an appropriate integration constant, which is easy to implement. The second, and more complex method, renormalizes the initial state by solving a certain nonlinear problem using Newton's method. We also demonstrate that a careful implementation of the symplectic WCSPH scheme, using the corrected treatment of free surfaces and the fixed-point (as opposed to the more usual floating-point) arithmetic leads to global time-reversibility. This can be considered as an additional symmetry-preserving feature alongside the conservation of energy, mass, momentum, and angular momentum. The purpose of this paper is to show key advantages of the symplectic WCSPH compared to the standard approach.

The symplectic WCSPH with a proper treatment of free boundaries, conservative wall-fluid interaction, and fixed-point arithmetic becomes globally reversible in time. For instance, the breaking-dam simulation can be reversed to recover the initial conditions. Although the resulting code is energy-preserving and reversible, it can still be considered dissipative in the sense that the Boltzmann entropy of the SPH particles grows. In other words, we observe the emergence of the second law of thermodynamics from purely reversible dynamics. In the case of the breaking dam simulation, the particles eventually occupy the bed of the container and their velocity distribution is approximately Maxwellian. We provide a reasoning for this apparent paradox between reversibility and irreversibility by means of information theory at the end of the manuscript.

The energy budget in SPH simulations is of great interest because it indicates which degrees of freedom lose energy and which gain it [17]. Dissipative terms (like the viscous terms or the diffusive terms) typically reduce the total energy, but sometimes the kinetic energy decreases and compressional energy increases while in other cases the kinetic energy increases. Although it may be tempting to link the decrease of a particular kind of energy (for instance kinetic energy) with dissipation, such link can not hold in general, since sometimes the particular kind of energy increases and sometimes decreases. The equilibrium partitioning of the total energy budget can be actually estimated from the virial theorem [18]. Therefore, the initial conditions determine which part of the energy will grow and which will drop. For isolated systems, it is the growth of entropy that indicated dissipation while in isothermal systems the total free energy decreases [19]. In this manuscript, we discuss how entropy grows even in reversible isolated systems.

We demonstrate the various versions of WCSPH on dam-break and Gresho vortex benchmarks. All SPH codes used to make this paper is freely available within the new SmoothedParticles.jl package [20] written in the Julia programming language [21]. But let us first recall the WCSPH equations in the following Section.

2. WCSPH for inviscid fluids

The standard weakly compressible spatial semi-discretization of Euler fluid equations in a uniform gravitational field is [22]:

$$\partial_t \rho_a = \sum_b m_b (\mathbf{u}_a - \mathbf{u}_b) w'(r_{ab}) \mathbf{e}_{ab}, \quad (1a)$$

¹ It is possible that the intimate connection between the parameters in the diffusive and viscous term might be connected with the alternatives to the Navier-Stokes equations where Laplacian-like terms are present in both the momentum equation and the equation of continuity [5,6].

$$\partial_t \mathbf{u}_a = \sum_b m_b \left(\frac{p_a}{\rho_a^2} + \frac{p_b}{\rho_b^2} \right) w'(r_{ab}) \mathbf{e}_{ab} - g \hat{\mathbf{z}}, \quad (1b)$$

$$\partial_t \mathbf{r}_a = \mathbf{u}_a, \quad (1c)$$

where the pressure is a function of density via the barotropic formula,

$$p(\rho) = \frac{c^2 \rho_0}{7} \left[\left(\frac{\rho}{\rho_0} \right)^7 - 1 \right]. \quad (2)$$

Constant ρ_0 stands for the referential density, g is the gravitational acceleration, and c is the numerical speed of sound (typically chosen as ten times the characteristic flow speed U_{char}). It is well known that the system of ordinary differential equations (1) conserves the total energy in the form

$$\mathcal{H} = \sum_a m_a \left(\frac{v_a^2}{2} + \epsilon_a + gz \right), \quad (3)$$

where

$$\epsilon_a = \frac{c^2}{42} \left[\left(\frac{\rho}{\rho_0} \right)^6 + \frac{6\rho_0}{\rho} \right]$$

is the potential of internal energy (also called compressional) satisfying $d\epsilon_a = \frac{p_a}{\rho_a} d\rho_a$. Moreover, for $g = 0$, the momentum

$$\mathcal{M} = \sum_a m_a \mathbf{u}_a,$$

and angular momentum

$$\mathcal{L} = \sum_a m_a \mathbf{r}_a \times \mathbf{u}_a$$

are conserved as well. Naturally, gravitational force can deliver some momentum to the fluid, while the equal opposite reaction of the fluid on Earth is considered grounded.

The WCSPH equations (1) represent a Hamiltonian system, which can be checked for instance using program [23]. But it is not a symplectic system because the mass density is treated as a state variable. If, on the other hand, the density would always be calculated from the current positions of the particles, then only the positions and momenta would be state variables and the system of equations would be symplectic. Symplecticity would make it easier to choose a geometric structure-preserving numerical integrator, for instance using the Störmer-Verlet scheme [24,12].

A symplectic form of WCSPH is obtained by solving the ordinary differential equation for density (1a),

$$\rho_a = \sum_b m_b w(r_{ab}), \quad (4)$$

instead of updating ρ_a iteratively by (1a). However, this closed expression for density (4) is rarely used in practice because it leads to questionable behavior near free surfaces [14]. This happens because free boundary particles are under-occupied and, according to (4), they have $\rho \ll \rho_0$. Therefore, they are equipped with large internal energy and, affected by its negative gradient, they start to vibrate. A remedy is provided in the following section, which leads to the possibility to use the symplectic form of WCSPH.

3. Treatment of free surfaces

3.1. Solving the equation for ρ_a with an appropriate integration constant

The issue of unphysical behavior at free surfaces can be corrected by choosing an appropriate integration constant when solving the differential equation for ρ_a ,

$$\rho_a = \sum_b m_b w(r_{ab}) + C_a, \quad (5)$$

where

$$C_a = \rho_0 - \rho_a|_{t=0}.$$

Indeed, since WCSPH based on (1a) typically assumes zero internal forces at $t = 0$, it is actually (5) and not (4) that is equivalent to the standard WCSPH formulation, since (4) leads to non-zero density gradients near the boundary. Although schemes based on (1a) and (5) are completely equivalent at the ODE level, they become very much different once time discretization is considered. It appears that (1a) is currently used by most researchers, despite the advantages of Equation (5):

1. Inferring ρ from positions using Equation (5) does not accumulate the density error.
2. The system of SPH evolution equations becomes symplectic (and not only Hamiltonian).
3. Therefore, symplectic structure-preserving integrators can be employed, which leads to simulations globally reversible in time.

However, even if we use the correct closed formula for density (5) and use a symplectic integrator, are facing another obstacle. For problems involving free surfaces, integration constant C_a is typically much bigger for boundary particles and, therefore, whenever such particle submerges into interior of the fluid body, it generates a small void pocket around itself. This unwanted numerical artefact is removed in the following section.

3.2. Initial state correction (ISC)

The numerical artefact that particles that are originally at the boundary are treated differently than the rest of the particles, even if the submerge into the in the interior of the fluid, is rooted in the difference in the C_a constants at the beginning. Therefore, we shall remove that artifact by correcting the initial state.

A solution is to correct the initial positions by a vector field $\delta \mathbf{x}$ such that

$$\rho_0 = \sum_b m_b w(|\mathbf{x}_a + \delta \mathbf{x}_a - \mathbf{x}_b|).$$

These non-linear equations can be solved by a strategy based on the Newton's method, details of which follow. Linearization with respect to $\delta \mathbf{x}_a$ leads to

$$\rho_0 - \rho_a \doteq \sum_b m_b (\delta \mathbf{x}_a - \delta \mathbf{x}_b) \cdot w'(r_{ab}) \mathbf{e}_{ab}.$$

On the right hand side, we identify the discrete divergence operator \tilde{D}^1

$$-\rho_a \tilde{D}_a^1 \delta \mathbf{x} \doteq \rho_0 - \rho_a, \quad (6a)$$

see [14] for details. This linear problem for unknowns $\delta \mathbf{x}$ is under-determined, so shall be restricted to $\delta \mathbf{x}$ in the form of a discrete gradient

$$\delta \mathbf{x}_a = \sum_b m_b \left(\frac{\phi_a}{\rho_a^2} + \frac{\phi_b}{\rho_b^2} \right) w'(r_{ab}) \mathbf{e}_{ab},$$

which can be also rewritten as

$$\delta \mathbf{x}_a + \frac{1}{\rho_a} G_a^1 \phi = 0. \quad (6b)$$

Sparse linear system (6) for $\delta \mathbf{x}$ and ϕ has to be solved iteratively,

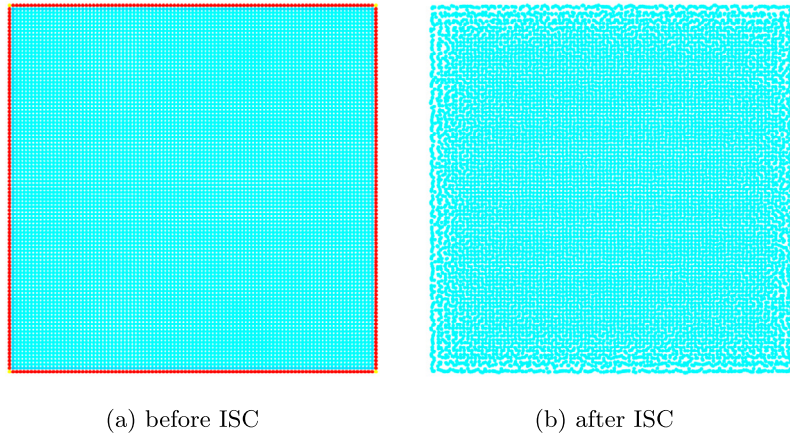


Fig. 1. Applying ISC to particles in square arranged regularly. Density (4) is shown in color (red to blue). Initially, it varies due to boundary effect but becomes everywhere constant after 7 iterations of ISC (up to relative error less than 10^{-10}). (For interpretation of the colors in the figure(s), the reader is referred to the web version of this article.)

updating \mathbf{x} and reevaluating ρ according to (4), until $\rho \doteq \rho_0$ with satisfactory precision. This initial state correction (ISC) procedure has been tested in our numerical examples, and the procedure converges quadratically except for problems with too much symmetry (for instance rectangle with particles arranged in square grid nearly always diverges).² The whole procedure may be then summarized as follows (see Fig. 1):

Initial state correction (ISC)

1. set $|\delta \mathbf{x}_a| < \frac{\delta r}{10}$ randomly for all a
2. repeat until sufficient precision is acquired:
3. $\mathbf{x}_a = \mathbf{x}_a + \delta \mathbf{x}_a$ for all a
4. recompute neighbor list
5. find $\rho_a = \sum_b m_b w(r_{ab})$ for all a
6. solve $N(d+1) \times N(d+1)$ linear problem

$$\begin{bmatrix} I & \frac{1}{\rho} G^1 \\ -\rho \tilde{D}^1 & 0 \end{bmatrix} \begin{bmatrix} \delta \mathbf{x} \\ \phi \end{bmatrix} = \begin{bmatrix} 0 \\ \rho_0 - \rho \end{bmatrix}$$

This computation is expensive, but is performed only once per simulation. In place of the linear system with 2×2 block matrix, one could also solve directly for ϕ :

$$-\rho \tilde{D}^1 \frac{1}{\rho} G^1 \phi = \rho_0 - \rho.$$

However, the product $A = -\rho \tilde{D}^1 \frac{1}{\rho} G^1$ leads to a matrix which is much more dense. A matrix-free iterative method could be used without evaluating the product directly, is a future possibility.

Let us note that after ISC, all constant fields will be correctly interpolated, at least initially. Weak compressibility helps to preserve this trait approximately in a way that does not accumulate error provided (4) is used. In this sense, ISC can be considered an alternative to (zeroth order) operator renormalization with the benefit that it does not break the symmetry of smoothing kernel. Unfortunately, this technique has two drawbacks. Firstly, it may slightly deform geometry in an unwanted way. Secondly, adapting it to a concrete setting may be difficult – for instance, when an anti-clump term is included.

² For these cases, we recommend to initially disrupt particle positions by a random noise.

Both symplecticity of the system of equations and ISC improve the numerical solutions, but in order to obtain a globally reversible behavior we have to tackle a further problem caused at the walls of the simulation box, as in the following section.

3.3. Wall modelling

In WCSPH, walls can be modeled by a layer of dummy particles which behave as if they belonged to the fluid, except that their positions and velocities are fixed. In this approach, it is hoped that the forces preventing compression will deflect any incoming particle. This method, of course, violates balance of momentum, but this is plausible, since we can imagine that any momentum yielded by the fluid is grounded. More importantly though, dummy particles violate conservation of energy. To see this, consider a wave stopped by a wall. The fluid acts on the solid with equal and opposite force. Therefore, a wall particle a is subject to acceleration, which should change its velocity after time step δt to

$$\mathbf{v}_a = \delta t \frac{\mathbf{F}_a}{m_a}.$$

To preserve wall integrity, this velocity must be annulled, reducing the total energy by a small kinetic contribution. From this, we see that dummy particles are essentially dissipative.

One could argue that this is still physically reasonable because every fluid-solid collision creates a sound wave, leading to loss of energy. However, it is dubious whether such effect is correctly modeled by dummy particles. Moreover, it complicates efforts to make a strictly energy-conservative scheme.

An alternative approach uses a fluid-solid force inspired by the Lennard-Jones potential

$$\mathbf{F}_{a \rightarrow b} = -\frac{E_{\text{wall}}}{r_{ab}^2 + \varepsilon^2} (s_{ab}^2 - s_{ab}) \mathbf{r}_{ab}$$

by which a wall particle a acts onto a fluid particle b . Here,

$$s_{ab} = \begin{cases} \frac{r_{\text{wall}}^2 + \varepsilon^2}{r_{ab}^2 + \varepsilon^2} & \text{if } r_{ab} < r_{\text{wall}}, \\ 1 & \text{otherwise.} \end{cases}$$

r_{ab} is the distance between a wall particle and a fluid particle, and $E_{\text{wall}}, r_{\text{wall}},$ and ε are numerical parameters [25].³ Except for this

³ In our dam-break simulation, we choose $E_{\text{wall}} = 10gh$ (g being the gravitational acceleration and h the height of the water column), $r_{\text{wall}} = 0.95dr$ (dr being the typical distance between particles), and $\varepsilon = 10^{-6}$.

interaction, wall particles are neither considered in the balance of mass (1b) nor in the calculation of density (5). Unlike the dummy particle approach, this solid wall modeling is conservative, with a modified energy

$$\mathcal{H} = \sum_{a \in \text{fluid}} m_a \left(\frac{v_a^2}{2} + \epsilon_a + gz \right) + \sum_{a \in \text{wall}} \sum_{b \in \text{fluid}} E_{\text{wall}} \left(\frac{1}{4} s_{ab}^2 - \frac{1}{2} s_{ab} + \frac{1}{4} \right), \quad (7)$$

and the wall-particle force is just minus the derivative of the wall-particle interaction energy. To see this, compute the total differential

$$\begin{aligned} d\mathcal{H}_{\text{wall}} &= \sum_{a \in \text{wall}} \sum_{b \in \text{fluid}} E_{\text{wall}} d \left(\frac{1}{4} s_{ab}^2 - \frac{1}{2} s_{ab} + \frac{1}{4} \right) \\ &= \sum_{a \in \text{wall}} \sum_{b \in \text{fluid}} E_{\text{wall}} \left(\frac{s_{ab}}{2} - \frac{1}{2} \right) ds_{ab} \\ &= - \sum_{a \in \text{wall}} \sum_{b \in \text{fluid}} E_{\text{wall}} \left(\frac{s_{ab}}{2} - \frac{1}{2} \right) \frac{r_{\text{wall}}^2 + \epsilon^2}{(r_{ab}^2 + \epsilon^2)^2} dr_{ab} \\ &= - \sum_{a \in \text{wall}} \sum_{b \in \text{fluid}} E_{\text{wall}} (s_{ab}^2 - s_{ab}) \frac{1}{r_{ab}^2 + \epsilon^2} \mathbf{r}_{ab} \cdot d\mathbf{r}_{ab} \end{aligned}$$

and hence, we have, for every fluid particle b :

$$-\frac{\partial \mathcal{H}_{\text{wall}}}{\partial \mathbf{x}_b} = - \sum_{a \in \text{wall}} E_{\text{wall}} (s_{ab}^2 - s_{ab}) \frac{1}{r_{ab}^2 + \epsilon^2} \mathbf{r}_{ab} = \sum_{a \in \text{wall}} \mathbf{F}_{a \rightarrow b}$$

This makes it potentially advantageous for problems involving inviscid flows.

Note that differential equations (1) (with or without the explicit density integration (4)) automatically conserve the Hamiltonian (or energy), due to their Hamiltonianity (in particular symplecticity) [14]. Indeed, the energy is conserved due to the skew-symmetry of the underlying Poisson bracket, and the momentum is conserved if the Hamiltonian is invariant with respect to spatial translations [12,26]. Or course, the conservativeness can be also checked manually by directly evaluating the conservation laws.

The values of the wall-interaction parameters depend on the particular situation. The wall energy must be much higher than typical energy of a particle colliding with the wall so that particles effectively bounce off the wall. The r_{wall} parameter must be, on the other hand, smaller than the typical distance between the particles so that the wall-particle interactions do not disturb the particle-particle interactions.

In our case, when we seek a globally reversible-in-time simulation, the conservativeness of the fluid-wall interaction becomes important.⁴ However, even if we use the correct close formula for density (1a), the initial state correction, and the conservative fluid-wall interaction, the symplectic Störmer-Verlet scheme is not reversible globally in time because of the errors caused by the floating-point arithmetic. The following section contains the final ingredient necessary for that reversibility, the symplectic Störmer-Verlet integrator with fixed-point arithmetic.

4. Symplectic integrator and fixed-point arithmetic

The symplectic character of evolution equations (1b) and (1c) is preserved in symplectic numerical schemes, for instance the clas-

⁴ Note that the results about global time-reversibility would stay the same if we chose a system without boundary, where no wall-fluid treatment would be necessary.

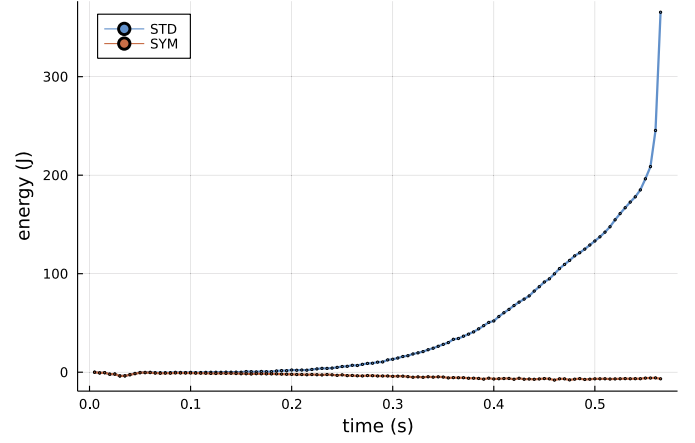


Fig. 2. Energy growth in standard WCSPH (STD) and symplectic WCSPH (SYM) in dambreak simulation with zero viscosity and parameters from Table 1. Without a stabilization of some sort, STD diverges, whereas SYM is stable.

sical Verlet scheme [27]. Consequences are for instance the long-time stability of the trajectories and conservation of integrals of motion (energy, momentum, and angular momentum, among others) [12]. However, even application of the Verlet scheme in SPH does not lead to globally in-time reversible simulations due to the floating-point errors, but a remedy is in the fixed-point arithmetic, as we show below.

The advantage of the direct update of density to the integration of the continuity equation is that the former way leads to a symplectic scheme while the latter to a non-symplectic (albeit still Hamiltonian) scheme. Although the scheme with integration of the continuity equation is still Hamiltonian, the underlying Poisson bracket is non-canonical (Poisson geometry), and it is more difficult to construct numerical schemes respecting the geometrical structure [12]. For instance, the standard symplectic schemes like Störmer-Verlet do not preserve the Poisson structure, but they preserve the symplectic structure.

The usual discretization of the SPH equations using the Störmer-Verlet scheme is

1. $\mathbf{u}(t_{m+\frac{1}{2}}) = \mathbf{u}(t_m) + \frac{1}{2} \delta t \mathbf{a}(\mathbf{r}(t_m))$
2. $\mathbf{r}(t_{m+1}) = \mathbf{r}(t_m) + \delta t \mathbf{u}(t_{m+\frac{1}{2}})$
3. $\mathbf{u}(t_{m+1}) = \mathbf{u}(t_{m+\frac{1}{2}}) + \frac{1}{2} \delta t \mathbf{a}(\mathbf{r}(t_{m+1}))$,

where \mathbf{a} is the acceleration composed of internal, gravitational, and wall forces. The scheme is of second order and symplectic, and therefore it conserves energy $\mathcal{H}_{\delta t}$ with error

$$\mathcal{H}_{\delta t}(\mathbf{r}, \mathbf{u}) - \mathcal{H}(\mathbf{r}, \mathbf{u}) = O(\delta t^2)$$

that does not depend explicitly on time, provided that δt is sufficiently small [28].⁵ If we took ρ as a separate state variable with its own evolution equation (1a) (usual WCSPH), symplecticity of the system of equations would be violated. The usual WCSPH equations are still Hamiltonian (generated by a Poisson bracket and a Hamiltonian), as checked by program [23], but they are not symplectic and they thus the (symplectic) Verlet scheme does not preserve their geometric structure, which causes energy to grow exponentially, unless some stabilization is used - see Fig. 2.⁶

⁵ Here, we rely on the fact that $p = p(\rho) = p(\rho(\mathbf{r}))$ using the closed expression (5).

⁶ In [22], it is suggested to correct this error by a mid-step extrapolation of density. However, it should be noted this approach adds additional inaccuracy to the scheme.

Table 1
Parameters used for dam-break test.

| | | |
|------------------------|------------|------------------------|
| density | ρ | 1000 kg/m ³ |
| spatial step | dr | 0.005 m |
| num. sound speed | c | 120 m/s |
| gravitational constant | g | 9.8 m/s ² |
| water column width | l_{wcv} | 1 m |
| water column height | l_{wch} | 2 m |
| box width | l_{bw} | 4 m |
| box height | l_{bh} | 3 m |
| kernel support radius | h | 3 dr |
| Lennard-Jones radius | r_{wall} | 0.95 dr |
| Lennard-Jones energy | E_{wall} | 10 mgl_{wch} |
| time step | dt | 0.2 h/c |

Besides being symplectic, Verlet scheme is also time reversible, which means that after changing the sign of velocities, the scheme returns back in time. The scheme thus preserves the time-reversal symmetry of the original system (1a), (1b), (1c). We can verify this by substituting

$$\mathbf{u}(t_m) \mapsto -\mathbf{u}(t_{m+1})$$

$$\mathbf{u}(t_{m+1}) \mapsto -\mathbf{u}(t_m)$$

$$\mathbf{r}(t_m) \mapsto \mathbf{r}(t_{m+1})$$

$$\mathbf{r}(t_{m+1}) \mapsto \mathbf{r}(t_m)$$

which produces the same set of equations

1. $-\mathbf{u}(t_{m+\frac{1}{2}}) = -\mathbf{u}(t_{m+1}) + \frac{1}{2}\delta t \mathbf{a}(\mathbf{r}(t_{m+1}))$
2. $\mathbf{r}(t_m) = \mathbf{r}(t_{m+1}) - \delta t \mathbf{u}(t_{m+\frac{1}{2}})$
3. $-\mathbf{u}(t_m) = -\mathbf{u}(t_{m+\frac{1}{2}}) + \frac{1}{2}\delta t \mathbf{a}(\mathbf{r}(t_m))$,

but in the reversed order. Unfortunately, the time reversibility fails in the floating-point arithmetic (FloPA), where addition is *not* associative. In particular, addition and subtraction of a value δx to a float x does not recover x . For instance

$$(1 + 0.5\epsilon) - 0.5\epsilon \stackrel{\text{float}}{=} 0.9999999999999999 \neq 1. \quad (8)$$

Although this error is usually very small, it tends to accumulate in the presence of non-linearities and destroys the reversibility in longer simulations.

There is, however, an easy solution suggested by [29] in the context of N-body simulations of Solar System. It converts vectors $\mathbf{r}(t_m)$, $\mathbf{u}(t_m)$, and $\mathbf{a}(t_m)$ to the fixed-point arithmetic (FixPA) just before they are used in the time-step evaluation. Since addition is associative in FixPA, this method allows for bit-precise time reversibility and long-time conservation of energy – see Fig. 3. Note that the intermediate computations of the sums in (5) and (1b) can be still performed in FloPA and only then converted to FixPA. However, due to the non-associativity of FloPA, summation of more than two elements in FloPA is order-dependent, and to ensure reversibility, the order of the summands must be chosen in a way that does not depend on the current state of the simulation (for instance, it is possible to perform summations always in the order of the particle indices).

In summary, symplectic WCSPH with the correct closed formula for density, the initial state correction, the conservative wall-fluid interaction, and the symplectic numerical Verlet scheme in the fixed-point arithmetic finally lead to globally-in-time reversible simulations. We have demonstrated the reversibility for instance on the dam break benchmark, and Appendix A contains the Gresho vortex benchmark. Although the simulation is symmetric, we can still observe the growth of entropy if we choose not to see all the details of the simulation, which is the matter of the following section (Fig. 4).

5. Dissipativity vs. decrease in mechanical energy

Can we judge dissipativity of an SPH simulation from observing decrease of mechanical energy or increase of internal (or compressional) energy? The purpose of this Section is to discuss the relation between dissipation and transformation of particular forms of energy.

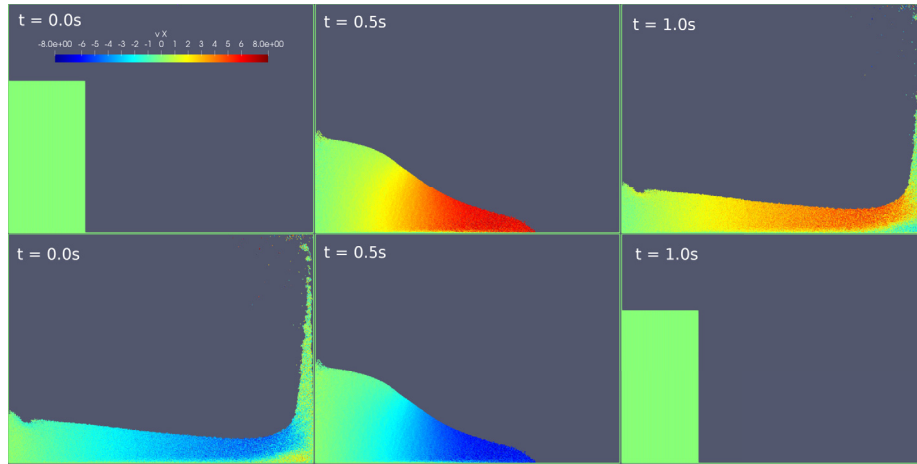
For instance the δ -SPH method adds a diffusive term to the continuity equation. The purpose of this term is stabilization of the scheme, and the term actually removes the noise from the pressure field and decreases the energy dissipation caused by the numerical scheme [17]. However, it is not straightforward to add the δ -SPH term into our symplectic scheme because our scheme does not contain the discretized continuity equation, to which that term would be added. Instead, we evaluate the density from the current particle positions (and from a correction based on their initial position). However, since our numerical scheme preserves the energy (up to a tiny constant that decreases with the time step), we do not need the δ -SPH term to decrease the dissipation of energy here, see Fig. 5. Moreover, since our aim is to obtain the global-in-time reversibility, we can not add the δ -SPH term here because it would violate the reversibility.

Nevertheless, the δ -SPH-like term might be added into the symplectic scheme in an indirect way. If another vector field is added to the state variables and coupled to the density as in mechanics of superfluids [33], it might be possible to keep the symplecticity of the SPH scheme. Algebraic dissipation in the equation for the extra vector field should then, after the field relaxes to a quasi-equilibrium value, restore a diffusion-like term in the density equation, as in [34].

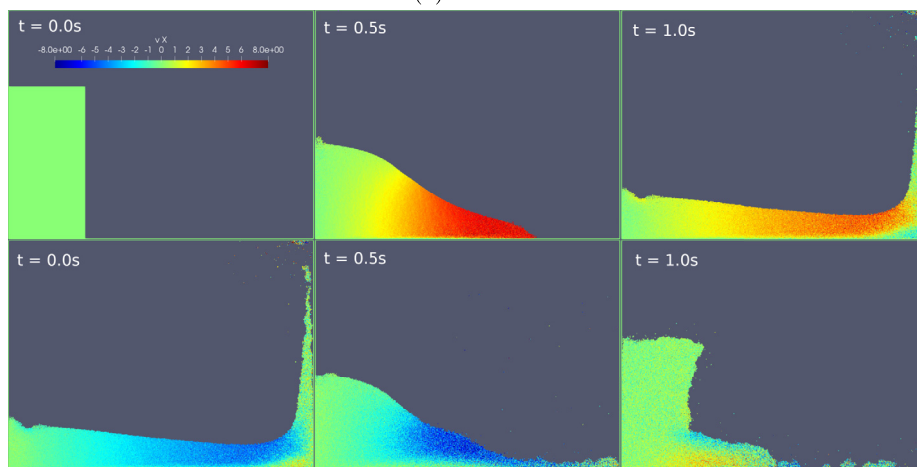
In paper [17], the sum of the kinetic and potential energies is called mechanical, and our internal energy is called compressional. The dissipation is calculated as the negative of the evolution of the mechanical energy in [17]. Therefore, we can compare the behavior of our kinetic, potential, and internal energies with the mechanical and compressional energies from [17]. Plots of the components of energy during the globally reversible dam-break simulation, namely the kinetic energy, gravitational (or potential) energy, the compressional energy, and the wall energy (from the wall-fluid interactions) are contained in Appendix C.

Since our scheme is symplectic, we preserve the underlying geometrical structure of the evolution equations (symplecticity), but the total energy is conserved only approximately. This is a feature of symplectic integrators that can not be circumvented because only the exact solutions preserve both the symplectic structure and energy [35]. However, the error in the total energy does not accumulate over time with symplectic integrators (it remains bounded by the time-step and order of the method), see [12] (Ch. IX.8). In our case, the numerical error in the total energy was less than $2 \cdot 10^{-4}\%$. Moreover, the qualitative behavior (growth of entropy and global reversibility) is not affected by either raising or reducing the time-step, despite the numerical error in energy decreases with lower time steps. Therefore, the qualitative behavior is not caused by the numerical errors in the total energy.

While the total energy is approximately conserved in the dam-break simulation, the gravitational energy oscillates until it reaches the minimum when the particles occupy the bottom of the container. Similarly, the wall-energy oscillates during the simulation, but it is small in comparison with the total energy. The kinetic energy goes in a non-monotonous way from the initial zero (particles not moving initially) until it reaches its maximum. Similarly, the compressional (or internal) energy grows until it reaches its maximum. Energy mainly flows from the gravitational energy (which decreases in time) to the kinetic energy and to the internal (compressional) energy (approximately 3/4 to the kinetic and 1/4 to the internal).



(a) FixPA



(b) FloPA

Fig. 3. Results for dam break test with parameters from Table 1 using symplectic WCSPH. At $t = 1$ s, we reset the time counter and revert all velocities. In FixPA, the simulation is completely reversible and returns to the initial state. In FloPA, this fails due to round-off errors illustrated in (8).

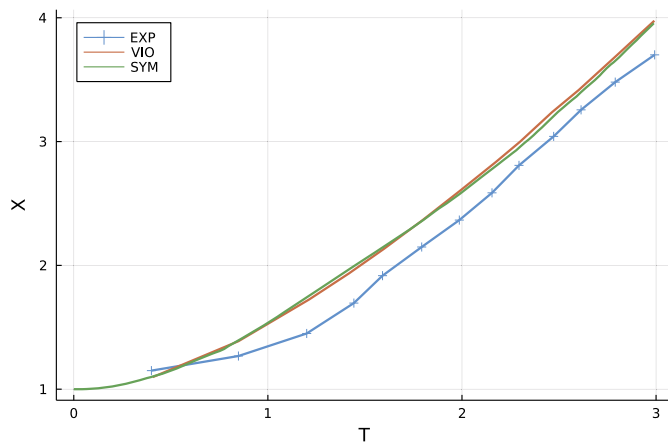


Fig. 4. Comparison of symplectic WCSPH (SYM) in dam-break simulation with experimental data [30] (EXP) and numerical result from Violeau's book [14] (VIO). Here, $T = t\sqrt{g/l_{wcv}}$ is a dimensionless time and $X = l_{le}/l_{wcv}$, where l_{le} is the x -coordinate of the wave's leading edge.

Although the overall mechanical energy (kinetic + potential) decreases, its drop can not be associated with dissipation in general. Instead, dissipation should be considered as the reduction of the total energy (including the compressional part). When this occurs, it also means that the simulated physical system is not isolated,

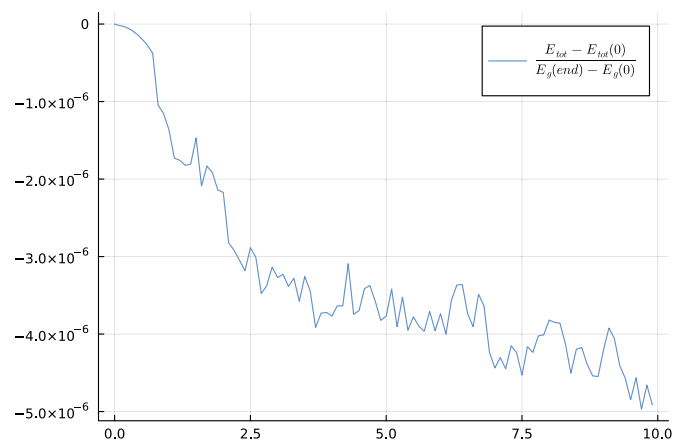


Fig. 5. Total energy (kinetic, potential, compressional, and wall) in the dam-break simulation. The initial value is subtracted and the remainder is divided by the total change of the potential energy during the simulation, as in [31,32]. The total energy is well preserved in our scheme. The total change is bounded in time and the bound decreases with the time step.

since otherwise the total energy would be conserved. A typical SPH simulation is not isolated, as the total energy typically decreases due to either the integrator or due to artificial dissipation [17].

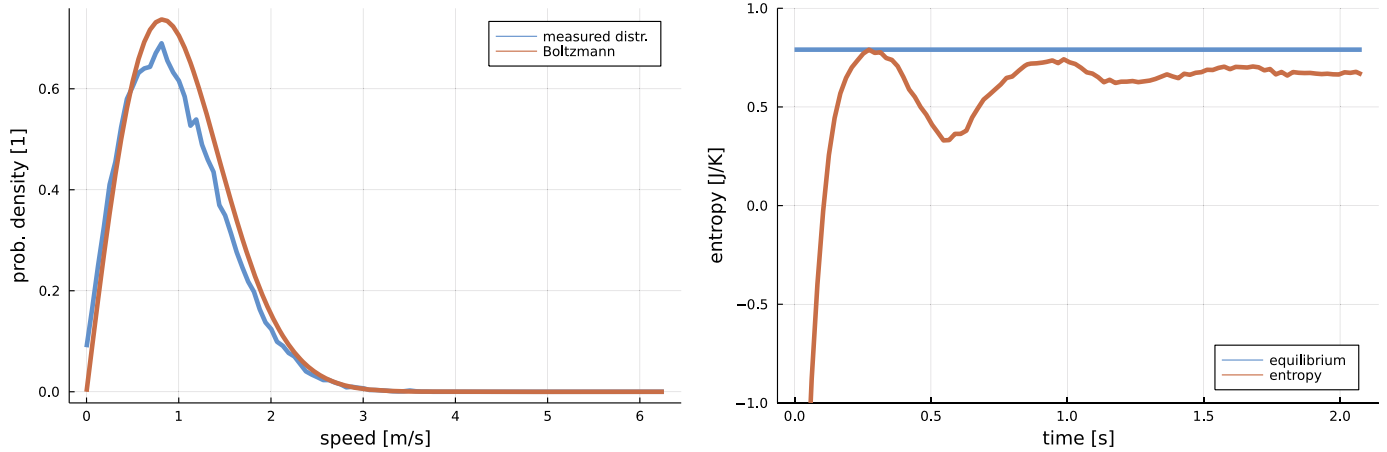


Fig. 6. Left: Histogram of the velocities of the particles at time $t = 2.0$ (blue) in comparison with the equilibrium Maxwell-Boltzmann distribution (orange) (19) with fitted temperature T . Right: Evolution of Boltzmann entropy (see Appendix B) in the reversible breaking-dam simulation (blue). Despite the reversibility of the dynamics, the entropy increases and approaches equilibrium entropy corresponding to the temperature of the measured Maxwell-Boltzmann distribution (blue line) from (21).

Let us now address the question whether symplectic integrators reduce the dissipation. First, symplectic integrators are suitable only for the reversible part of the differential equations, whereas the irreversible part (viscosity and diffusion) is typically not in the symplectic form [14]. Non-symplectic integrators, however, can cause irreversibility even in the reversible part of the equations. Although they can conserve the energy precisely, they do not preserve the phase-volume, which means that they affect the evolution of the distribution function of the particles [13]. Consequently, they affect the Liouville entropy of the system, which causes dissipation. Another source of irreversibility is the floating-point arithmetic, which actually spoils the reversibility and phase-volume preservation of the exact symplectic integrators, leading to similar source of irreversibility as the non-symplectic integrators. In practice, the dissipation caused by imperfect integration of the equations is often shadowed by the dissipation due to the viscous terms that are pertinent in situations that require some smoothing (for instance distorted boundary [15]). Nevertheless, if one wishes to minimize the dissipation due to the reversible terms in the SPH scheme, one should use the symplectic integrator, fixed-point arithmetic, and better also the other tweaks proposed in the current manuscript.

6. Emergence of the second law of thermodynamics

The second law of thermodynamics tells that the entropy of each isolated system grows until the system reaches the thermodynamic equilibrium. Where does this irreversible behavior come from when the underlying evolution equations for particle dynamics (here SPH) are reversible? In this section we illustrate that the emergence of the second law from completely reversible dynamics is caused by ignoring details of the dynamics, similarly as in [36–38].

The emergence of the second law is actually expected due to the result of Lanford [39] and following works [40], where a system of classical particles with a short-range potential is shown to obey the Boltzmann equation. The collision term in the Boltzmann equation then causes the growth of the Boltzmann entropy. Fig. 6 shows the growth of Boltzmann entropy in a reversible SPH breaking-dam simulation. But how to interpret the Lanford’s mathematical result and the observed growth of Boltzmann entropy of the SPH particles from the physical point of view? The SPH particles obey reversible Hamiltonian dynamics. Another possibility to describe their motion is the Liouville equation, which ex-

presses reversible evolution of the N -particle distribution function, $f_N(t, \mathbf{r}_1, \mathbf{p}_1, \dots, \mathbf{r}_N, \mathbf{p}_N)$. Indeed, Liouville equation follows from the particle mechanics, and, vice versa, if we set the distribution function to be the product of Dirac δ -distributions in the positions and momenta of all particles, we recover Hamilton canonical equations. Liouville equation also conserves the Liouville entropy

$$S^{\text{Liouville}}(f_N) = -\frac{k_B}{N!} \int d\mathbf{r}_1 \int d\mathbf{p}_1 \dots \int d\mathbf{r}_N \int d\mathbf{p}_N f_N \ln(h^{3N} f_N), \tag{9}$$

which thus remains constant. This is consistent with the reversibility of the underlying Hamiltonian particle mechanics.

Now we decide not to see all the positions and momenta of the individual particles, observing for instance only the probability distribution of momenta at given space and time. Such one-particle distribution function $f(t, \mathbf{r}, \mathbf{p})$ indeed does not contain the knowledge of positions and momenta of all particles and thus the entropy of the system expressed in terms of f must be higher than the Liouville entropy (functional of f_N). The former is the Boltzmann entropy and it is obtained by maximization of the Liouville entropy subject to the constraint that the one-particle distribution function is known [26]. Plugging the resulting f_N back into the Liouville entropy, we obtain the Boltzmann entropy

$$S^{\text{Boltzmann}}(f) = -k_B \int d\mathbf{r} d\mathbf{p} f (\ln(h^2 f) - 1) \tag{10}$$

see [26]. Because the Boltzmann entropy is the Liouville entropy evaluated at the point f_N where it is maximal (keeping the knowledge of f), the Boltzmann entropy is higher than the Liouville entropy. Although the Liouville entropy remains constant in the dynamics, the Boltzmann entropy can grow in the dynamics following the Liouville equation.

The irreversibility of the dynamics of the one-particle distribution function can be illustrated on the reversible breaking-dam simulation with fixed-point arithmetic. Section 4 contains details of the simulation, but let us also show the histogram of the particle velocity distribution in the middle of the simulation, just before the velocities are inverted. Fig. 6 shows the measured histogram of the velocities of the SPH particles in comparison with the equilibrium Maxwell-Boltzmann distribution function (19) obtained by

fitting the effective temperature.⁷ Although all velocities were initially zero, their distribution approaches the equilibrium distribution. This approach towards equilibrium is reflected in the growth of Boltzmann entropy during the long-time reversible simulation.

In other words, when the particles are described by the Boltzmann equation, our knowledge is incomplete, since the positions and momenta of all the particles remain unknown, in contrast to the description by means of Hamilton canonical equations or Liouville equation. And this lack of knowledge makes the evolution of the one-particle distribution function f irreversible. The irreversibility is then explicitly expressed by the collision integral in the Boltzmann equation. The second law of thermodynamics thus emerges from completely reversible dynamics when our description is incomplete (not seeing all positions and momenta of the particles).

In summary, if we see all the positions and momenta in the SPH simulation, we can not see the second law of thermodynamics. Indeed, the simulation is reversible and the Liouville entropy remains constant. However, when we only focus on the one-particle distribution function, we can see the growth of Boltzmann entropy and thus irreversible behavior. The second law of thermodynamics emerges when we our knowledge about the precise state of the system is incomplete [38].

Interestingly, since our discrete system is deterministic, reversible and can exist in only finitely many states, it is recurrent [41]. In other words, if the system evolves long enough, it comes back to the initial state exactly (provided that the particles are not allowed to escape to infinity). However, since the phase space of the system contains thousands of SPH particles, it has enormous amount of states, which makes it highly unlikely to observe the recurrence theorem in practice.

7. Conclusion

In this paper we have turned the usual weakly compressible smoothed particle hydrodynamics (WCSPH) to a symplectic form by finding the correct closed formula for the mass density. Because the closed formula for density leads to different treatment of particles that are initially near the boundary, the method of initial state correction (ISC) was introduced, due to which all particles are then treated in the same way. This leads to stable SPH simulations in the presence of free surfaces without any further stabilization.

In order to get simulations that preserve the energy, we use a conservative fluid-wall interaction. A symplectic (Verlet) scheme, which is suitable for the symplectic WCSPH, implemented in the fixed-point arithmetic then leads to globally-in-time reversible SPH simulations. This is demonstrated on the dam-break benchmark, where inversion of velocities at a later stage of the simulation eventually leads the system back to the initial state. The simulations are available in a new Julia package *SmoothedParticles.jl* [20].

Despite the global reversibility of the simulations, we observe thermodynamic behavior when we do not use all the details of the simulation. The Boltzmann entropy, which depends only on the one-particle distribution function and not on positions of individual particles, grows in the dam-break simulation and approaches the equilibrium value. In other words, we observe the emergence of the second law of thermodynamics from purely reversible dynamics, caused by reduction of our knowledge about the system.

⁷ Note that the effective temperature is not the physical temperature of the system because it is calculated from the overall motion of the macroscopic SPH particles. To see this, consider the extreme case of only one SPH particle with weight one kilogram, where the effective temperature obtained from the motion of that macroscopic particle does not coincide with the physical temperature of that particle.

In future, we would like to extend the WCSPH framework to non-isothermal fluids and solids while keeping the Hamiltonianity of the equations and numerical schemes. In particular, we would like to apply our approach towards reversibility in solid mechanics, using for instance the Lagrangian kernels [9,10].

Declaration of competing interest

The authors declare that they have no known competing financial interests or personal relationships that could have appeared to influence the work reported in this paper.

Data availability

Our code, including the examples, is publicly available as the *SmoothedParticles.jl* Julia package.

Acknowledgements

OK was supported by project No. START/SCI/053 of Charles University Research program. MP was supported by project No. UNCE/SCI/023 of Charles University Research program. OK, MP and VK were also supported by the Czech Science Foundation (project no. 20-22092S).

Appendix A. Gresho vortex benchmark

The Gresho vortex benchmark [42] prescribes a tangential velocity component of Eulerian fluid in polar coordinates as⁸

$$u_{\theta}^0(r) = \begin{cases} 5r & \text{for } r < \frac{1}{5}, \\ 2 - 5r & \text{for } \frac{1}{5} < r < \frac{2}{5}, \\ 0 & \text{for } r > \frac{2}{5}. \end{cases}$$

The vortex is confined in a box $(-\frac{1}{2}, \frac{1}{2}) \times (-\frac{1}{2}, \frac{1}{2})$ with no-slip wall (though different variants can be found in literature). Theoretically, in the absence of viscosity, the vortex should be stationary, but obtaining this in a numerical scheme is challenging. In our numerical experiment, we simulate the flow in time-interval $[0, 1]$ and measure the error using a discretized (L^{∞}, L^2) Sobolev norm

$$e = \max_{t \in [0,1]} \sqrt{\frac{75}{4\pi} \sum_a V_a |\mathbf{u}_a - \mathbf{u}^0(\mathbf{r}_a)|^2}. \quad (11)$$

The meaning of the factor $\frac{75}{4\pi}$ is that the zero velocity field corresponds to error 1. In order to prevent formation of void space in the center of vortex, we had to include an anti-clump force term in the form

$$\mathbf{f} = \sum_b m_b \left(\frac{p_0}{\rho_a^2} + \frac{p_0}{\rho_b^2} \right) \tilde{w}'(r_{ab}) \mathbf{e}_{ab},$$

where \tilde{w} is a smoothing kernel with support radius $\frac{dr}{2}$. Additionally, we consider noise reduction by the Shepard filter

$$\tilde{\mathbf{u}}_a = \frac{1}{\gamma_a} \sum_b V_b \mathbf{u}_b w_{ab},$$

where

$$\gamma_a = \sum_b V_b w_{ab}.$$

⁸ Similar simulation of the Kepler vortex shows stability of the vortex even after 200 revolutions [43,44].

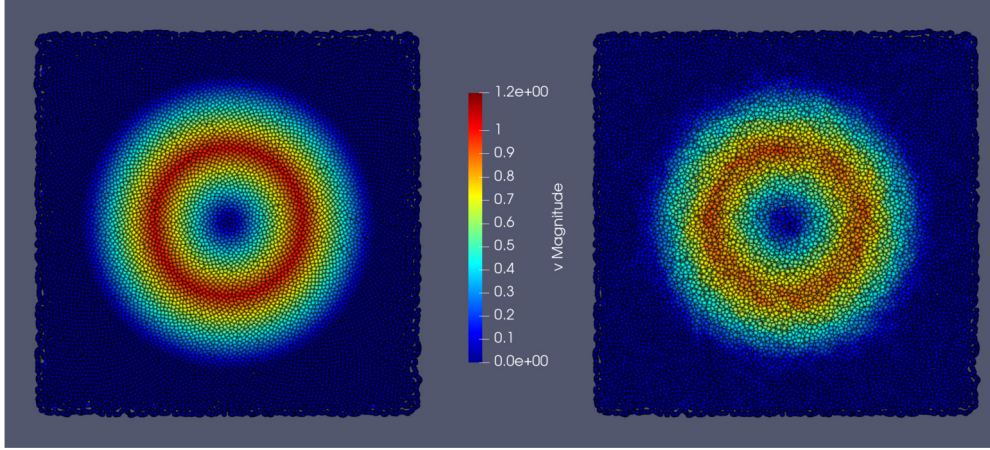


Fig. 7. Simulation result with Vogel spiral + ISC arrangement at $t = 0$ (left) and $t = 1$ (right).

Table 2

Error of Gresho vortex benchmark for different grid types (square, hexagonal, Vogel spiral, Vogel spiral + ISC) and with different types of noise filtering. The error is computed according to formula (11). It appears from data that passive (a posteriori) filter is better than active filtering (which dissipates energy). Compared to WENO method [42], numerical dissipation in symplectic WCSPH is quite strong.

| | no filter | passive filter | active filter |
|-------------|-----------|----------------|---------------|
| square | 28.16% | 12.20% | 53.07% |
| hexagonal | 27.84% | 11.77% | 55.79% |
| Vogel | 29.85% | 13.31% | 78.06% |
| Vogel + ISC | 28.19% | 11.26% | 55.25% |

Table 3

Parameters used for Gresho vortex simulation. This benchmark is dimensionless and with no gravity. Walls were implemented by two layers of dummy particles.

| | | |
|-----------------------|--------|--------|
| density | ρ | 1 |
| spatial step | dr | 1e-2 |
| num. sound speed | c | 20 |
| kernel support radius | h | 3 dr |
| box size | l | 1 |
| anti-clump pressure | p_0 | 10 |
| time step | dt | 0.1h/c |
| filter frequency | M | 30 |

This filter can be applied either in post-processing (passive filter), or by setting $\mathbf{u}_a := \hat{\mathbf{u}}_a$ every M time steps (active filter). Results are summarized in Table 2 and Fig. 7. Simulation parameters are listed in Table 3. Note that the pressure field is noisy because the noise is not suppressed by artificial dissipation [17]. However, the total energy is still conserved despite the noise. As the noise affects the quality of the solution, we opt-out for filtering it out in the post-processing rather than eliminating it in the calculation because the latter would violate our goals of global-in-time reversibility and energy conservation.

Appendix B. The Maxwell-Boltzmann entropy

In this section we derive the formula for Boltzmann entropy in terms of the Maxwell-Boltzmann distribution and, subsequently, to find its equilibrium value.

B.1. The reduced Boltzmann entropy in terms of the Maxwell-Boltzmann distribution

Let us start with the Boltzmann entropy in two dimensions expressed in terms of the one-particle distribution function $f(t, \mathbf{r}, \mathbf{p})$,

$$S^{(\text{Boltzmann})} = -k_B \int d\mathbf{r} \int d\mathbf{p} f \left(\ln(h^2 f) - 1 \right), \quad (12)$$

where the position is constrained to a box with volume V and where h is the Planck constant. This formula can be obtained for instance by the principle of maximum entropy from the Liouville entropy, from where it also follows that the one-particle distribution function is normalized to the number of particles, see [26].

Assuming that the distribution function depends only on the magnitude of the momentum (isotropic dependence), the Boltzmann entropy can be rewritten as

$$S^{(\text{Boltzmann})} = k_B N \ln \frac{e}{h^2} - 2\pi k_B V \int_0^\infty dp p f(p) \ln f(p), \quad (13)$$

where $p = |\mathbf{p}|$ is the norm of the momentum. This dependence on the one-particle distribution function $f(p)$ has to be converted to a dependence on the Maxwell-Boltzmann distribution function $f_{MB}(v)$, which tells the probability that the norm of velocity of a particle $v = p/m$ is in the interval $(v, v + dv)$. This is done using the normalization,

$$1 = \frac{1}{N} \int d\mathbf{r} \int d\mathbf{p} f = \int_0^\infty dv \frac{2\pi m^2 V}{N} v f(v), \quad (14)$$

which leads to the expression of the two-dimensional Maxwell-Boltzmann distribution function in terms of the one-particle distribution,

$$f_{MB}(v) = \frac{2\pi m^2 V}{N} v f(v), \quad (15)$$

which is normalized to unity. Note that we assume that the one-particle distribution is homogeneous in space (the total volume being V) and isotropic in momentum. These assumptions are valid in the thermodynamic equilibrium, but they approximately hold also before the equilibrium is reached, and for the purpose of showing that the Boltzmann entropy grows in our simulations, the approximation is satisfactory. Finally, the Boltzmann entropy in terms of the Maxwell-Boltzmann distribution function becomes

$$S^{(\text{Boltzmann})} - k_B N \ln \frac{e}{h^2} = -k_B N \int_0^\infty dv f_{MB}(v) \ln \left(\frac{f_{MB}(v) N}{2\pi m^2 v} \right). \quad (16)$$

Since the number of particles is conserved in our simulation, we only evaluate the part of Boltzmann entropy that varies when f_{MB} changes,

$$S_{\text{reduced}}^{(\text{Boltzmann})} = \frac{S^{(\text{Boltzmann})} - k_B N \ln \frac{e}{h^2}}{k_B N} + \ln \left(\frac{N}{2\pi m^2} \right) = - \int_0^\infty f_{MB}(v) \ln \left(\frac{f_{MB}(v)}{v} \right), \quad (17)$$

called reduced Boltzmann entropy. Note that the integral converges near the origin because the Maxwell-Boltzmann distribution typically has linear growth there.

In our simulations, this reduced Boltzmann entropy is numerically integrated using the approximate Maxwell-Boltzmann distribution function obtained from a histogram of the particle velocities at given time instant.

B.2. Equilibrium Boltzmann entropy

What is the final value of the reduced Boltzmann entropy when the system of particles reaches the thermodynamic equilibrium? This question can be answered in two steps. First, the equilibrium distribution function is calculated by the principle of maximum entropy (MaxEnt). Second, the equilibrium distribution function is plugged into the formula for the reduced Boltzmann entropy. Note, however, that the MaxEnt step depends on the energy (Hamiltonian) of the system and it depends on the complexity of the Hamiltonian whether the calculation can proceed purely analytically (without numerical solutions). Therefore, we use the simplest Hamiltonian approximating the true Hamiltonian of our SPH particles, consisting only of the kinetic energy of the particles. Maximization of the Boltzmann entropy subject to the constraints given by the total energy and total number of particles leads to the equilibrium one-particle distribution function

$$f_{\text{equilibrium}} = \frac{1}{h^2} e^{-\frac{N^*}{k_B}} e^{-\frac{E^*}{k_B} \frac{p^2}{2m}}, \quad (18)$$

where N^* and E^* are the Lagrange multipliers corresponding to the two constraints (number of particles and total energy). From the normalization it follows that $N/V = \exp(-N^*/k_B)/h^2$, while the other Lagrange multiplier can be interpreted as the inverse temperature, $E^* = 1/T$.

The equilibrium Maxwell-Boltzmann distribution function then becomes

$$f_{MB, \text{equilibrium}}(T, v) = \frac{m}{k_B T} v e^{-\frac{1}{2} m v^2}. \quad (19)$$

As time proceeds in our simulations, the histogram of particle velocities approaches the equilibrium Maxwell-Boltzmann distribution.

When this equilibrium distribution function is plugged back into the Boltzmann entropy, the reduced Boltzmann entropy becomes

$$S_{\text{(reduced)}}^{(\text{Boltzmann})}(T) = 1 + \ln \left(\frac{k_B T}{m} \right). \quad (20)$$

This equilibrium entropy, which depends on T , can be calculated once the temperature is obtained by fitting the histogram of particle velocities to the equilibrium Maxwell-Boltzmann distribution function (19). This makes sense, however, only at later stages in the simulations, when the histogram approaches the equilibrium distribution.

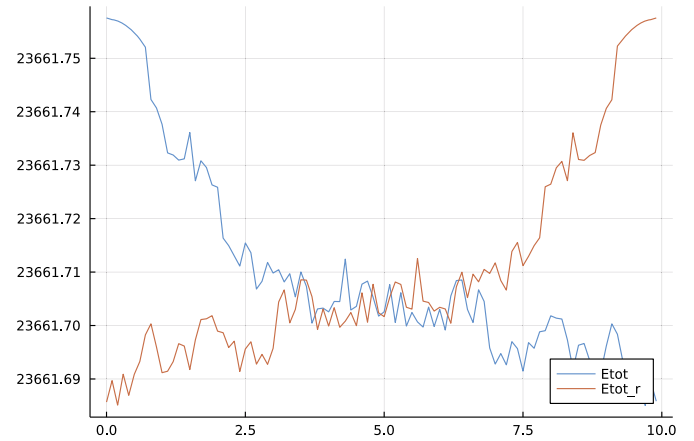


Fig. 8. Evolution of the total energy in the dam-break simulation (forward and reversed simulations). The energy oscillates within $2 \cdot 10^{-4}\%$ of the initial (exact) value.

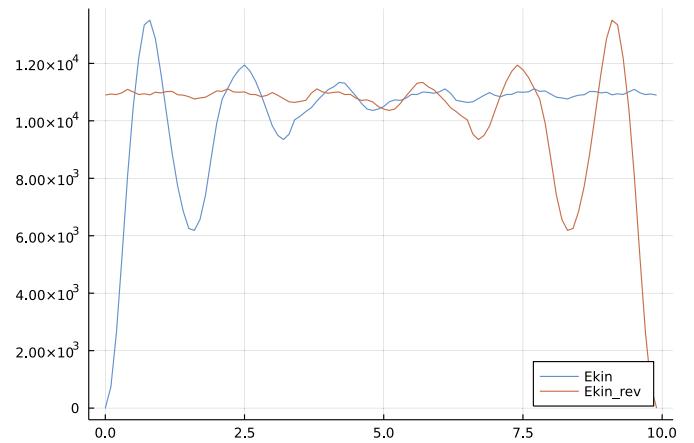


Fig. 9. Kinetic energy in the dam-break simulation (forward and reversed simulations). The energy starts from zero and then evolves in a non-monotonous way towards its maximum when the particles occupy the bottom of the container.

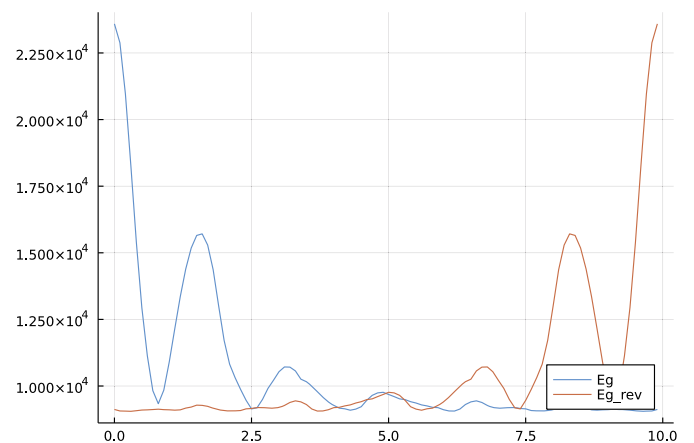


Fig. 10. Gravitational (potential) energy in the dam-break simulation (forward and reversed simulations). The energy decreases as the particles tend to occupy the bottom of the container.

Instead of using the equilibrium temperature, which makes sense only in later stages of the simulations, we can express the equilibrium entropy in terms of energy, which can be measured anytime. The total kinetic energy of the two-dimensional system of particles is equal to $E = Nk_B T$, which makes it possible to write the equilibrium entropy in terms of the energy,

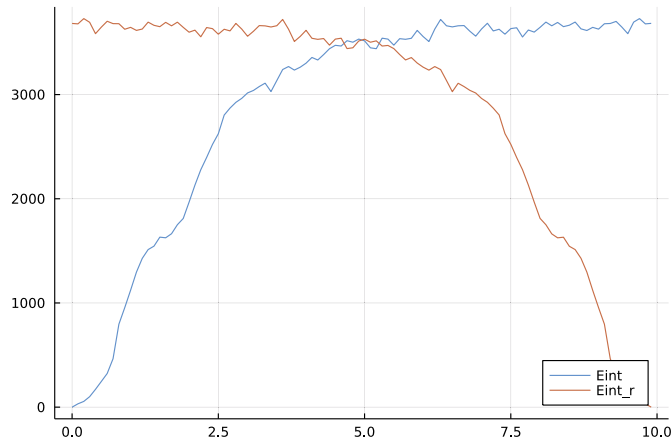


Fig. 11. Internal (or compressional) energy in the dam-break simulation (forward and reversed simulations). The energy grows from the initial condition to its maximum when the particles occupy the bottom of the container.

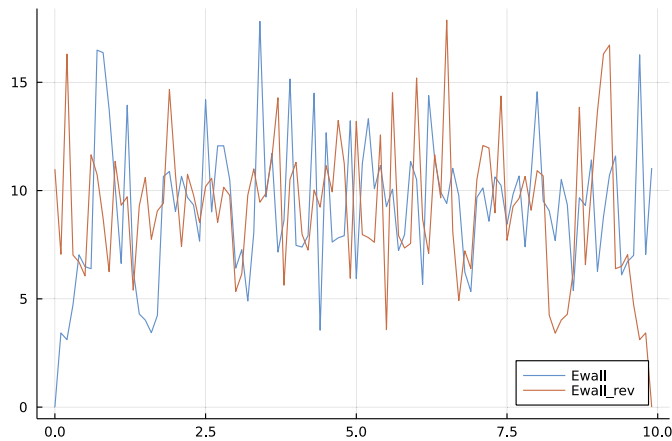


Fig. 12. The wall-fluid interaction energy in the dam-break simulation (forward and reversed simulations). Once the fluid starts interacting with the wall, the wall energy oscillates around an average value.

$$S_{(\text{reduced})}^{(\text{Boltzmann})}(E) = 1 + \ln\left(\frac{E}{Nm}\right). \quad (21)$$

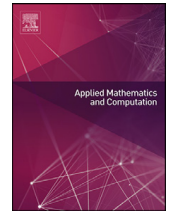
This value of equilibrium entropy is close to the Boltzmann entropy obtained directly from the approximated Maxwell-Boltzmann distribution, while the entropy based on the equilibrium temperature is only approached at later stages of the simulations.

Appendix C. Energy budget in the dam-break simulation

This Section contains the plots of various parts of the energy (gravitational, kinetic, internal, wall) and the total energy within the reversible dam-break simulation. The time-span ranges from the initial condition to the point where the particle velocities were inverted. The plots contain both the forward simulation and the backward simulation (denoted by subscript rev). See Figs. 8–12.

References

- [1] R. Gingold, J. Monaghan, *Mon. Not. R. Astron. Soc.* 181 (3) (1977) 375–389.
- [2] M. Antuono, A. Colagrossi, S. Marrone, D. Molteni, *Comput. Phys. Commun.* 181 (3) (2010) 532–549.
- [3] C. Zhang, X.Y. Hu, N.A. Adams, *J. Comput. Phys.* 335 (2017) 605–620.
- [4] D.D. Meringolo, S. Marrone, A. Colagrossi, Y. Liu, *Comput. Fluids* 179 (2019) 334–355.
- [5] M. Svård, *Phys. A, Stat. Mech. Appl.* 506 (2018) 350–375.
- [6] M. Pavelka, V. Klika, M. Grmela, *Phys. D: Nonlinear Phenom.* 399 (2019) 193–210.
- [7] Z.-F. Meng, A.-M. Zhang, P.-P. Wang, F.-R. Ming, *Comput. Methods Appl. Mech. Eng.* 386 (2021) 114082.
- [8] J. Swegle, D. Hicks, S. Attaway, *J. Comput. Phys.* 116 (1) (1995) 123–134.
- [9] T. Belytschko, Y. Guo, W. Kam Liu, S. Ping Xiao, *Int. J. Numer. Methods Eng.* 48 (9) (2000) 1359–1400.
- [10] T. Rabczuk, T. Belytschko, *Int. J. Numer. Methods Eng.* 61 (13) (2004) 2316–2343.
- [11] T. Rabczuk, T. Belytschko, *Comput. Methods Appl. Mech. Eng.* 196 (29) (2007) 2777–2799.
- [12] E. Hairer, C. Lubich, G. Wanner, *Geometric Numerical Integration: Structure-Preserving Algorithms for Ordinary Differential Equations*, Springer Series in Computational Mathematics, Springer, Berlin Heidelberg, 2013.
- [13] W. Hoover, T. Pierce, C. Hoover, J. Shugart, C. Stein, A. Edwards, *Comput. Math. Appl.* 28 (10) (1994) 155–174.
- [14] D. Violeau, *Fluid Mechanics and the SPH Method: Theory and Applications*, Oxford University Press, Oxford, UK, 2012.
- [15] A. Colagrossi, M. Landrini, *J. Comput. Phys.* 191 (2) (2003) 448–475.
- [16] J.J. Monaghan, A. Rafiee, *Int. J. Numer. Methods Fluids* 71 (5) (2013) 537–561.
- [17] M. Antuono, S. Marrone, A. Colagrossi, B. Bouscasse, *Comput. Methods Appl. Mech. Eng.* 289 (2015) 209–226.
- [18] L. Landau, E. Lifshitz, *Mechanics*, Butterworth-Heinemann, 1976.
- [19] L. Landau, E. Lifshitz, *Statistical Physics. No. pt. 1 in Course of Theoretical Physics*, Pergamon Press, 1969.
- [20] O. Kincl, M. Pavelka, *Smoothedparticles.jl*, 2021.
- [21] J. Bezanson, A. Edelman, S. Karpinski, V.B. Shah, *SIAM Rev.* 59 (1) (2017) 65–98.
- [22] J. Monaghan, *Rep. Prog. Phys.* 68 (07 2005) 1703.
- [23] M. Kroeger, M. Huetter, *Comput. Phys. Commun.* 181 (2010) 2149–2157.
- [24] L. Verlet, *Phys. Rev.* 159 (Jul 1967) 98–103.
- [25] J.J. Monaghan, *J. Comput. Phys.* 110 (2) (1994) 399–406.
- [26] M. Pavelka, V. Klika, M. Grmela, *Multiscale Thermo-Dynamics*, de Gruyter, Berlin, 2018.
- [27] B. Leimkuhler, S. Reich, *C.U. Press, Simulating Hamiltonian Dynamics*, Cambridge Monographs on Applied and Computational Mathematics, Cambridge University Press, 2004.
- [28] J. Candy, W. Rozmus, *J. Comput. Phys.* 92 (1) (1991) 230–256.
- [29] H. Rein, D. Tamayo, *Mon. Not. R. Astron. Soc.* 473 (09 2017) 3351–3357.
- [30] S. Koshizuka, Y. Oka, *Nucl. Sci. Eng.* 123 (3) (1996) 421–434.
- [31] S. Marrone, M. Antuono, A. Colagrossi, G. Colicchio, D. Le Touzé, G. Graziani, *Comput. Methods Appl. Mech. Eng.* 200 (13) (2011) 1526–1542.
- [32] S. Marrone, A. Colagrossi, A. Di Mascio, D. Le Touzé, *Phys. Rev. E* 93 (May 2016) 053113.
- [33] M. Sýkora, M. Pavelka, M. La Mantia, D. Jou, M. Grmela, *Phys. Fluids* 33 (127124) (2021).
- [34] I. Peshkov, M. Pavelka, E. Romenski, M. Grmela, *Contin. Mech. Thermodyn.* 30 (6) (2018) 1343–1378.
- [35] G. Zhong, J.E. Marsden, *Phys. Lett. A* 133 (3) (1988) 134–139.
- [36] M. Kac, *Bull. Cl. Sci., Acad. R. Belg.* 5 (42) (1956) 356–361.
- [37] P. Ehrenfest, T. Ehrenfest, *The Conceptual Foundations of the Statistical Approach in Mechanics*, Dover Books on Physics, Dover Publications, 1990.
- [38] M. Pavelka, V. Klika, M. Grmela, *J. Stat. Phys.* 181 (1) (2020) 19–52.
- [39] O.E. Lanford, in: J. Moser (Ed.), *Dynamical Systems, Theory and Applications*, in: *Lecture Notes in Physics*, vol. 38, Springer-Verlag, Berlin, 1975, pp. 1–111.
- [40] M. Pulvirenti, C. Saffirio, S. Simonella, *Rev. Math. Phys.* 26 (02) (2014) 1450001.
- [41] D. Wallace, *J. Math. Phys.* 56 (2) (2015) 022105.
- [42] H. Grimm-Strele, F. Kupka, H. Muthsam, *Comput. Phys. Commun.* 185 (3) (2014) 764–776.
- [43] A. Cartwright, D. Stamatellos, A.P. Whitworth, *Mon. Not. R. Astron. Soc.* 395 (2009) 2373–2380.
- [44] L. Cullen, W. Dehnen, *Mon. Not. R. Astron. Soc.* 408 (07 2010) 669–683.



Unified description of fluids and solids in Smoothed Particle Hydrodynamics



Ondřej Kincl^{a,*}, Ilya Peshkov^b, Michal Pavelka^a, Václav Klika^c

^a Mathematical Institute, Faculty of Mathematics, Charles University, Sokolovská 83, Prague 186 75, Czech Republic

^b Department of Civil, Environmental and Mechanical Engineering, University of Trento, Via Mesiano 77, Trento 38123, Italy

^c Dept. of Mathematics, FNSPE, Czech Technical University in Prague, Trojanova 13, Prague 120 00 Czech Republic

ARTICLE INFO

Article history:

Available online 26 October 2022

Keywords:

SPH
SHTC
Solid mechanics
Fluid dynamics
Energy-conservation
Tensile instability

ABSTRACT

Smoothed Particle Hydrodynamics (SPH) methods are advantageous in simulations of fluids in domains with free boundary. Special SPH methods have also been developed to simulate solids. However, there are situations where the matter behaves partly as a fluid and partly as a solid, for instance, the solidification front in 3D printing, or any system involving both fluid and solid phases. We develop an SPH-like method that is suitable for both fluids and solids at the same time. Instead of the typical discretization of hydrodynamics, we discretize the Symmetric Hyperbolic Thermodynamically Compatible equations (SHTC), which describe both fluids, elastic solids, and visco-elasto-plastic solids within a single framework. The resulting SHTC-SPH method is then tested on various benchmarks from the hydrodynamics and dynamics of solids and shows remarkable agreement with the data.

© 2022 Elsevier Inc. All rights reserved.

1. Introduction

We continue investigating different numerical strategies for the discretization of the unified formulation of continuum fluid and solid mechanics [1,2], which can describe flows of Newtonian and non-Newtonian fluids [3], as well as deformations of elastoplastic solids [4] in a single system of first-order hyperbolic partial differential equations. In this paper, we are particularly interested in the capabilities of the Smoothed Particle Hydrodynamics approach to capture the solution to the unified model in both fluid and solid regimes. Because the non-dissipative part of the model (all differential terms) belongs to the class of Symmetric Hyperbolic Thermodynamically compatible (SHTC) equations [5–9], we shall also refer to the unified model as the SHTC equations. Moreover, as shown in [5] the SHTC equations can also be seen as a particular realization of the GENERIC (General Equation for Non-Equilibrium Reversible-Irreversible Coupling) approach [10–12] to non-equilibrium thermodynamics. From this view point, where we emphasize thermodynamic compatibility, our approach is similar to the formulation of the SPH scheme based on the GENERIC framework [13–15]. In the long-term perspective, we, therefore, are interested in developing an SPH Hamiltonian integrator that respects various properties of the continuous equations (differential constraints, Jacobi identity, etc.) at the discrete level. This goal is partially addressed in this paper.

Previously, the unified model of continuum mechanics was discretized using various *mesh-based* techniques including Godunov-type finite volume methods and Discontinuous Galerkin methods [2], Arbitrary Lagrangian Eulerian methods [4,16], a finite volume method in the Updated Lagrangian formulation with a high-order IMEX time integrator [17], semi-implicit

* Corresponding author.

E-mail address: ondrej.kincl.6@gmail.com (O. Kincl).

staggered finite volume method [18] for low-Mach number problems, thermodynamically compatible finite volume scheme [19].

This time, we turn to the discretization of the SHTC equations with *mesh-free* methods and, in particular, with the Smoothed Particle Hydrodynamics (SPH), which is a particle-based numerical method for partial differential equations introduced by Gingold and Monaghan in 1977 [20]. The method allows for an elegant treatment of complex time-dependent geometries. This feature makes it attractive for problems involving fluid-structure interactions [21–24] and multiphase flows [25]. Despite its name, there are also numerous applications to solids [26–32]. We refer, for example, to [33] for a comprehensive review.

Although SPH methods were successfully applied to simulate fluids and solids, the schemes and equations were rather different. For example, fluid mechanics equations are formulated in the Eulerian frame, while solid mechanics equations are traditionally formulated in the Lagrangian frame. Our ultimate goal, therefore, to develop a single reliable scheme that works in both fluid and solid regimes of the SHTC equations, is far from being trivial. For example, such a goal is very appealing from the perspective of modeling material flows that exhibit coexistence of the fluid and solid states, as well as mutual transformations, e.g. selective laser metal printing (3D printing of metals), flows of viscoplastic fluids, landslides and avalanches, ice formation, etc. Another canonical example of coexistence of fluid-like and solid-like behavior is granular flows [34,35]. In particular, models for granular materials [35–37] have, in addition to the standard SPH equations for position and momentum, relationships for strain or other state variables (e.g. vorticity). Thus, granular flows with their many phases [34,35] might be also addressed in future within the SHTC-SPH framework proposed here.

Although SPH methods were successfully applied to simulate fluids and solids, the schemes and equations were rather different. For example, fluid mechanics equations are formulated in the Eulerian frame, while solid mechanics equations are traditionally formulated in the Lagrangian frame. Our ultimate goal, therefore, to develop a single reliable scheme that works in both fluid and solid regimes of the SHTC equations, is far from being trivial. For example, such a goal is very appealing from the perspective of modeling material flows that exhibit coexistence of the fluid and solid states, as well as mutual transformations, e.g. selective laser metal printing in additive manufacturing, flows of viscoplastic fluids, granular flows [34], landslides and avalanches, ice formation, etc.

Despite the fact that the SHTC equations are formulated in the Eulerian frame (which is necessary for a fluid-like motion), these equations also have a particle-like, and therefore Lagrangian, nature, which was discussed in [38]. In particular, the main field of SHTC equations that makes it possible to describe fluids and solids at once is the distortion field \mathbb{A} . This field can be seen as a field of infinitesimal local basis triads, which are allowed to arbitrary rearrange with their neighbors and thus exhibit the particle-like nature. Such a continuum description of matter was in particular inspired by Frenkel’s idea to characterize the fluidity of the liquids by the so-called characteristic particle rearrangement time τ [39,40]. Moreover, the SHTC equations can be derived by the transformation of the Lagrangian Hamiltonian continuum mechanics to the Eulerian continuum [41]. Therefore, Lagrangian particle-like methods, like the SPH scheme developed in this work, may provide an important theoretical tool to study the small scale dynamics of the distortion field in the future.

The numerical scheme proposed in this paper is based on an explicit variant of SPH. First, we perform the spatial semidiscretization of the reversible part of the SHTC system. The exact form of discrete operators is derived from a potential, which guarantees the conservation of energy without a direct discretization of the total energy conservation law. We obtain a system of ordinary differential equations, for which we find an efficient time-reversible integrator. We also discuss the problem of tensile instability and suggest a solution without interfering with the conservative properties of SPH. Finally, the irreversible part is added using the classical Runge-Kutta-4 scheme as time integrator. The last section is devoted to the validity tests.

2. Governing PDEs

The unified model of continuum fluid and solid mechanics is formulated in the Eulerian frame in a Cartesian coordinate system $\mathbf{x} = \{x_1, x_2, x_3\}$ as follows [1,2]

$$\frac{\partial \rho}{\partial t} + \nabla \cdot (\rho \mathbf{v}) = 0, \tag{1a}$$

$$\frac{\partial (\rho \mathbf{v})}{\partial t} + \nabla \cdot (\mathbf{v} \otimes \rho \mathbf{v} - \mathbb{S}) = 0, \tag{1b}$$

$$\frac{\partial \mathbb{A}}{\partial t} + \mathbf{v} \cdot \nabla \mathbb{A} + \mathbb{A} \nabla \mathbf{v} = -\frac{1}{\theta} E_{\mathbb{A}}, \tag{1c}$$

$$\frac{\partial (\rho E)}{\partial t} + \nabla \cdot (\mathbf{v} \rho E - \mathbb{S} \mathbf{v}) = 0, \tag{1d}$$

where ρ is the mass density of the material, $\mathbf{v} = \{v_1, v_2, v_3\}$ is the velocity field, $\mathbf{v} \otimes \rho \mathbf{v} = \{\rho v^i v^j\}$, $\mathbb{A} = \{A^{ij}\}$ is the distortion field, $\nabla \mathbf{v} = \{\frac{\partial v^i}{\partial x^j}\}$, $\mathbf{v} \cdot \nabla = v^i \frac{\partial}{\partial x^i}$, $\mathbb{S} = \{S^{ij}\}$ is the total stress tensor whose specification depends on the material under

consideration and is defined by the total energy density specification $E = E(\rho, \mathbf{v}, \mathbb{A}) = \epsilon(\rho, \mathbb{A}) + \frac{1}{2} \|\mathbf{v}\|^2$, see Section 3.4. In addition, $\epsilon(\rho, \mathbb{A})$ is the internal energy that must be specified by the user.

The left-hand side of the equations is the reversible part of the time evolution and can be derived either from the variational principle or can be generated by Poisson brackets [5]. This part describes the elasticity of the material. The right-hand side is characterized by the relaxation term in the distortion equation. Here, $E_{\mathbb{A}} = \frac{\partial E}{\partial \mathbb{A}}$ and is essentially the Lagrangian stress tensor (first Piola-Kirchhoff stress), while the scalar $\theta = \theta(\rho, \tau, \mathbb{A}) \geq 0$ is a relaxation function which depends on the state variables and some material constants. In particular, $\theta \sim \tau$, where τ is the strain relaxation time and one of the key elements of the SHTC model to describe fluids and solids. For example, in this framework, fluids can be seen as the relaxation limit (small relaxation time $0 < \tau \ll \infty$) of a solid when the shear stresses are strongly relaxed (“melted” solid). For Newtonian fluids τ can be taken constant, while for non-Newtonian fluids and elastoplastic solids τ is the function of the stress state [3,4], and therefore of the distortion field $\tau = \tau(\mathbb{A})$ (as well as other parameters, e.g. temperature).

As relaxation time is widely used in non-Newtonian fluid dynamics but with a slightly different meaning, e.g. [15] we further comment on the strain relaxation time τ . A viscoelastic fluid, for instance the classical Maxwell model, can be obtained from the SHTC equations if the energy does not depend directly on distortion \mathbb{A} , but rather only on the left Cauchy-Green tensor $\mathbb{B} = \mathbb{A}^{-1} \mathbb{A}^{-T}$, by projection of the dynamics of \mathbb{A} to \mathbb{B} [12]. The strain relaxation time τ then becomes the relaxation time in the Maxwell model. However, many modern extensions of the original Maxwell model implies that the stress tensor is additively decomposed into pure viscous and elastic parts [15]. In such models, the pure viscous Newtonian regime corresponds to the vanishing relaxation time (i.e. $\tau = 0$). On the other hand, a material described by the SHTC equations is never pure viscous but a viscoelastic one, i.e. the elastic component never vanishes completely, though it might be vanishingly small. Thus, the first-order Chapman-Enskog approximation of the SHTC equations in the case of sufficiently small but finite τ gives the Navier-Stokes equations [42,43]. On the other side of the spectrum of τ , in the case of no dissipation, i.e. $\tau \rightarrow \infty$, the SHTC equations are just the Eulerian evolution equations of the finite strain hyperelasticity.

For simplicity, we ignore the heat transfer effect which is also described by hyperbolic relaxation equations in the SHTC framework [5,12,18], as well as the materials are considered as isothermal. The heat conduction will be included in a follow up paper.

The following section contains a numerical method (SHTC-SPH) that finds approximate solutions of the SHTC Eq. (1) in both the fluid and solid regimes. [44]

3. The SHTC-SPH method

In order to address the SHTC Eq. (1), which contain the distortion field (unlike hydrodynamics), we have to define a discrete analogy of the continuous distortion. But before that, let us first recall the standard construction of SPH via smoothing kernels.

The SPH is based on *smoothing kernels* to calculate the influence of a particle on its surroundings. In this paper, we will use Wendland’s quintic kernel, which reads

$$w(r) = \begin{cases} \frac{\alpha_d}{h^d} \left(1 - \frac{r}{2h}\right)^4 \left(1 + \frac{2r}{h}\right), & r \leq 2h \\ 0, & r \geq 2h \end{cases} \tag{2}$$

where r is the distance from the center of the particle, h is the *smoothing length* and d is the dimension. The constant α_d normalizes w such that $\int_{\mathbb{R}^d} w = 1$ has the following values:

$$\begin{cases} \alpha_2 = \frac{7}{4\pi} \\ \alpha_3 = \frac{21}{16\pi} \end{cases} \tag{3}$$

Following Violeau [45], we will use the notation

$$w_{ab} = w(r_{ab}), \quad w'_{ab} = dw_{ab}(r_{ab}) \tag{4}$$

where $r_{ab} = |\mathbf{x}_a - \mathbf{x}_b| = |\mathbf{x}_{ab}|$ is the distance between two particles with positions $\mathbf{x}_a, \mathbf{x}_b$ in the Eulerian frame. Furthermore, let us also denote

$$\nabla w_{ab} = w'_{ab} \frac{\mathbf{x}_{ab}}{r_{ab}} \tag{5}$$

Realizing that

$$\frac{w'(r)}{r} = \begin{cases} -\frac{10\alpha_d}{h^{d+1}} \left(1 - \frac{r}{2h}\right)^3, & r \leq 2h \\ 0, & r \geq 2h \end{cases} \tag{6}$$

we can implement ∇w_{ab} in a way that avoids potential division by $r = 0$.

Moreover, in the initial state, the particles are placed in a regular pattern, filling a domain Ω_0 such that every particle occupies a volume $V_0 = \delta r^d$, where $\delta r > 0$ is the spatial step of the simulation. In the 2D case, an isometric grid arrangement

is used in this paper, while in the 3D case, the particles are initially distributed in a body-centered cubic crystal. We can now proceed to the definition of the discrete state variables.

3.1. Discrete density

Mass density can be approximated, using interpolation by smoothing kernel density ρ_a at \mathbf{x}_a , as

$$\rho_a = \sum_b m_b w_{ab} + C_{\rho,a} \tag{7}$$

where $C_{\rho,a}$ is a time-independent parameter that enforces the equality of ρ_a with the reference density ρ_0 at the initial time instant $t = 0$ (this is necessary to obtain the vanishing internal energy of the free surface particles). We assume that the masses of the particles m_b are positive and do not depend on time [46]. In all the examples presented in this paper, we use $m_b = \rho_0 V_0|_b$ where the volume of the particles follows from $V_a = (\sum_b w_{ab})^{-1}$.

A straightforward computation then yields the following formula for the differential of the discrete density.

Statement 1. Assuming $r_{ab} > 0$ for each pair of particles, the total differential of ρ_a according to formula (7) with respect to the positions of the particles \mathbf{x} is

$$d\rho_a = \sum_b m_b d\mathbf{x}_{ab} \cdot \nabla w_{ab} \tag{8}$$

3.2. Discrete distortion

An important variable in the SHTC equations is the *distortion* matrix. In the reversible (elastic) case, i.e. (1c) is homogeneous, it can be thought of as the inverse of the deformation gradient $\mathbb{F} = \frac{\partial \mathbf{x}}{\partial \mathbf{X}} = \mathbb{A}^{-1}$, and therefore it satisfies the following equation [12, Chap. 3]

$$\dot{\mathbb{A}} = -\mathbb{A}\mathbb{L}, \tag{9}$$

which is the identity following from the definition $\mathbb{A} = \frac{\partial \mathbf{x}}{\partial \mathbf{X}}$, [7]. Here, \mathbb{L} is the velocity gradient, \mathbf{X} is the Lagrangian coordinate of the continuum, and the dot denotes the material time derivative. Using a renormalized SPH gradient [47,48] inspired by work [49] by Falk and Langer, we can approximate this quantity as

$$\mathbb{L}_a = \left(\sum_b m_b \mathbf{v}_{ab} \otimes \nabla w_{ab} \right) \left(\sum_b m_b \mathbf{x}_{ab} \otimes \nabla w_{ab} \right)^{-1}. \tag{10}$$

The following statement explains that \mathbb{L}_a can be found by approximating a differential formula $d\mathbf{v} = \mathbb{L}d\mathbf{x}$:

Statement 2. Assume $r_{ab} > 0$ for each pair of particles and for any fixed particle a that there are d linearly independent vectors \mathbf{x}_{ab} satisfying $r_{ab} < 2h$. (In other words, particle a and its neighbors must not be co-planar in 3D or co-linear in 2D.) Then the matrix inverse in (10) exists and \mathbb{L}_a is the unique solution of the overdetermined system

$$\mathbb{L}_a \mathbf{x}_{ab} \doteq \mathbf{v}_{ab} \tag{11}$$

in the sense of weighted least squares with weights $m_b \frac{|w'_{ab}|}{r_{ab}}$.

Proof. Note that $|w'_{ab}| = -w'_{ab}$. It is clear from the assumptions that the matrix

$$-\sum_b m_b \mathbf{x}_{ab} \otimes \nabla w_{ab} = \sum_b \frac{m_b |w'_{ab}|}{r_{ab}} (\mathbf{x}_{ab} \otimes \mathbf{x}_{ab}) \tag{12}$$

is positive definite and thus invertible. Now, the global minimum of coercive and differentiable function

$$\mathcal{E}(\mathbb{L}_a) = -\frac{1}{2} \sum_b m_b \frac{w'_{ab}}{r_{ab}} |\mathbb{L}_a \mathbf{x}_{ab} - \mathbf{v}_{ab}|^2 \tag{13}$$

with respect to \mathbb{L}_a exists and satisfies

$$\begin{aligned} 0 &= d\mathcal{E}_a = -\sum_b m_b \frac{w'_{ab}}{r_{ab}} (\mathbb{L}_a \mathbf{x}_{ab} - \mathbf{v}_{ab}) \cdot d\mathbb{L}_a \mathbf{x}_{ab} \\ &= -d\mathbb{L}_a : \sum_b m_b (\mathbb{L}_a \mathbf{x}_{ab} - \mathbf{v}_{ab}) \otimes \nabla w_{ab}, \quad \forall d\mathbb{L}_a. \end{aligned} \tag{14}$$

This immediately yields (10). \square

As a corollary of Statement 2, it is clear that the definition (10) is first-order exact. In fact, $\mathbb{L}_a \mathbf{x}_{ab} = \mathbf{v}_{ab}$ will be solved exactly by least squares, provided that a solution exists, which is the case when \mathbf{v} can be written as a linear function of \mathbf{x} .

Combining (9) with (10), we obtain the evolution of \mathbb{A}_a in the form

$$\dot{\mathbb{A}}_a = -\mathbb{A}_a \left(\sum_b m_b \mathbf{v}_{ab} \otimes \nabla w_{ab} \right) \left(\sum_b m_b \mathbf{x}_{ab} \otimes \nabla w_{ab} \right)^{-1}. \tag{15}$$

Since $\mathbf{v}_a = \dot{\mathbf{x}}_a$, we can write this as a linear relation between total differentials of \mathbb{A}_a and \mathbf{x}_a with respect to time:

$$d\mathbb{A}_a = -\mathbb{A}_a \left(\sum_b m_b d\mathbf{x}_{ab} \otimes \nabla w_{ab} \right) \left(\sum_b m_b \mathbf{x}_{ab} \otimes \nabla w_{ab} \right)^{-1}, \tag{16}$$

Here, we have a subtle problem because we do not have any guarantee that the right-hand side in (16) is integrable – that is, unlike for density (see (7)), we do not have a closed formula for $\mathbb{A}_a = \mathbb{A}_a(\mathbf{x})$. Therefore, when Γ is a closed loop in the configuration space, one, in general, has

$$\int_{\Gamma} d\mathbb{A}_a \neq 0. \tag{17}$$

In other words, if (16) is used, the numerical distortion may not exactly recover its initial value when the shape of a material does, potentially introducing some artificial *inelasticity* and small local residual stresses. Without resorting to the Lagrangian description [50], we have not found a satisfactory solution to this problem in pure Eulerian settings.

On a side note, instead of treating the density as a separate variable, it is possible to use

$$\rho_a = \rho_0 \det \mathbb{A}_a. \tag{18}$$

However, in our numerical experiments, using formula (7) appeared to be more reliable.

3.3. Reversible part of the SHTC-SPH equations

Let us now consider the case of an elastic solid with internal energy

$$\mathcal{U} = \int_{\Omega} \rho \epsilon dx. \tag{19}$$

which we discretize as

$$\mathcal{U}_h = \sum_a m_a \epsilon_a, \tag{20}$$

where $\epsilon_a = \epsilon(\rho_a, \mathbb{A}_a)$ is the specific internal energy. For simplicity of notation, let us write

$$\mathbb{H}_a = \sum_b m_b \mathbf{x}_{ab} \otimes \nabla w_{ab} \tag{21a}$$

$$\mathbb{T}_a = -\epsilon_{\rho_a} \mathbb{I} + \mathbb{A}_a^T \epsilon_{\mathbb{A}_a} \mathbb{H}_a^{-1}, \tag{21b}$$

where we employed the usual notation for partial derivatives $\epsilon_{\rho_a} = \frac{\partial \epsilon}{\partial \rho_a}$, $\epsilon_{\mathbb{A}_a} = \frac{\partial \epsilon}{\partial \mathbb{A}_a}$. Here, \mathbb{H}_a is a renormalization matrix with units of density that appeared in definition of the discrete velocity gradient (10) and is usually negative definite. Matrix \mathbb{T}_a represent the stress on particle a . Now, using (8), (16), we find how \mathcal{U} varies when \mathbf{x} changes:

$$\begin{aligned} d\mathcal{U}_h &= \sum_a m_a \epsilon_{\rho_a} d\rho_a + \sum_a m_a \epsilon_{\mathbb{A}_a} : d\mathbb{A}_a \\ &= \sum_{a,b} m_a m_b \left(\epsilon_{\rho_a} \nabla w_{ab} \cdot d\mathbf{x}_{ab} - \epsilon_{\mathbb{A}_a} : \mathbb{A}_a (d\mathbf{x}_{ab} \otimes \nabla w_{ab}) \mathbb{H}_a^{-1} \right) \\ &= -\sum_{a,b} m_a m_b \mathbb{T}_a \nabla w_{ab} \cdot d\mathbf{x}_{ab} \\ &= -\sum_{a,b} m_a m_b (\mathbb{T}_a + \mathbb{T}_b) \nabla w_{ab} \cdot d\mathbf{x}_a. \end{aligned} \tag{22}$$

Combining (15), (22) and $m_a \dot{\mathbf{v}}_a = -\frac{\partial \mathcal{U}_h}{\partial \mathbf{x}_a}$ (Newton's second law), we obtain a system of ordinary differential equations:

$$\begin{aligned} \dot{\mathbf{x}}_a &= \mathbf{v}_a \\ \dot{\mathbf{v}}_a &= \sum_b m_b (\mathbb{T}_a + \mathbb{T}_b) \nabla w_{ab} \\ \dot{\mathbb{A}}_a &= -\mathbb{A}_a \mathbb{L}_a, \end{aligned} \tag{23}$$

which is the system of the SHTC-SPH ordinary differential equations approximating the SHTC equations.

One of the greatest assets of SHTC-SPH is that it enjoys various conservative properties.

Statement 3. The system of Eq. (23) satisfies the conservation of the

- energy

$$\mathcal{H}_h = \sum_a m_a \left(\frac{v_a^2}{2} + \epsilon_a \right), \tag{24}$$

- linear momentum

$$\mathbf{M}_h = \sum_a m_a \mathbf{v}_a, \tag{25}$$

- angular momentum (provided that the shear stress tensor $\mathbb{A}_a^T \in \mathbb{A}_a$ is symmetric)

$$\mathbf{L}_h = \sum_a m_a \mathbf{x}_a \times \mathbf{v}_a. \tag{26}$$

Proof. Conservation of energy follows from the construction, linear momentum is conserved due to antisymmetry $\nabla w_{ab} = -\nabla w_{ba}$. Likewise, showing conservation of angular momentum is easy because

$$\begin{aligned} \dot{\mathcal{L}}_h^i &= \epsilon^{ijk} \sum_a m_a x_a^j \dot{v}_a^k \\ &= \epsilon^{ijk} \sum_a m_a x_a^j \left(\sum_b m_b (T_a^{kl} + T_b^{kl}) \nabla_{ab} w^l \right) \\ &= \epsilon^{ijk} \sum_a m_a T_a^{kl} \left(\sum_b m_b x_{ab}^i \nabla_{ab} w^l \right) \\ &= \epsilon^{ijk} \sum_a m_a T_a^{kl} H_a^{li} \\ &= 0 \end{aligned} \tag{27}$$

since the matrix $\mathbb{T}_a \mathbb{H}_a$ is symmetric. \square

3.4. Constitutive equations

The set of Eq. (23) is incomplete until one specifies the dependence of internal energy ϵ on ρ, \mathbb{A} . In this paper, we assume that the energy $\epsilon(\rho, \mathbb{A})$ can be additively decomposed as

$$\epsilon(\rho, \mathbb{A}) = \epsilon_0(\rho) + \epsilon_s(\rho, \mathbb{A}), \tag{28}$$

where $\epsilon_0(\rho)$ may depends only on density and represents stored energy due to volumetric changes in the continuum. In general, it is convenient to chose ϵ_0 in such a way that in the ideal fluid limit (Euler equations), it recovers some known equations of state (e.g. ideal gas, stiffened gas, MieGrneisen, etc.). In particular, we shall use the following simple quadratic relation

$$\epsilon_0(\rho) = \frac{c_0^2}{2} \left(\frac{\rho}{\rho_0} - 1 \right)^2, \tag{29}$$

with constant c_0 taken equal to the bulk sound velocity in the case of small deformations, and ρ_0 being a reference density. In principle, arbitrary physically meaningful formula can be used instead (29) (e.g. [2,12]), but for the prove of concept, (29) is sufficiently general. From (29), we can deduce an expression for the pressure:

$$p = \rho^2 \frac{\partial \epsilon_0}{\partial \rho} = c_0^2 \rho_0 \left(1 - \frac{\rho_0}{\rho} \right). \tag{30}$$

On the other hand, $\epsilon_s(\rho, \mathbb{A})$ represents stored elastic energy due to tangential deformations. It, however, may contain volumetric contribution as well. In this paper, we use two variants for $\epsilon(\rho, \mathbb{A})$. Following the papers [2], we can use

$$\epsilon_s^{DPRZ}(\mathbb{A}) = \frac{c_s^2}{4} \|\text{dev}(\mathbb{A}^T \mathbb{A})\|_F^2, \tag{31}$$

where c_s is set to be equal to the shear speed of sound so that in the case of small deformations, the Hook law of linear elasticity is recovered, $\|\cdot\|_F$ is the Frobenius norm and

$$\text{dev} \mathbb{M} = \mathbb{M} - \frac{1}{3} (\text{tr} \mathbb{M}) \mathbb{I} \tag{32}$$

denotes deviatoric part. Plugging this into (21b), we get

$$\mathbb{T}_a = -\frac{p_a}{\rho_a} \mathbb{I} + c_s^2 \mathbb{A}_a^T \mathbb{A}_a \operatorname{dev}(\mathbb{A}_a^T \mathbb{A}_a) \mathbb{H}_a^{-1}. \tag{33}$$

Remark that formula (31) implicitly depends on density through $\det \mathbb{A} = \rho/\rho_0$. Indeed, if a_k are the singular values of \mathbb{A} then it can be shown that

$$\begin{aligned} \epsilon_s^{DPRZ}(\mathbb{A}) &= \frac{1}{6} \left((a_1 - a_2)^2 + (a_2 - a_3)^2 + (a_3 - a_1)^2 \right) \\ &\quad + \frac{8}{3} \left(a_1^2 a_2^2 \left(1 - \frac{1}{2} \left(\frac{a_1}{a_2} + \frac{a_2}{a_1} \right) \right) + a_2^2 a_3^2 \left(1 - \frac{1}{2} \left(\frac{a_2}{a_3} + \frac{a_3}{a_2} \right) \right) + a_3^2 a_1^2 \left(1 - \frac{1}{2} \left(\frac{a_3}{a_1} + \frac{a_1}{a_3} \right) \right) \right) \end{aligned} \tag{34}$$

where, in particular, it is clear that the second part of the formula depends on $\det \mathbb{A} = a_1 a_2 a_3$. This results in a non-zero trace of the stress tensor, which is, however, vanishingly small in the case of small deformations. Other options for ϵ_s which give exactly trace-free stress are available in the literature, e.g. see [51].

It is also possible to use the Neo-Hookean model

$$\epsilon_s^{NH}(\mathbb{A}) = \frac{c_s^2}{2} (\operatorname{tr} \mathbb{B}_a - 3 + 2 \ln \det \mathbb{A}_a), \tag{35}$$

which yields:

$$\mathbb{T}_a = -\frac{p_a}{\rho_a} \mathbb{I} - c_s^2 (\mathbb{B}_a - \mathbb{I}) \mathbb{H}_a^{-1}, \tag{36}$$

with $\mathbb{B}_a = \mathbb{A}_a^{-1} \mathbb{A}_a^{-T}$ being the left Cauchy-Green tensor and the pressure in a particle follows from (30) as

$$p_a = c_0^2 \rho_0 \left(1 - \frac{\rho_0}{\rho_a} \right). \tag{37}$$

3.5. Tensile penalty

A common issue encountered in SPH is the *tensile instability* – a numerical artifact, which causes unwanted clumping of particles in regions of negative pressure. Due to non-linearities in formula (7), density ρ will increase slightly under tensile strain. This is usually not a problem for $p > 0$, however, for $p < 0$ particles can reduce their potential by tensile strain according to

$$\frac{\epsilon}{\partial \rho} = \frac{p}{\rho^2}. \tag{38}$$

This often results in the formation of particle chains surrounded by void patches, which can eventually cause body tearing. There are a few remedies offered in the literature. Monaghan [52] recommends adding an artificial force that repels particles with abnormally small separation. Another possible treatment is based on the idea of particle shifting (typically due to an artificial Fickian diffusion) which prevents highly anisotropic particle distributions and hence reduce the onset of numerical instability in both the internal and free boundary flows [53,54].

In this paper, we suggest adding the following *tensile penalty* term to the energy:

$$\mathcal{P}_h = \frac{1}{2} \sum_a m_a c_p^2 \left(\frac{\lambda_a}{\rho_0} \right)^2, \tag{39}$$

where c_p is a numerical parameter with the dimension of velocity and that determines the strength of anti-clumping forces. The variable λ_a is defined by the relation

$$\lambda_a = h \frac{\partial \rho_a}{\partial h} + C_{\lambda,a} = \sum_b m_b h \frac{\partial w_{ab}}{\partial h} + C_{\lambda,a}. \tag{40}$$

Our idea is to describe clustering as a situation where ρ_a increases when we take a smaller smoothing length h . By adding this energy term, we enforce a desired distribution of the particles by keeping $\frac{\partial \rho_a}{\partial h}$ small. Similarly to (7), we add a time-independent parameter $C_{\lambda,a}$ to ensure that $\lambda_a = 0$ at the initial time. The potential \mathcal{P}_h then generates an additional force

$$-\frac{\partial \mathcal{P}_h}{\partial \mathbf{x}_a} = -\sum_b m_a m_b c_p^2 \frac{\lambda_a + \lambda_b}{\rho_0^2} h \frac{\partial \nabla w_{ab}}{\partial h} \tag{41}$$

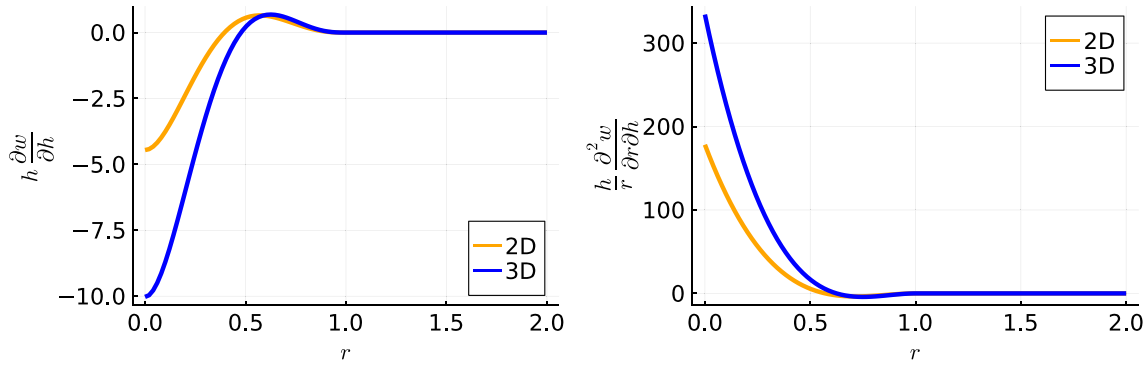


Fig. 1. The plot of $h \frac{\partial w}{\partial h}$ (left) and $\frac{h}{r} \frac{\partial^2 w}{\partial r \partial h}$ (right) in two and three dimensions for $h = 1$.

so that the updated balance of momentum reads

$$\begin{aligned} \dot{\mathbf{v}}_a &= \sum_b m_b (\mathbb{T}_a + \mathbb{T}_b) \nabla w_{ab} \\ &\quad - \sum_b m_b c_p^2 \frac{\lambda_a + \lambda_b}{\rho_0^2} \frac{h}{r_{ab}} \frac{\partial^2 w_{ab}}{\partial r_{ab} \partial h} \mathbf{x}_{ab}. \end{aligned} \tag{42}$$

Restricting ourselves to the Wendland’s kernel (2), we can provide these explicit formulas:

$$h \frac{\partial w}{\partial h} = \begin{cases} \frac{7}{4\pi h^2} \left(1 - \frac{r}{2h}\right)^3 \left(7\left(\frac{r}{h}\right)^2 - \frac{3r}{h} - 2\right) & r \leq 2h \\ 0 & r \geq 2h \end{cases}, \tag{43}$$

$$\frac{h}{r} \frac{\partial^2 w}{\partial r \partial h} = \begin{cases} -\frac{35}{4\pi h^4} \left(1 - \frac{r}{2h}\right)^2 \left(\frac{7r}{h} - 8\right) & r \leq 2h \\ 0 & r \geq 2h \end{cases} \tag{44}$$

in 2D, and

$$h \frac{\partial w}{\partial h} = \begin{cases} \frac{21}{32\pi h^3} \left(1 - \frac{r}{2h}\right)^3 \left(16\left(\frac{r}{h}\right)^2 - \frac{9r}{h} - 6\right) & r \leq 2h \\ 0 & r \geq 2h \end{cases}, \tag{45}$$

$$\frac{h}{r} \frac{\partial^2 w}{\partial r \partial h} = \begin{cases} -\frac{105}{16\pi h^5} \left(1 - \frac{r}{2h}\right)^2 \left(\frac{4r}{h} - 5\right) & r \leq 2h \\ 0 & r \geq 2h \end{cases} \tag{46}$$

in 3D.

From the graphs in Fig. 1, we can intuitively understand the behavior of artificial force in (42) as follows: for evenly distributed particles (such as in a grid), λ_a will be close to zero, since this is the average value of $h \frac{\partial w}{\partial h}$ inside the ball of radius $2h$ (or disc in 2D). However, λ_a will be negative when the particle a is found in a cluster or chain of particles surrounded by a void. This activates the artificial force, whose magnitude is proportional to $\frac{h}{r} \frac{\partial^2 w}{\partial r \partial h}$. This makes it strongly repulsive for nearby particles and slightly attractive for relatively large separations within the particle’s sphere of influence. Thus, we get a modification of the equations similar to Monaghan’s anti-clump term but with the additional benefit that the energy is conserved, albeit in a modified form, and, as we will see in the next section, the contribution of \mathcal{P}_h to the total energy is usually small.

3.6. Time integrator

So far, we have only been concerned with the spatial semi-discretization (discrete space, continuous time), and a time integrator is required to solve the SHTC-SPH ordinary differential equations (ODE). ODE system (23) conserve energy, and we would like to find a time integrator that preserves this property. First, let us write the system in a more succinct form:

$$\begin{aligned} \dot{\mathbf{x}}_a &= \mathbf{v}_a, \\ \dot{\mathbf{v}}_a &= \frac{\mathbf{f}_a}{m_a}, \\ \dot{\mathbb{A}}_a &= -\mathbb{A}_a \mathbb{L}_a, \end{aligned} \tag{47}$$

where the force

$$\mathbf{f}_a = \sum_b m_a m_b \left(\mathbb{T}_a(\mathbf{x}, \rho, \mathbb{A}) + \mathbb{T}_b(\mathbf{x}, \rho, \mathbb{A}) \right) \nabla w_{ab} - \sum_b m_a m_b c_p^2 \frac{\lambda_a + \lambda_b}{\rho_0^2} \frac{h}{r_{ab}} \frac{\partial^2 w_{ab}}{\partial r_{ab} \partial h} \mathbf{x}_{ab}. \tag{48}$$

depends on \mathbf{x} , \mathbb{A} , ρ and λ . However, from Eqs. (7), (40), we see that ρ and λ are themselves merely functions of \mathbf{x} , and thus we have $\mathbf{f}_a = \mathbf{f}_a(\mathbf{x}, \mathbb{A})$. For the discrete velocity gradient, we can write $\mathbb{L}_a = \mathbb{L}_a(\mathbf{x}, \mathbf{v})$.

Naturally, we would like to use a symplectic integrator, such as the Verlet scheme, which has excellent energy-conservation properties [55]. Unfortunately, system (47) is not symplectic due to the presence of variable \mathbb{A}_a . Instead, we suggest the following combination of Verlet (for \mathbf{x} and \mathbf{v}) and the mid-point rule (for \mathbb{A}):

$$\begin{aligned} \mathbf{v}_a(t_{k+\frac{1}{2}}) &= \mathbf{v}_a(t_k) + \frac{\delta t}{2m_a} \mathbf{f}_a(t_k), \\ \mathbf{x}_a(t_{k+\frac{1}{2}}) &= \mathbf{x}_a(t_k) + \frac{\delta t}{2} \mathbf{v}_a(t_{k+\frac{1}{2}}), \\ \mathbb{A}_a(t_{k+1}) &= \mathbb{A}_a(t_k) \left(\mathbb{I} - \frac{\delta t}{2} \mathbb{L}_a(t_{k+\frac{1}{2}}) \right) \left(\mathbb{I} + \frac{\delta t}{2} \mathbb{L}_a(t_{k+\frac{1}{2}}) \right)^{-1}, \\ \mathbf{x}_a(t_{k+1}) &= \mathbf{x}_a(t_{k+\frac{1}{2}}) + \frac{\delta t}{2} \mathbf{v}_a(t_{k+\frac{1}{2}}), \\ \mathbf{v}_a(t_{k+1}) &= \mathbf{v}_a(t_{k+\frac{1}{2}}) + \frac{\delta t}{2m_a} \mathbf{f}_a(t_{k+1}), \end{aligned} \tag{49}$$

where $t_k = k \delta t$ denotes the k -th time-step, and $\mathbf{f}_a(t)$, $\mathbb{L}_a(t)$ is a shorthand notation for

$$\mathbf{f}_a(t) = \mathbf{f}_a(\mathbf{x}(t), \mathbb{A}(t)), \quad \mathbb{L}_a(t) = \mathbb{L}_a(\mathbf{x}(t), \mathbf{v}(t)). \tag{50}$$

From the practical standpoint, this scheme is explicit in the sense that there are no linear or non-linear systems to be solved, or matrices to be inverted, except those of size $d \times d$. The main motivation for using (49) is to obtain discrete time-reversibility as in [46]. Indeed, inverting the sign of \mathbf{v}_a and \mathbb{L}_a in (49), we get the exactly same set of equations with the swapped role of t_k and t_{k+1} .

3.7. Adding relaxation

We now have a discrete system for elastic solid in terms of arrays \mathbf{x} , \mathbf{v} , \mathbb{A} , which constitutes the reversible part of SHTC framework. The last step is adding fluidity to our model by relaxing \mathbb{A} , and hence tangential stresses. Let us return to semi-discrete differential system (47), where we add relaxation as¹

$$\dot{\mathbf{x}}_a = \mathbf{v}_a, \tag{51a}$$

$$\dot{\mathbf{v}}_a = \frac{\mathbf{f}_a}{m_a}, \tag{51b}$$

$$\dot{\mathbb{A}}_a = -\mathbb{A}_a \mathbb{L}_a - \frac{3}{\tau c_s^2} \epsilon_{\mathbb{A}_a}, \tag{51c}$$

where τ is the *relaxation time* (noting that the potential equilibrium of \mathbb{A} is $\mathbb{A} = \mathbb{Q}$ with \mathbb{Q} being an orthogonal matrix). For an elastic solid $\tau = \infty$ and for a Newtonian fluid τ is a constant, while for non-Newtonian fluids and elastoplastic solids it should be taken as a function of \mathbb{A}_a [3,4]. With this new addition, the equation for \mathbb{A}_a is often stiff, and therefore, implicit and exponential time integrators are recommended [2,17]. However, we already have a very small time step in our explicit SHTC-SPH integrator (as opposed to fully implicit finite element or finite volume approaches), so for performance reasons, we use a simpler splitting strategy, using the classical Runge-Kutta-4 (RK4) scheme [55] for integrating the relaxation term in the PDE for \mathbb{A}_a :

$$\mathbf{v}_a(t_{k+\frac{1}{2}}) = \mathbf{v}_a(t_k) + \frac{\delta t}{2m_a} \mathbf{f}_a(t_k), \tag{52a}$$

$$\mathbf{x}_a(t_{k+\frac{1}{2}}) = \mathbf{x}_a(t_k) + \frac{\delta t}{2} \mathbf{v}_a(t_{k+\frac{1}{2}}), \tag{52b}$$

¹ The function θ in (1c) is taken as $\theta = \frac{\tau c_s^2}{3} (\det \mathbb{A})^{-5/3}$, see [2]. However, we omit the factor $(\det \mathbb{A})^{-5/3}$ in this paper for simplicity because it is important only in the case of compressible viscous fluids which we shall not consider here.

Table 1
Summary of simulation parameters used in this paper.

| | model | dr | dt | c ₀ | c _s | c _p | h |
|----------------------------|-------|----------|----------|----------------|----------------|----------------|----------|
| Beryllium plate | DPR | 2.50E-04 | 9.05E-10 | 9.05E+03 | 9.05E+03 | 9.05E+04 | 3.75E-04 |
| Twisting column | NH | 4.96E-02 | 3.44E-06 | 7.15E+02 | 7.19E+01 | 7.15E+03 | 7.44E-02 |
| Taylor-Couette flow | DPR | 3.33E-02 | 3.31E-05 | 2.00E+01 | 4.00E+01 | 2.00E-01 | 5.00E-02 |
| Lid-driven cavity, Re 100 | DPR | 5.00E-03 | 1.50E-05 | 2.00E+01 | 2.00E+01 | 0.00E+00 | 7.50E-03 |
| Lid-driven cavity, Re 400 | DPR | 7.14E-03 | 3.75E-06 | 2.00E+01 | 2.00E+01 | 0.00E+00 | 1.07E-02 |
| Lid-driven cavity, Re 1000 | DPR | 7.14E-03 | 1.50E-06 | 2.00E+01 | 2.00E+01 | 0.00E+00 | 1.07E-02 |

$$\mathbb{A}_a(t_k^*) = \mathbb{A}_a(t_k) \left(\mathbb{I} - \frac{\delta t}{2} \mathbb{L}_a(t_{k+\frac{1}{2}}) \right) \left(\mathbb{I} + \frac{\delta t}{2} \mathbb{L}_a(t_{k+\frac{1}{2}}) \right)^{-1}, \tag{52c}$$

$$\mathbb{A}_a(t_{k+1}) = \mathbb{A}_a(t_k^*) + \frac{\delta t}{6} \left(\mathbb{K}_{1,a}(t_k^*) + 2\mathbb{K}_{2,a}(t_k^*) + 2\mathbb{K}_{3,a}(t_k^*) + \mathbb{K}_{4,a}(t_k^*) \right), \tag{52d}$$

$$\mathbf{x}_a(t_{k+1}) = \mathbf{x}_a(t_{k+\frac{1}{2}}) + \frac{\delta t}{2} \mathbf{v}_a(t_{k+\frac{1}{2}}), \tag{52e}$$

$$\mathbf{v}_a(t_{k+1}) = \mathbf{v}_a(t_{k+\frac{1}{2}}) + \frac{\delta t}{2m_a} \mathbf{f}_a(t_{k+1}), \tag{52f}$$

where

$$\mathbb{K}_{i,a}(t_k^*) = -\frac{3}{\tau c_s^2} \epsilon_{\mathbb{A}_a} \Big|_{\mathbb{A}=\mathbb{A}(t_k^*)+b_i \delta t \mathbb{K}_{i-1,a}(t_k^*)}, \quad i = 1, 2, 3, 4 \tag{53}$$

and $(b_1, b_2, b_3, b_4) = (1, \frac{1}{2}, \frac{1}{2}, 1)$. Therefore, we get relatively cheap time steps and for $\tau = \infty$ (no relaxation) the scheme reduces to the reversible one (49).

Since positions are updated twice per step, we also require two neighbor list calculations in each iteration of (49).

4. Numerical results

As we have introduced the new SHTC-SPH numerical scheme, the following section contains the numerical results for both fluids and solids to demonstrate the robustness of the proposed SHTC-SPH approach. For a list of all the material and SPH parameters used in different test cases, we refer to Table 1.

4.1. Beryllium plate

This benchmark examines the two-dimensional oscillation of an elastic solid that is bending due to a velocity field prescribed at $t = 0$. The body in question is a translationally symmetric plate, whose cross section is a rectangle

$$\Omega = \left(-\frac{L}{2}, \frac{L}{2} \right) \times \left(-\frac{W}{2}, \frac{W}{2} \right) \tag{54}$$

with values $L = 0.06 \text{ m}$ and $W = 0.01 \text{ m}$. The initial velocity field in this cross section is

$$\mathbf{v} = A\omega \begin{pmatrix} 0 \\ a_1(\sinh s + \sin s) - a_2(\cosh s + \cos s) \end{pmatrix} \tag{55}$$

where $s = \alpha(x + \frac{1}{2})$ and $A, \omega, a_1, a_2, \alpha$ are constants with values (parameters retrieved from [17]):

$$\begin{aligned} A &= 4.3369 \cdot 10^{-5} \text{ m}, \\ \omega &= 2.3597 \cdot 10^5 \text{ s}^{-1}, \\ \alpha &= 78.834, \\ a_1 &= 56.6368, \\ a_2 &= 57.6455. \end{aligned} \tag{56}$$

We use the constitutive relation (29)–(31) for with

$$c_0 = c_s = 9046.59 \text{ m}\cdot\text{s}^{-1}. \tag{57}$$

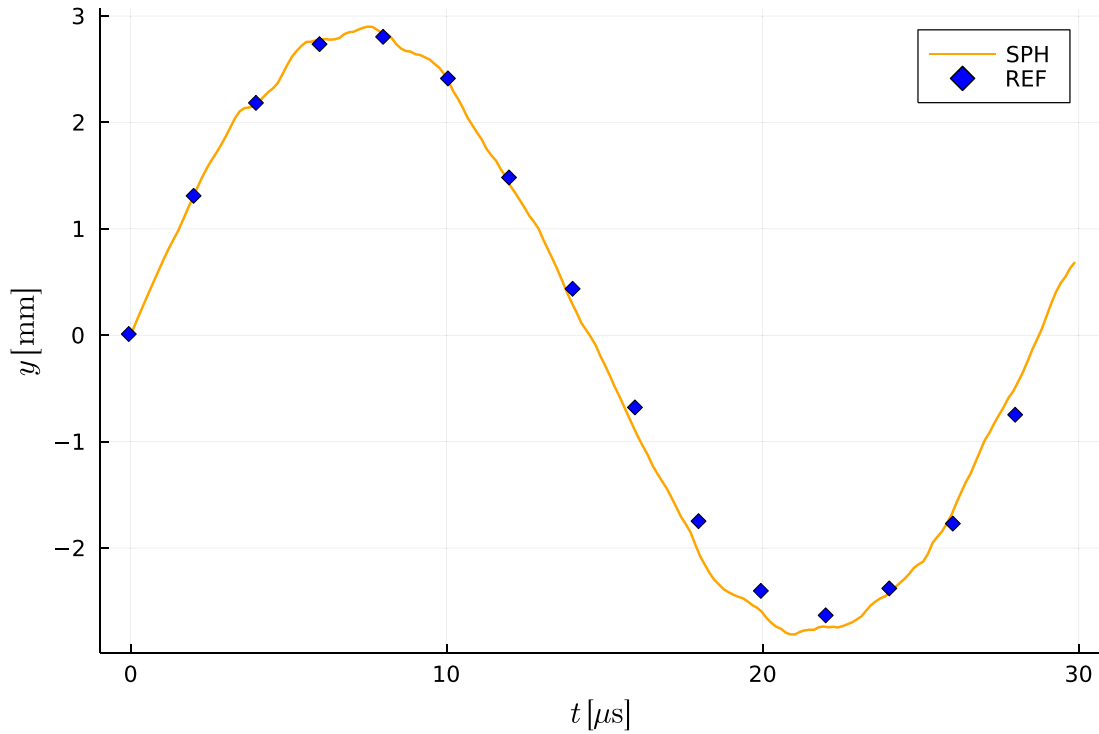


Fig. 2. The y coordinate of center point in beryllium plate benchmark plotted against time. Orange line depicts the result of our scheme. Blue squares mark the referential solution.

Complete elasticity is assumed and therefore $\tau = \infty$. We choose the spatial step $\delta r = W/40$ which gives us approximately 10 000 particles. The time step is selected according to

$$\delta t = \frac{0.05\delta r}{\sqrt{c_0^2 + \frac{4}{3}c_s^2}} \tag{58}$$

and the simulation ends at time $t = 3 \cdot 10^{-5}$ s, roughly corresponding to one period of the oscillating motion.

Three things can be tested in this benchmark. Firstly, we plot the y coordinate of the central point, which we then compare to data from the finite volume simulation [17]. Fig. 2 shows that we get a reasonable agreement. Secondly, since there are no dissipative or external forces involved, it presents an ideal test for verifying the conservation of energy, which we achieve to a reasonable degree, see Fig. 3. One can see some high frequency energy oscillations. These are likely caused by secondary vibrating modes. The same effect was observed in [4]. The relative total energy error is within $5 \cdot 10^{-6}$. Note that the kinetic energy decays slightly over time. This behavior can be explained by statistical second law of thermodynamics. Indeed, although we have no heat production terms in our equations, almost no total energy losses and reversible equations (up to round-off errors), the non-linearity and many degrees of freedom make disorder a self-emergent property. As a result, we can see irreversible transformations of one type of energy into another, e.g. transformation of the total kinetic energy into the shear elastic energy. The distribution of energy in the final "thermal equilibrium" could be estimated for instance by means of the virial theorem [56].

Last but not least, due to the presence of strongly negative pressures, this simulation poses a challenge with respect to tensile instability, demonstrating the usefulness of the penalty term (39). In fact, without this addition, the plate would tear completely as can be seen in Fig. 4. Interestingly, the tensile penalty contribution is kept relatively small despite its profound importance in the evolution.

4.2. Twisting column

The next benchmark is borrowed from [57]. The initial setup is a cuboid

$$\Omega = \left(-\frac{W}{2}, \frac{W}{2}\right) \times \left(-\frac{W}{2}, \frac{W}{2}\right) \times (0, H) \tag{59}$$

where $W = 1m$ and $H = 6m$ which is subjected to a prescribed velocity field

$$\mathbf{v} = \omega \sin\left(\frac{\pi z}{2H}\right) \begin{pmatrix} y \\ -x \\ 0 \end{pmatrix}, \tag{60}$$

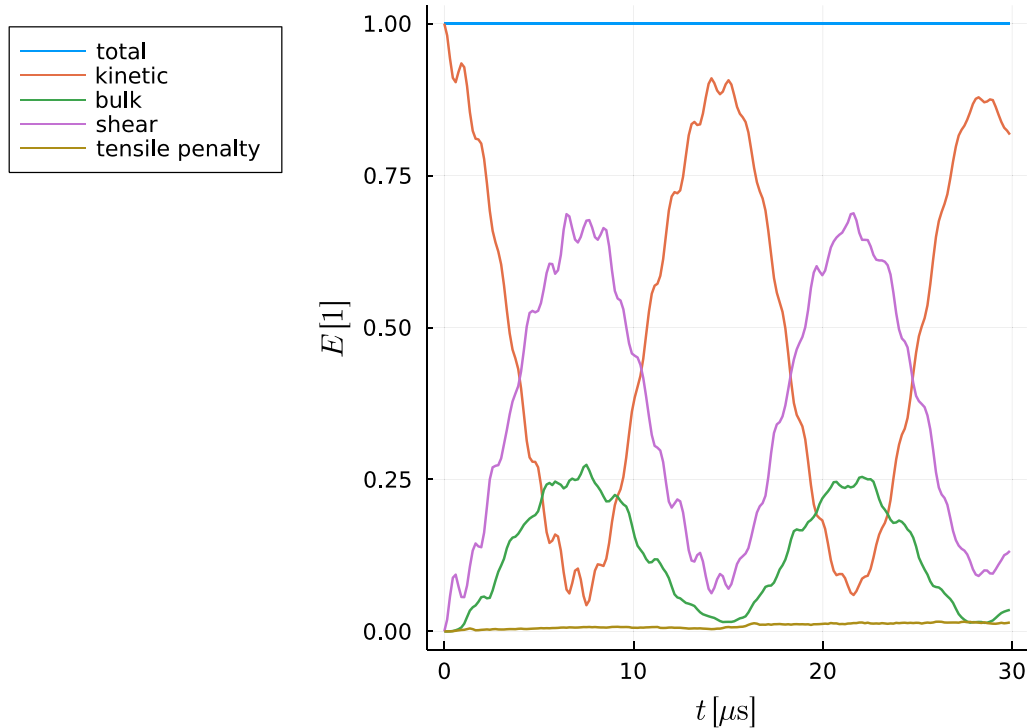


Fig. 3. Different contributions to energy in beryllium plate benchmark plotted against time, normalized. The relative total energy error is within $5 \cdot 10^{-6}$.

where $\omega = 105 \text{ s}^{-1}$. The base of the column is kept in place by a Dirichlet boundary condition for velocity. Here, we use the fully elastic ($\tau = \infty$) Neo-Hookean model (35) with $\rho_0 = 1100 \text{ kg/m}^3$, $Y = 17 \text{ MPa}$ (Young modulus), $\nu = 0.495$ (Poisson ratio). These values are related to the bulk shear sound speed by relations:

$$\rho_0 c_s^2 = \frac{Y}{1 + \nu}, \quad \rho_0 c_0^2 = \frac{\nu Y}{(1 + \nu)(1 - 2\nu)}. \tag{61}$$

In this benchmark, inertia should twist the column, building up tensile forces that eventually prevail and reverse the rotation. The shape of the column should recover without loss of energy. Additionally, there is associated non-linear effect, which causes shrinkage of the column. All these phenomena are observed in our simulation, as can be seen in Figs. 5 and 7. We still have reasonably good energy conservation (Fig. 6), but the Dirichlet boundary condition at the base is slightly dissipative (since it is implemented by resetting the velocity to zero at every time step). Unfortunately, variables like pressure become very noisy in the simulation after a short time, but we did not find a remedy which would not involve artificial dissipation.

4.3. Laminar Taylor-Couette flow

We now turn our attention to the fluid regime of the SHTC equations, which means that $\tau < \infty$ and the relaxation terms need to be taken into account. First, we try a simple test of laminar flow in an annulus

$$\Omega = \{(x, y) : R_1^2 < x^2 + y^2 < R_2^2\} \tag{62}$$

driven by a rigid counterclockwise rotation of the outer ring with angular velocity ω . Meanwhile, the inner ring has zero angular velocity. We take $R_1 = 1$, $R_2 = 2$ and $\omega = 1$. The flow is incompressible and well described by the incompressible Navier-Stokes equations with kinetic viscosity $\nu = 0.1$. This corresponds to a low Reynolds number

$$\text{Re} = \frac{\omega R_2 (R_2 - R_1)}{\nu} = 20, \tag{63}$$

which ensures laminar flow. The exact stationary solution to this problem is given by the formula

$$\mathbf{v} = \frac{R_2}{r} \frac{r}{R_1} - \frac{R_1}{r} \frac{r}{R_2} \begin{pmatrix} -\omega y \\ \omega x \end{pmatrix}. \tag{64}$$

The solution theoretically does not depend on ν but viscosity affects how quickly the velocity field converges (if at all), starting from $\mathbf{v} = \mathbf{0}$.

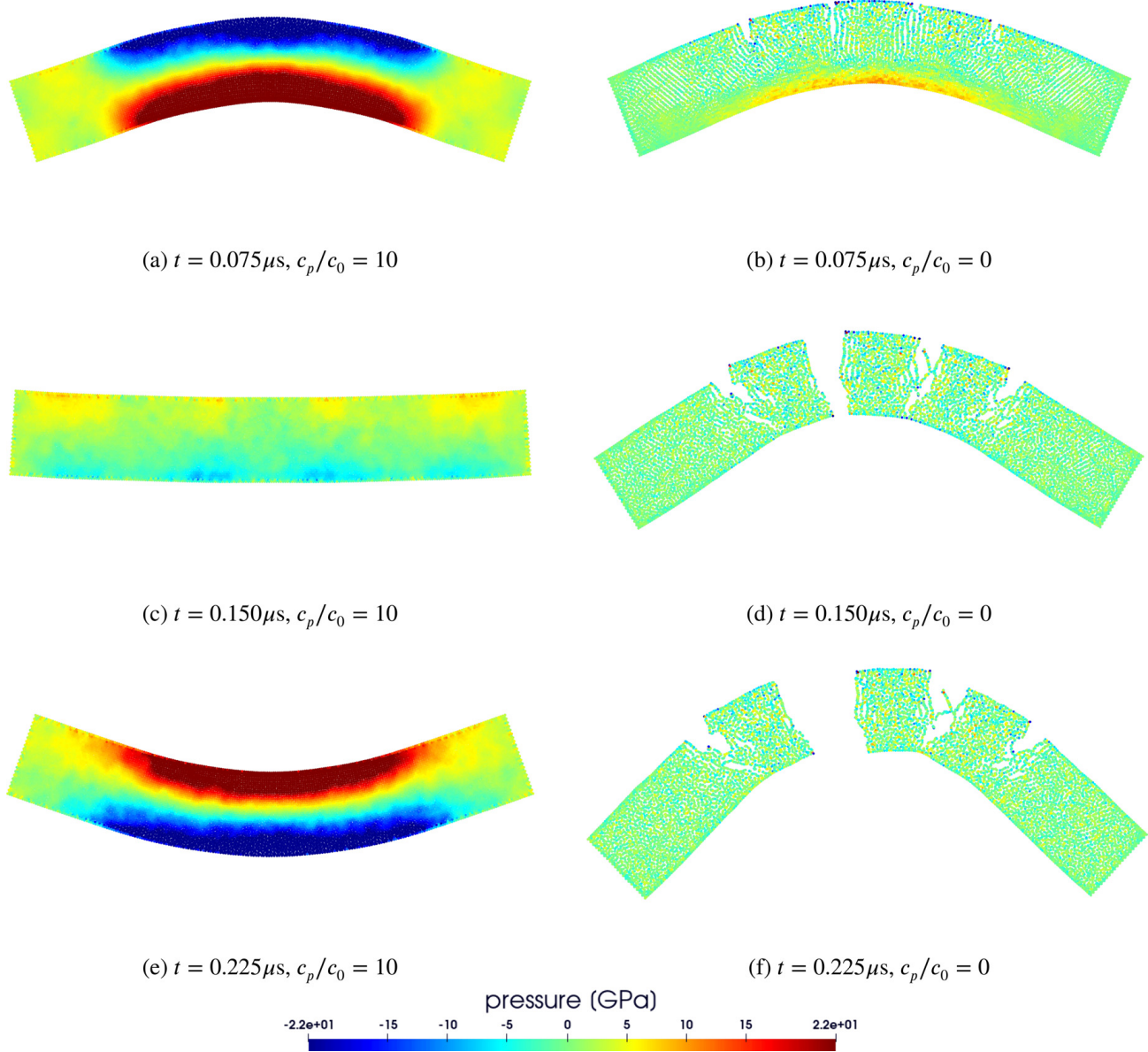


Fig. 4. Images of beryllium plate simulation and color-plot for pressure with tensile instability treatment (left) and without (right). For $c_p = 0$, particles have an extra degree of freedom which allows them to minimize negative pressure by forming clumps. This results in clearly non-physical behavior.

The Navier-Stokes equations (NSEs) are formally incompatible with the SHTC equations, which can be inferred from the fact that NSEs are a hyperbolic-parabolic system, whereas SHTC equations include only first-order hyperbolic equations. However, it is possible to obtain NSEs (at least formally) in the asymptotic expansion of the SHTC equations as the first-order terms in τ [2]. To achieve sufficiently small values of τ one needs to take sufficiently large values of the shear sound speed since they are related as [2]

$$\tau = \frac{6\nu}{c_s^2}. \tag{65}$$

Here, we essentially mirror the common approach in SPH, where incompressibility is enforced by “sufficiently high” values of c_0 (corresponding to small Mach number $\text{Ma} = \|\mathbf{v}\|/c_0 \ll 1$) but this time for the shear component of energy. The characteristic speed in this simulation is $\omega R_2 = 2$, so it is reasonable to take $c_0 = 20$ and $c_s = 40$. Here, we set $\delta r = \frac{1}{40}$ and δt according to (58). With these parameters, we get

$$\frac{\delta t}{\tau} \doteq 0.075 \tag{66}$$

so the natural time step is significantly smaller than τ , justifying the use of an explicit time integrator for relaxation. Note that using strictly incompressible scheme would probably yield better results in this benchmark. However, it would require

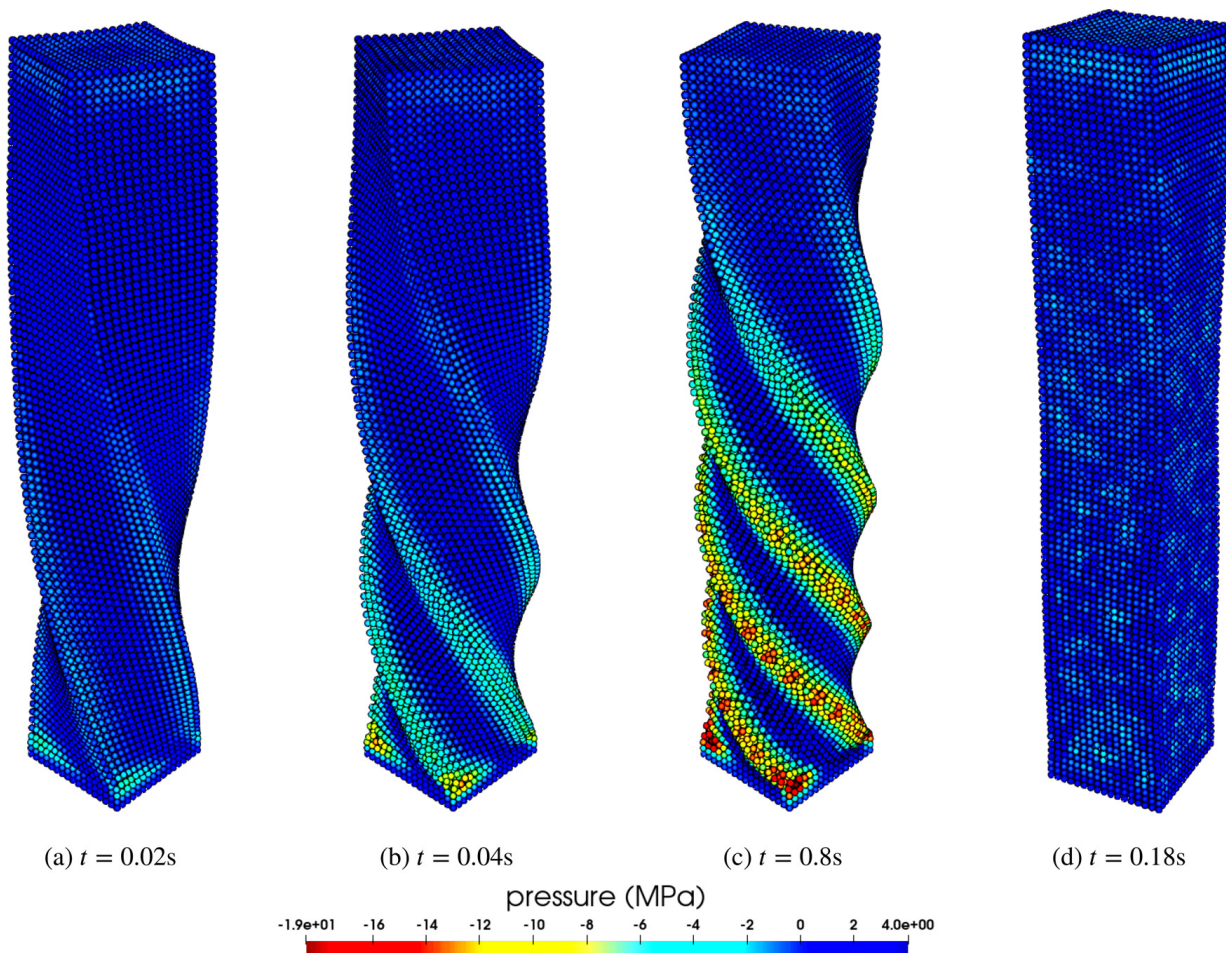


Fig. 5. Results of the twisting column simulation with a color-plot for pressure. We use this as a qualitative test whether our code can deal with large elastic deformations in three dimensions. The last frame shows the column after untwisting, showing some noise in the pressure field (presumably, this can be remedied by adding artificial dissipation). Shape of the column is not exactly recovered but note that the elastic energy is not perfectly zero at this point either (see Fig. 6).

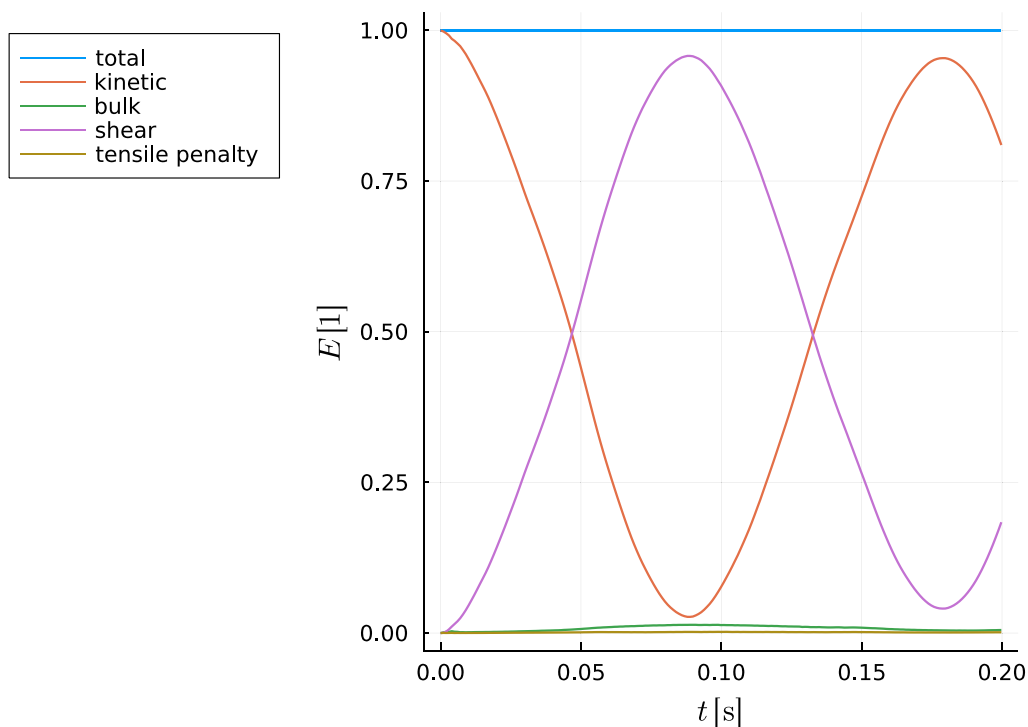


Fig. 6. Energy conservation in twisting column benchmark. The relative total energy error is within $4 \cdot 10^{-7}$.

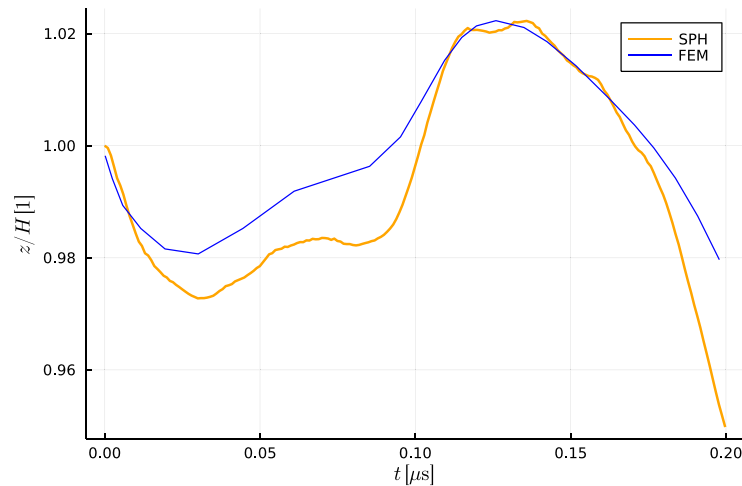


Fig. 7. Twisting column: the normalized z-coordinate of material point initially at $(0, 0, H)$ plotted against time. Although the column is shrinking at first, it “bounces off” at some point and starts to elongate. This effect was also observed in [17] and [57]. The blue line shows comparison to a finite element simulation (created using the Fenics software [58]).

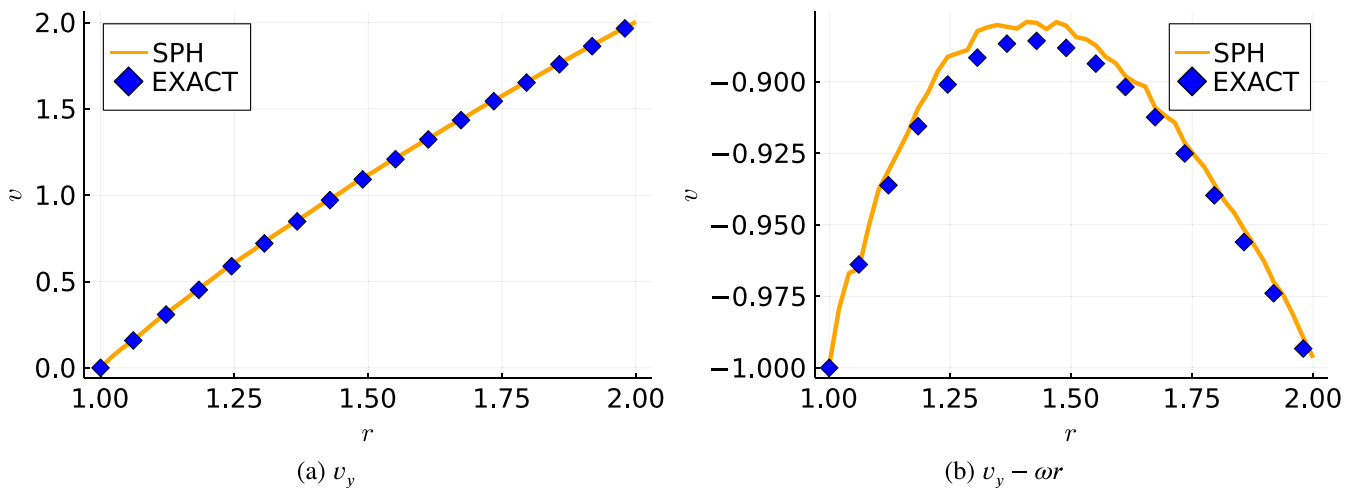


Fig. 8. Tangential velocity in the simulation at $t = 10$ along the segment $y = 0, R_1 \leq x \leq R_2$ (orange line) and its comparison to the exact solution (blue squares). Picture on the right magnifies error by subtracting a linear approximation $v_y \approx \omega r$ from both data arrays.

us to use implicit SPH, leading to complications such as boundary recognition [45]. Since this paper pioneers SPH-SHTC scheme, we want avoid these intricacies for now.

Despite the numerous approximations used, we obtain reasonable agreement with the exact solution, as shown in Fig. 8. It is interesting here to plot the distortion field (Fig. 9). Even for such a simple stationary flow, \mathbb{A} displays non-stationary behavior due to the rotation of the local basis vectors (see the color map in Fig. 9 which ranges from -1 to $+1$) represented by \mathbb{A} , e.g. see [1–3]. Fig. 10 shows convergence analysis. The convergence curve shows non-monotonic behavior and possibly a nonzero discretization error limit. This behavior is known in SPH, see [59].

4.4. Lid-driven cavity

The advantages of the Taylor-Couette benchmark are simple implementation and availability of an exact solution (in steady state at least). It is, however, insufficient in the sense that the velocity field does not depend on the magnitude of ν . For a more qualitative and challenging test, we include the lid-driven cavity benchmark. The geometry of this problem consists of a square $\Omega = (0, 1) \times (0, 1)$ filled with a viscous fluid. The left, right, and bottom boundaries are the walls with a no slip boundary condition, i.e. $\mathbf{v} = 0$, and the top boundary is moving at the prescribed velocity

$$\mathbf{v}_{\text{lid}} = \begin{pmatrix} 1 \\ 0 \end{pmatrix}. \tag{67}$$

For the shear energy, we use the constitutive Eq. (31) with $\rho = 1$. Again, in the case of fluid flows, and especially incompressible flows, the ideal values for the shear and bulk speed of sound would be $c_s \gg 1, c_0 \gg 1$ corresponding to the

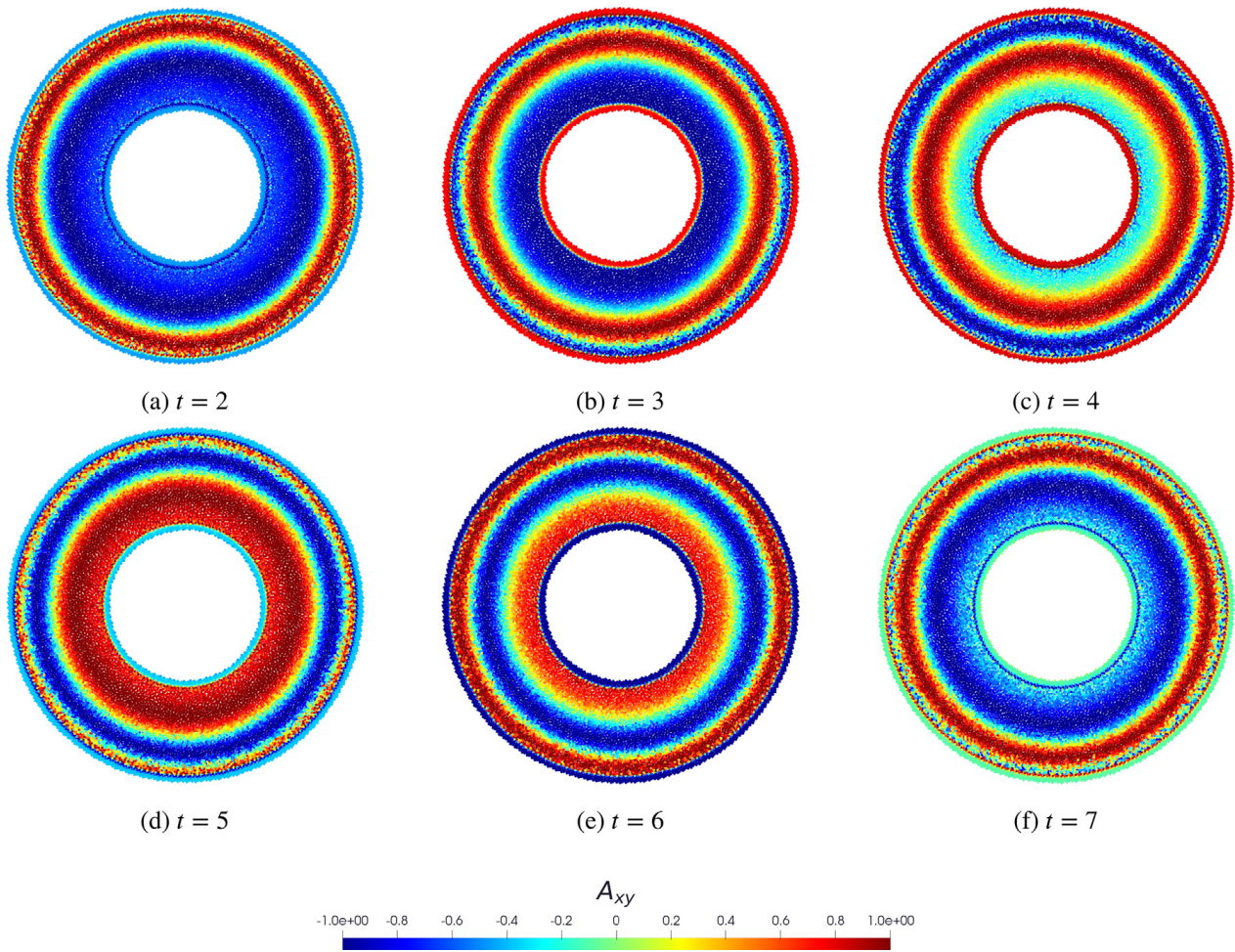


Fig. 9. Plot of xy distortion component. Interestingly, whereas velocity converges in time (approximately) to the stationary solution (64), the \mathbb{A} field is always changing in a periodic manner, forming waves that travel from the outer ring towards the center.

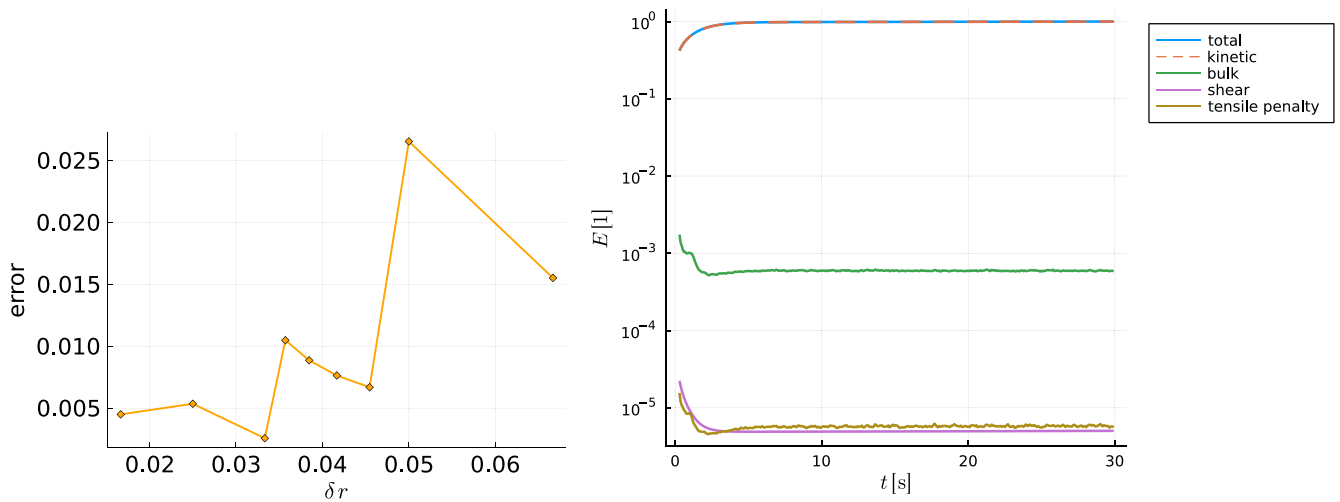
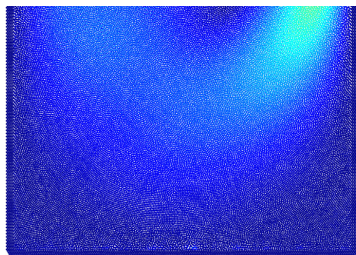


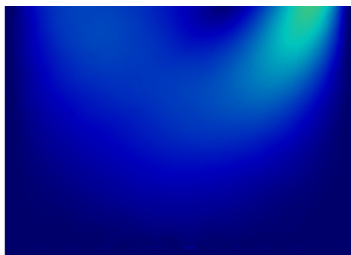
Fig. 10. Left: Changing δr in Taylor-Couette flow, we observe non-monotonic behavior of the convergence curve. The error is computed using L^∞ norm on the segment $x \in [1, 2], y = 0$. Right: Semi-logarithmic plot of energy components normalized by the final total energy E_f . Individual components differ by several orders of magnitude. The total energy overlaps with the kinetic energy. It increases since the flow is externally driven.

incompressible Navier-Stokes limit of the SHTC equations, i.e. $\tau \sim \nu/c_s^2 \ll 1$ and $Ma \sim \|\mathbf{v}\|/c_0 \ll 1$, but this is not possible in our scheme because the underlying ODE system (51) would become extremely stiff. Therefore, as an approximation, we set²

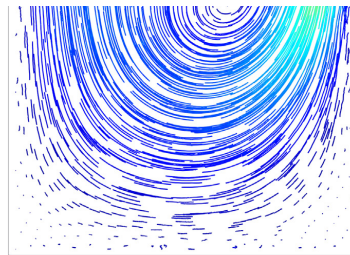
² We note that the shear sound speed c_s is not an artificial fitting parameter in the SHTC equations but it can be measured for real fluids via the sound dispersion data and fitted via a procedure described in [38].



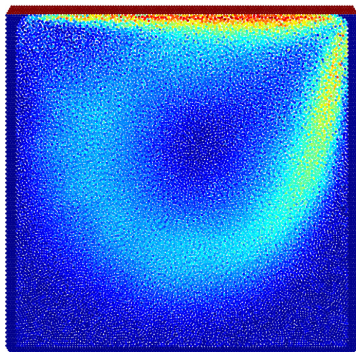
(a) particles, $Re = 100, t = 10$



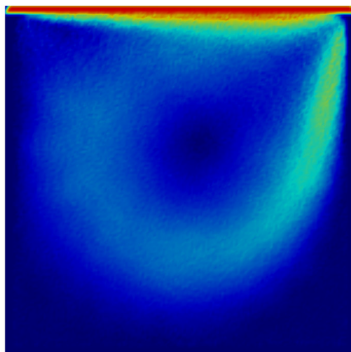
(b) interpolation, $Re = 100, t = 10$



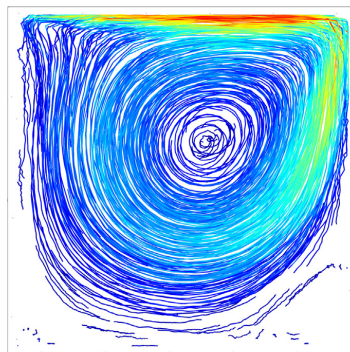
(c) path-lines, $Re = 100, t = 10$



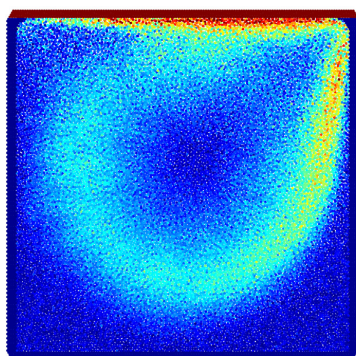
(d) particles, $Re = 400, t = 20$



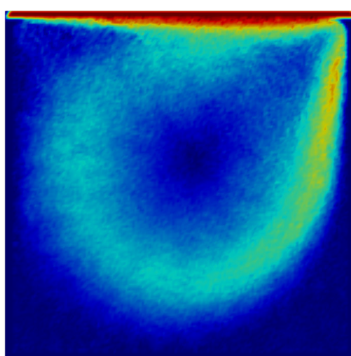
(e) interpolation, $Re = 400, t = 20$



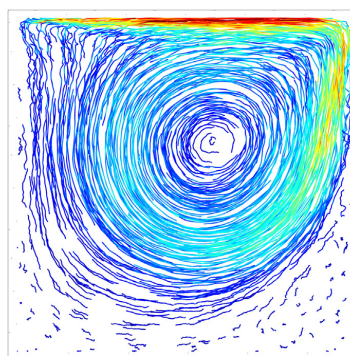
(f) path-lines, $Re = 400, t = 20$



(g) particles, $Re = 1000, t = 20$



(h) interpolation, $Re = 1000, t = 20$



(i) path-lines, $Re = 1000, t = 20$

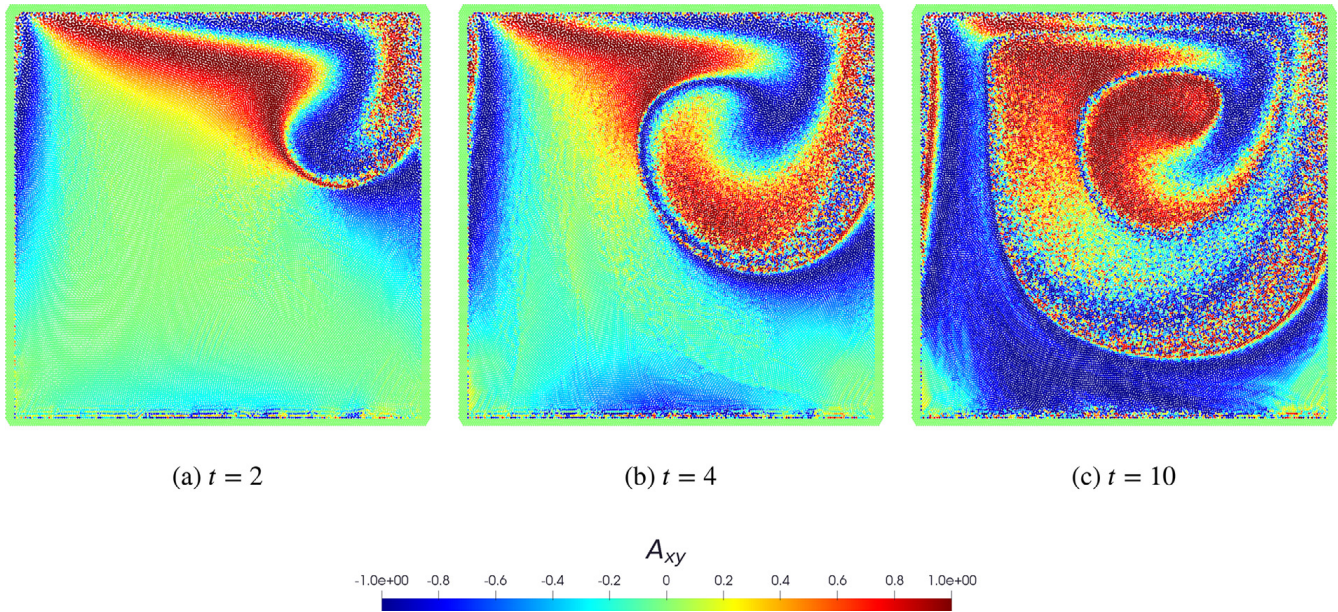


Fig. 12. Evolution of the distortion field in Newtonian lid-driven cavity benchmark for $Re = 100$.

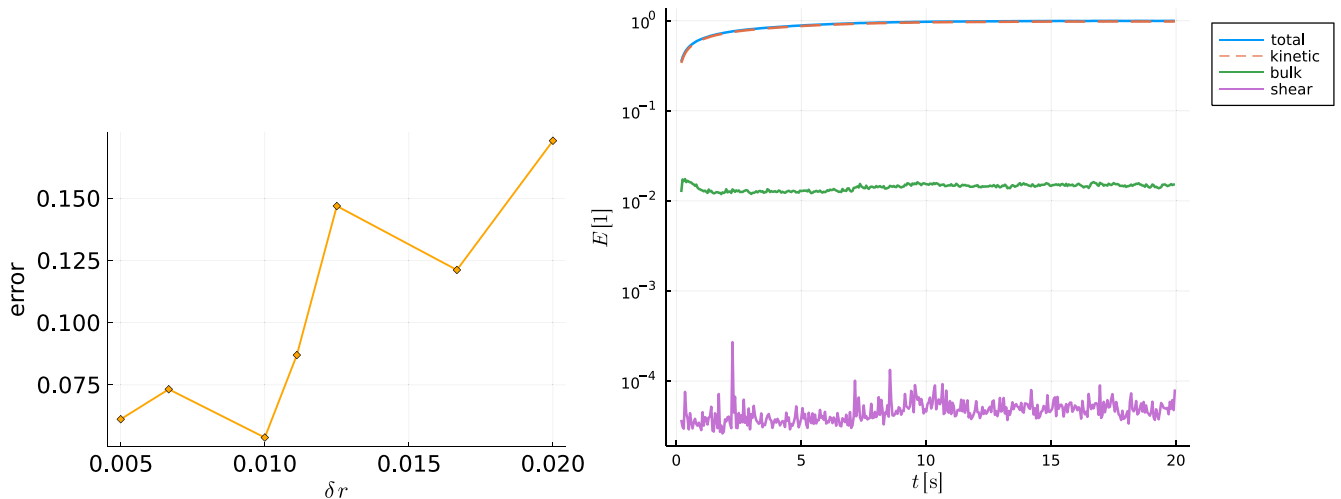


Fig. 13. Left: Convergence analysis in lid-driven cavity problem for $Re = 100$. The error is computed using L^∞ norm at the nodes where referential solution is provided. Right: Energy components (normalized by the final total energy).

$$c_s = c_0 = 20. \tag{68}$$

We consider the cases of $Re \in \{100, 400, 1000\}$. The viscosity and the relaxation time are related to this number by:

$$\nu = \frac{1}{Re}, \quad \tau = \frac{6\nu}{c_s^2}. \tag{69}$$

The no slip walls are implemented as h -deep layer of particles with zero velocity. The lid is implemented similarly with immobile particles but “pretending” to have velocity v_{lid} for the purposes of L computation (Eq. (10)). The initial state is somewhat problematic in a weakly compressible scheme because discontinuities in the velocity field will generate shock waves. For this reason, we fix the zero lid velocity at $t = 0$ and gradually accelerate it up to 1.

The results are shown in Figs. 11 and 12. In Fig. 14, we plot the transverse velocity along the center lines and compare the result to a referential solution [60]. Despite one can see slight discrepancies between SPH-SHTC solution and the reference one in Fig. 14 (which we suspect is caused by the problematic implementation of the Dirichlet boundary condition) a reasonable agreement between the solutions has been achieved. Fig. 13 shows the convergence analysis. One can observe a similar zigzag pattern as seen in the Talor-Coutte benchmark. Also, as was already reported in [3], as the Reynolds number goes higher and higher it gets increasingly difficult to compute the distortion field as its spin faster and faster. As a consequence, the computation of the viscous stress also getting increasingly difficult that results in spurious oscillations in the velocity field, see Fig. (14), which are more pronounced for high Reynolds numbers.

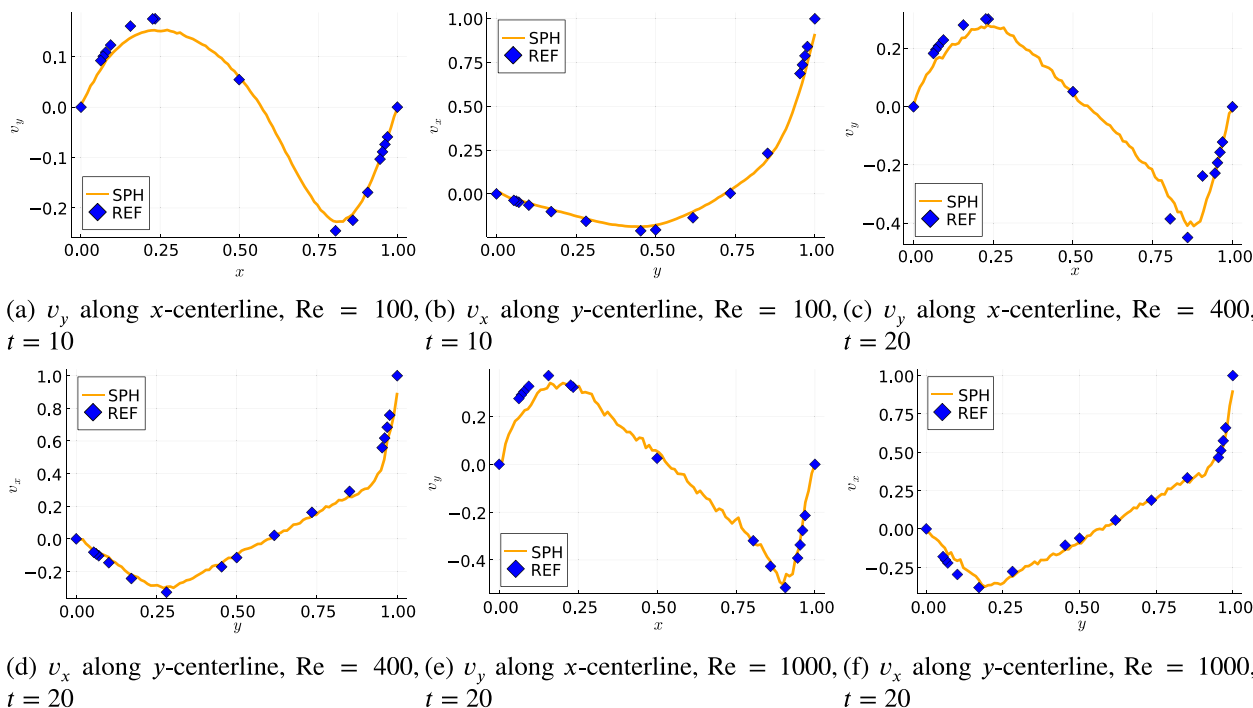


Fig. 14. Plot of transverse velocities along lines $x = \frac{1}{2}$ and $y = \frac{1}{2}$ in the Newtonian lid-driven cavity benchmark. Decent agreement with reference is achieved. With growing Reynolds numbers, however, distortion Δ has increasingly complicated dynamics, which makes it difficult to resolve viscous stress accurately. Therefore, we see some numerical oscillations in the curves for $Re = 1000$.

5. Conclusion

We have developed a new SHTC-SPH numerical method that is suitable for simulations of both fluids and solids within a single framework. To the best of our knowledge it is the first ever discretization of the SHTC equations with an SPH scheme. The method discretizes (both in space and time) the Symmetric Hyperbolic Thermodynamically Compatible Eq. (1), which describe both fluids and solids. First, we discretize them in space, which results in the SHTC-SPH ordinary differential Eq. (23), which contain an evolution equation for a discrete analogue of the distortion field. Then, we prescribe a time integrator (49), which gives the SHTC-SPH numerical scheme.

The scheme is then tested on benchmarks like a vibrating Beryllium plate, twisting column, laminar Taylor-Couette flow, and lid-driven cavity flow, and shows acceptable agreement with the data, although finite volume and discontinuous Galerkin ADER schemes [2,17] usually offer better precision.

Currently, due to its quasi-Hamiltonian property and lack of dissipation, the presented SHTC-SPH scheme can be applied only to smooth flows without discontinuities such as shocks, and future research will be directed towards consistent introduction of dissipation into the scheme, e.g. in the spirit of [19]. In the future, we would like to investigate deeper geometrical properties of the SHTC-SPH scheme, such as its Hamiltonianity and conservation of Casimirs [61] as well as incorporating the heat conduction part of the SHTC equations. In addition, we plan to combine SHTC with an implicit variant of SPH for improving stability and performance in low Mach number flows.

Acknowledgments

The authors are grateful to Markus Hütter for bringing our attention to the paper by Falk and Langer which helped us to construct the proposed discretization of the distortion field. OK was supported by project No. START/SCI/053 of Charles University Research program. MP was supported by project No. UNCE/SCI/023 of Charles University Research program. OK, MP and VK were also supported by the Czech Science Foundation (project no. 20-22092S). VK is grateful for the support from European Regional Development Fund-Project ‘Center for Advanced Applied Science’ (no. CZ.02.1.01/0.0/0.0/16_019/0000778). IP is a member of the Gruppo Nazionale per il Calcolo Scientifico of the Istituto Nazionale di Alta Matematica (INdAM GNCS) and acknowledges the financial support received from the Italian Ministry of Education, University and Research (MIUR) in the frame of the Departments of Excellence Initiative 2018-2022 attributed to the Department of Civil, Environmental and Mechanical Engineering (DICAM) of the University of Trento (Grant No. L.232/2016) and in the frame of the Progetti di Rilevante Interesse Nazionale (PRIN) 2017, Project No. 2017KKJP4X, ‘Innovative numerical methods for evolutionary partial differential equations and applications’.




References

- [1] I. Peshkov, E. Romenski, A hyperbolic model for viscous Newtonian flows, *Contin. Mech. Thermodyn.* 28 (1-2) (2016) 85–104, doi:[10.1007/s00161-014-0401-6](https://doi.org/10.1007/s00161-014-0401-6).
- [2] M. Dumbser, I. Peshkov, E. Romenski, O. Zanotti, High order ADER schemes for a unified first order hyperbolic formulation of continuum mechanics: viscous heat-conducting fluids and elastic solids, *J. Comput. Phys.* 314 (2016) 824–862, doi:[10.1016/j.jcp.2016.02.015](https://doi.org/10.1016/j.jcp.2016.02.015).
- [3] I. Peshkov, M. Dumbser, W. Boscheri, E. Romenski, S. Chiochetti, M. Ioriatti, Simulation of non-Newtonian viscoplastic flows with a unified first order hyperbolic model and a structure-preserving semi-implicit scheme, *Comput. Fluids* 224 (2021) 104963, doi:[10.1016/j.compfluid.2021.104963](https://doi.org/10.1016/j.compfluid.2021.104963).
- [4] I. Peshkov, W. Boscheri, R. Loubère, E. Romenski, M. Dumbser, Theoretical and numerical comparison of hyperelastic and hypoelastic formulations for Eulerian non-linear elastoplasticity, *J. Comput. Phys.* 387 (2019) 481–521, doi:[10.1016/j.jcp.2019.02.039](https://doi.org/10.1016/j.jcp.2019.02.039).
- [5] I. Peshkov, M. Pavelka, E. Romenski, M. Grmela, Continuum mechanics and thermodynamics in the Hamilton and the Godunov-type formulations, *Contin. Mech. Thermodyn.* 30 (6) (2018) 1343–1378, doi:[10.1007/s00161-018-0621-2](https://doi.org/10.1007/s00161-018-0621-2).
- [6] E.I. Romenski, Hyperbolic systems of thermodynamically compatible conservation laws in continuum mechanics, *Math. Comput. Model.* 28 (10) (1998) 115–130, doi:[10.1016/S0895-7177\(98\)00159-9](https://doi.org/10.1016/S0895-7177(98)00159-9).
- [7] S.K. Godunov, E.I. Romenskii, *Elements of Continuum Mechanics and Conservation Laws*, Kluwer Academic/Plenum Publishers, 2003.
- [8] S. Godunov, E. Romenski, Thermodynamics, conservation laws and symmetric forms of differential equations in mechanics of continuous media, in: *Computational Fluid Dynamics Review 1995*, volume 95, John Wiley, NY, 1995, pp. 19–31, doi:[10.1142/7799](https://doi.org/10.1142/7799).
- [9] S.K. Godunov, An interesting class of quasilinear systems, *Dokl. Akad. Nauk SSSR* 139(3) (1961) 521–523.
- [10] M. Grmela, H.C. Öttinger, Dynamics and thermodynamics of complex fluids. I. Development of a general formalism, *Phys. Rev. E* 56 (1997) 6620–6632, doi:[10.1103/PhysRevE.56.6620](https://doi.org/10.1103/PhysRevE.56.6620).
- [11] H.C. Öttinger, M. Grmela, Dynamics and thermodynamics of complex fluids. II. Illustrations of a general formalism, *Phys. Rev. E* 56 (1997) 6633–6655, doi:[10.1103/PhysRevE.56.6633](https://doi.org/10.1103/PhysRevE.56.6633).
- [12] M. Pavelka, V. Klika, M. Grmela, *Multiscale Thermo-Dynamics*, de Gruyter, Berlin, 2018.
- [13] M. Ellero, P. Español, E.G. Flekkoy, Thermodynamically consistent fluid particle model for viscoelastic flows, *Phys. Rev. E* 68 (041504) (2003).
- [14] M. Ellero, P. Español, Everything you always wanted to know about sdpd "(but were afraid to ask)", *Appl. Math. Mech.* 39 (1) (2018) 103–124.
- [15] A. Vázquez-Quesada, M. Ellero, P. Español, Smoothed particle hydrodynamic model for viscoelastic fluids with thermal fluctuations, *Phys. Rev. E* 79 (5) (2009) 056707, doi:[10.1103/PhysRevE.79.056707](https://doi.org/10.1103/PhysRevE.79.056707).
- [16] S. Busto, S. Chiochetti, M. Dumbser, E. Gaburro, I. Peshkov, High order ADER schemes for continuum mechanics, *Front. Phys.* 8 (32) (2020), doi:[10.3389/fphy.2020.00032](https://doi.org/10.3389/fphy.2020.00032).
- [17] W. Boscheri, S. Chiochetti, I. Peshkov, A cell-centered implicit-explicit Lagrangian scheme for a unified model of nonlinear continuum mechanics on unstructured meshes, *J. Comput. Phys.* 451 (2022) 110852, doi:[10.1016/j.jcp.2021.110852](https://doi.org/10.1016/j.jcp.2021.110852).
- [18] W. Boscheri, M. Dumbser, M. Ioriatti, I. Peshkov, E. Romenski, A structure-preserving staggered semi-implicit finite volume scheme for continuum mechanics, *J. Comput. Phys.* 424 (2021) 109866, doi:[10.1016/j.jcp.2020.109866](https://doi.org/10.1016/j.jcp.2020.109866).
- [19] S. Busto, M. Dumbser, I. Peshkov, E. Romenski, On thermodynamically compatible finite volume schemes for continuum mechanics, *SIAM J. Sci. Comput.* 44 (3) (2022) A1723–A1751, doi:[10.1137/21M1417508](https://doi.org/10.1137/21M1417508).
- [20] R. Gingold, J. Monaghan, Smoothed particle hydrodynamics: theory and application to non-spherical stars, *Mon. Not. R. Astron. Soc.* 181 (3) (1977) 375–389.
- [21] C. Antoci, M. Gallati, S. Sibilla, Numerical simulation of fluid–structure interaction by sph, *Comput. Struct.* 85 (11-14) (2007) 879–890.
- [22] A. Rafiee, K.P. Thiagarajan, An SPH projection method for simulating fluid-hypoelastic structure interaction, *Comput. Methods Appl. Mech. Eng.* 198 (33-36) (2009) 2785–2795.
- [23] H.H. Bui, G.D. Nguyen, A coupled fluid-solid SPH approach to modelling flow through deformable porous media, *Int. J. Solids Struct.* 125 (2017) 244–264.
- [24] A. Ghaïtanellis, D. Violeau, M. Ferrand, K.E.K. Abderrezzak, A. Leroy, A. Joly, A SPH elastic-viscoplastic model for granular flows and bed-load transport, *Adv. Water Resour.* 111 (2018) 156–173.
- [25] J. Monaghan, A. Kocharyan, SPH simulation of multi-phase flow, *Comput. Phys. Commun.* 87 (1-2) (1995) 225–235.
- [26] T. Belytschko, Y. Guo, W. Kam Liu, S. Ping Xiao, A unified stability analysis of meshless particle methods, *Int. J. Numer. Methods Eng.* 48 (9) (2000) 1359–1400, doi:[10.1002/1097-0207\(20000730\)48:9<1359::AID-NME829>3.0.CO;2-U](https://doi.org/10.1002/1097-0207(20000730)48:9<1359::AID-NME829>3.0.CO;2-U).
- [27] J.P. Gray, J.J. Monaghan, R. Swift, SPH elastic dynamics, *Comput. Methods Appl. Mech. Eng.* 190 (49-50) (2001) 6641–6662.
- [28] T. Rabczuk, T. Belytschko, Cracking particles: a simplified meshfree method for arbitrary evolving cracks, *Int. J. Numer. Methods Eng.* 61 (13) (2004) 2316–2343, doi:[10.1002/nme.1151](https://doi.org/10.1002/nme.1151).
- [29] T. Rabczuk, T. Belytschko, A three-dimensional large deformation meshfree method for arbitrary evolving cracks, *Comput. Methods Appl. Mech. Eng.* 196 (29) (2007) 2777–2799, doi:[10.1016/j.cma.2006.06.020](https://doi.org/10.1016/j.cma.2006.06.020).
- [30] M. Liu, G. Liu, Smoothed particle hydrodynamics (SPH): an overview and recent developments, *Arch. Comput. Methods Eng.* 17 (1) (2010) 25–76.
- [31] J.J. Monaghan, Smoothed particle hydrodynamics and its diverse applications, *Annu. Rev. Fluid Mech.* 44 (2012) 323–346.
- [32] C.H. Lee, A.J. Gil, G. Greto, S. Kulasegaram, J. Bonet, A new Jameson Schmidt Turkel Smooth Particle Hydrodynamics algorithm for large strain explicit fast dynamics, *Comput. Methods Appl. Mech. Eng.* 311 (2016) 71–111, doi:[10.1016/j.cma.2016.07.033](https://doi.org/10.1016/j.cma.2016.07.033).
- [33] J. Monaghan, Smoothed particle hydrodynamics, *Rep. Prog. Phys.* 68 (2005) 1703, doi:[10.1088/0034-4885/68/8/R01](https://doi.org/10.1088/0034-4885/68/8/R01).
- [34] B. Andreotti, Y. Forterre, O. Pouliquen, *Granular Media: Between Fluid and Solid*, Cambridge University Press, 2013.
- [35] S. Dunatunga, K. Kamrin, Continuum modelling and simulation of granular flows through their many phases, *J. Fluid Mech.* 779 (2015) 483–513, doi:[10.1017/jfm.2015.383](https://doi.org/10.1017/jfm.2015.383).
- [36] W. Chen, T. Qiu, Numerical simulations for large deformation of granular materials using smoothed particle hydrodynamics method, *Int. J. Geomech.* 12 (2) (2012) 127–135, doi:[10.1061/\(ASCE\)GM.1943-5622.0000149](https://doi.org/10.1061/(ASCE)GM.1943-5622.0000149).
- [37] R. Feng, G. Fourtakos, B.D. Rogers, D. Lombardi, Large deformation analysis of granular materials with stabilized and noise-free stress treatment in smoothed particle hydrodynamics (SPH), *Comput. Geotech.* 138 (2021) 104356, doi:[10.1016/j.compgeo.2021.104356](https://doi.org/10.1016/j.compgeo.2021.104356).
- [38] M. Dumbser, I. Peshkov, E. Romenski, A unified hyperbolic formulation for viscous fluids and elastoplastic solids, in: C. Klingenberg, M. Westdickenberg (Eds.), *Springer Proceedings in Mathematics and Statistics*, Springer Proceedings in Mathematics and Statistics, 237, Springer International Publishing, Cham, 2018, pp. 451–463, doi:[10.1007/978-3-319-91548-7_34](https://doi.org/10.1007/978-3-319-91548-7_34), https://doi.org/10.1007/978-3-319-91548-7_34.
- [39] J. Frenkel, *Kinetic Theory of Liquids*, Dover, New York, NY, 1955.
- [40] V.V. Brazhkin, Y.D. Fomin, A.G. Lyapin, V.N. Ryzhov, K. Trachenko, Two liquid states of matter: a dynamic line on a phase diagram, *Phys. Rev. E* 85 (3) (2012) 031203, doi:[10.1103/PhysRevE.85.031203](https://doi.org/10.1103/PhysRevE.85.031203).
- [41] M. Pavelka, I. Peshkov, V. Klika, On Hamiltonian continuum mechanics, *Phys. D Nonlinear Phenom.* 408 (132510) (2020).
- [42] I. Peshkov, E. Romenski, A hyperbolic model for viscous newtonian flows, *Contin. Mech. Thermodyn.* 28 (2016) 85–104.
- [43] I. Peshkov, M. Pavelka, E. Romenski, M. Grmela, Continuum mechanics and thermodynamics in the Hamilton and the Godunov-type formulations, *Contin. Mech. Thermodyn.* 30 (6) (2018) 1343–1378.
- [44] B.A. Dubrovin, S.P. Novikov, Hamiltonian formalism of one-dimensional systems of hydrodynamic type, and the Bogolyubov-Whitham averaging method, *Dokl. Akad. Nauk SSSR* 270 (1983) 781–785. English transl. in *Soviet Math. Dokl.* 27 (1983)
- [45] D. Violeau, *Fluid Mechanics and the SPH Method: Theory and Applications*, Oxford University Press, Oxford, UK, 2012.
- [46] O. Kincl, M. Pavelka, Globally time-reversible fluid simulations with smoothed particle hydrodynamics, 2022 (<http://arxiv.org/abs/2204.08884>).

- [47] J. Bonet, T.-S. Lok, Variational and momentum preservation aspects of smooth particle hydrodynamic formulations, *Comput. Methods Appl. Mech. Eng.* 180 (1-2) (1999) 97–115.
- [48] J. Vila, On particle weighted methods and smooth particle hydrodynamics, *Math. Models Methods Appl. Sci.* 9 (02) (1999) 161–209.
- [49] M.L. Falk, J.S. Lange, Dynamics of viscoplastic deformation in amorphous solids, *Phys. Rev. E* 57 (6) (1998).
- [50] S.K. Godunov, I.M. Peshkov, Thermodynamically consistent nonlinear model of elastoplastic Maxwell medium, *Comput. Math. Math. Phys.* 50 (8) (2010) 1409–1426, doi:10.1134/S0965542510080117.
- [51] S. Ndanou, N. Favrie, S. Gavrilyuk, Criterion of hyperbolicity in hyperelasticity in the case of the stored energy in separable form, *J. Elast.* 115 (1) (2014) 1–25, doi:10.1007/s10659-013-9440-7.
- [52] J.J. Monaghan, SPH without a tensile instability, *J. Comput. Phys.* 159 (2) (2000) 290–311.
- [53] S. Lind, R. Xu, P. Stansby, B. Rogers, Incompressible smoothed particle hydrodynamics for free-surface flows: a generalised diffusion-based algorithm for stability and validations for impulsive flows and propagating waves, *J. Comput. Phys.* 231 (4) (2012) 1499–1523, doi:10.1016/j.jcp.2011.10.027.
- [54] P. Sun, A. Colagrossi, S. Marrone, M. Antuono, A.-M. Zhang, A consistent approach to particle shifting in the δ -plus-SPH model, *Comput. Methods Appl. Mech. Eng.* 348 (2019) 912–934.
- [55] E. Hairer, C. Lubich, G. Wanner, *Geometric Numerical Integration: Structure-Preserving Algorithms for Ordinary Differential Equations*, Springer Series in Computational Mathematics, Springer Berlin Heidelberg, 2013.
- [56] L. Landau, E. Lifshitz, *Mechanics*, Butterworth-Heinemann, 1976. Butterworth Heinemann
- [57] J. Haider, C.H. Lee, A.J. Gil, A. Huerta, J. Bonet, An upwind cell centred total lagrangian finite volume algorithm for nearly incompressible explicit fast solid dynamic applications, *Comput. Methods Appl. Mech. Eng.* 340 (2018) 684–727.
- [58] A. Logg, K.-A. Mardal, G.N. Wells, et al., *Automated Solution of Differential Equations by the Finite Element Method*, Springer, 2012, doi:10.1007/978-3-642-23099-8.
- [59] N.J. Quinlan, M. Basa, M. Lastiwka, Truncation error in mesh-free particle methods, *Int. J. Numer. Methods Eng.* 66 (13) (2006) 2064–2085.
- [60] U. Ghia, K.N. Ghia, C. Shin, High-re solutions for incompressible flow using the Navier-Stokes equations and a multigrid method, *J. Comput. Phys.* 48 (3) (1982) 387–411.
- [61] P. Pelech, K. Tůma, M. Pavelka, M.S. Martin Šípka, On compatibility of the natural configuration framework with GENERIC: Derivation of anisotropic rate-type models, 2020, model.

RESEARCH ARTICLE | APRIL 25 2023

Simulation of superfluid fountain effect using smoothed particle hydrodynamics

Ondřej Kincl ; David Schmoranzner ; Michal Pavelka 



Physics of Fluids 35, 047124 (2023)

<https://doi.org/10.1063/5.0145864>



View
Online



Export
Citation

CrossMark

Articles You May Be Interested In

Impinging axisymmetric turbulent fountains

Physics of Fluids (November 2007)

Fluttering fountains: Annular geometry

Journal of Applied Physics (February 1996)

Physics of the granite sphere fountain

Am. J. Phys. (November 2014)

Simulation of superfluid fountain effect using smoothed particle hydrodynamics

Cite as: Phys. Fluids **35**, 047124 (2023); doi: [10.1063/5.0145864](https://doi.org/10.1063/5.0145864)

Submitted: 8 February 2023 · Accepted: 28 March 2023 ·

Published Online: 25 April 2023



View Online



Export Citation



CrossMark

Ondřej Kincl,^{1,a)}  David Schmoranzer,²  and Michal Pavelka¹ 

AFFILIATIONS

¹Mathematical Institute, Faculty of Mathematics and Physics, Charles University, Sokolovská 83, 18675 Prague, Czech Republic

²Department of Low-Temperature Physics, Faculty of Mathematics and Physics, Charles University, V Holešovičkách 2, 180 00 Prague, Czech Republic

^{a)}Author to whom correspondence should be addressed: kincl@karlin.mff.cuni.cz

ABSTRACT

This paper investigates the applicability of smoothed particle hydrodynamics in simulations of superfluid helium-4. We devise a new approach based on Hamiltonian mechanics suitable for simulating thermally driven and weakly compressible flows with free surfaces. The method is then tested in three cases, including a simulation of the fountain effect. We obtain remarkable agreement with referential and theoretical results. The simulations provide new physical insight, such as the pressure and temperature fields in a vessel experiencing the fountain effect.

© 2023 Author(s). All article content, except where otherwise noted, is licensed under a Creative Commons Attribution (CC BY) license (<http://creativecommons.org/licenses/by/4.0/>). <https://doi.org/10.1063/5.0145864>

I. INTRODUCTION

Quantum fluids are governed by laws of quantum mechanics rather than classical ones and represent a fairly recent addition to the family of various types of fluids with relevance both in fundamental science and in technological applications. Prime examples can be found in superfluid phases of helium isotopes or in Bose–Einstein condensates of rarefied gases. These fluids possess remarkable properties, such as the possibility of frictionless flow, the existence of numerous sound modes, the formation of superfluid films, quantized circulation around discrete vortex lines, or the ability to transport heat convectively with zero local mass flow. In addition to the fields of low-temperature physics and fluid dynamics, this behavior makes quantum fluids appealing, via certain analogies,⁶² for researchers across multiple disciplines, including astrophysicists^{13,44} or cosmologists,^{22,65} for which they represent an accessible model system.

In this work, we deal specifically with the isotope helium-4. The liquid phase, historically called He I, exists below 4.2 K at standard pressure. When cooled further by pumping on its vapors, helium-4 undergoes a second-order phase transition at 2.17 K and enters the superfluid phase, called He II. Most physical properties of helium are well-known and tabulated.⁶

He II exhibits all of the exotic phenomena mentioned above; for instance, it flows easily through narrow capillaries without friction and displays two-fluid behavior (in the sense of Landau's model, see

further below). The latter leads to the mechano-caloric effect, or the famous fountain effect,¹ where a heater causes the motion of helium in the form of a fountain-like jet.² Additionally, various forms of turbulent motion may exist in He II, including a state of two-fluid “double turbulence;” for a phenomenological treatment of quantum turbulence, see Ref. 47.

Historically, experimental investigations of dynamics in He II may be divided into studies of thermally generated flows, such as the fountain effect, counterflow in a channel driven by a heater placed at its closed end,³² or mechanically driven flows, mostly by submerged oscillating structures.^{14,20,43} A superfluid wind tunnel experiment has been constructed,⁴¹ and a large-scale Kármán flow experiment is now in operation.⁴⁰ Methods for flow visualization using tracer particles^{25,26} or He excimers⁴² have been developed recently and applied to both thermally and mechanically driven flows.

The motion of superfluid helium-4 can be simulated by solving the Gross–Pitaevskii equation,⁴⁶ the Hall–Vinen–Bekarevich–Khalatnikov (HVBK) models,^{5,15} the one-component models,³⁵ or by the vortex-filament method.^{10,19} However, many experiments are notoriously difficult to simulate numerically using mesh-based techniques such as finite element or finite volume methods, as they contain either a free surface (fountain effect) or a moving boundary (oscillating bodies). Therefore, it is advantageous to use a method based on Smoothed Particle Hydrodynamics (SPH),^{31,33,58} which is mesh-free and thus more suitable for these problems.

This paper presents a new numerical mesh-free method for simulations of superfluid helium-4. An SPH method for helium II has already been developed by Tsuzuki,^{54–56} who investigated vortices emerging in a rotating cylinder. Our approach is different because we discretize helium II using only one type of fluid particle with two densities as opposed to the work of Tsuzuki, where normal and super particles are distinguished. Our method comes at the cost of including additional convective terms, which consider that entropy, for instance, is advected by normal velocity and not by the collective or coflow velocity. However, it liberates us from assuming that superfluid behaves like a mixture and facilitates the implementation of heating bodies (a crucial feature in thermally driven flows, like the fountain effect). Additionally, we use a slightly different form of equations, a Hamiltonian variant of the two-fluid model that goes beyond the Landau–Tisza approach. We explain this in detail in [Appendix A](#). The Hamiltonian characteristic of the equations is advantageous also in the SPH numerical scheme.²³

The first macroscopic models of superfluid helium-4 were proposed by Tisza *et al.*^{16,27,49,51} Their final model²¹ consists of four evolution equations, namely, the continuity equation, balance of momentum, evolution of superfluid velocity, and entropy balance. The Landau–Tisza model can also be derived from the Gross–Pitaevskii equation.⁵³ However, the model has several limitations. First, it does not allow for non-zero superfluid vorticity (quantum vortices).

Second, the Landau–Tisza model is formulated in terms of five quantities (superfluid density ρ_s , normal density ρ_n , superfluid velocity v_s , normal velocity v_n , and entropy density s), despite having only four evolution equations. This inconsistency is overcome by setting a dependence of the ratio ρ_n/ρ on temperature ($\rho = \rho_s + \rho_n$ being the total mass density). Although this setting closes the evolution equations, it goes against the nature of superfluid helium-4, which is not a mixture of two fluids, but rather a single fluid with two motions, as expressed by Landau.^{27,29} “It must be particularly stressed that we have here no real division of the particles of the liquid into ‘superfluid’ and ‘normal’ ones....” The dependence $\rho_n/\rho(T)$ actually defines how free energy depends on temperature, which has to be taken into account because otherwise compatibility with Hamiltonian mechanics would be violated.⁵⁰ The HVBK model resolves the problem of four equations for five quantities by requiring both v_n and v_s to be divergence-free (incompressible).^{4,38} Another solution was proposed by Zilsel,⁶⁴ who introduced a continuity equation for both ρ_s and ρ_n , despite that there are no real two components in the superfluid helium (as noted by Landau). Yet another solution is the so-called one-fluid model,³⁵ where entropy exhibits an extra motion instead of density.

Here, we follow a route that builds upon Hamiltonian structures of the evolution equations for superfluid helium-4. The Hamiltonian structure of Landau–Tisza equations was derived from quantum commutators between the mass density and phase of the wave function.^{7,27} Moreover, Volovik and Dotsenko extended the Hamiltonian structure to a model related to HVBK dynamics by also considering Hamiltonian motion of quantum vortices.^{59–61} Alternatively, the Hamiltonian form of equations can be derived from the one-fluid model.⁵⁰ This is the structure we use in the current manuscript. Another Hamiltonian formulation of HVBK dynamics was obtained by Holm and Kuperschmidt,^{11,17,18} which contains additional state variables (vector and scalar potentials of the superfluid velocity).

This manuscript is organized as follows. Section II contains both the continuous model of superfluid helium-4 and the discrete SPH counterpart. Section III describes numerical simulation of the fountain effect and its comparison with experimental data.

II. SPH TWO-FLUID MODEL

This section contains a two-fluid model of superfluid helium-4 that extends the Landau–Tisza model and its discretization within SPH.

A. Reversible part of the model

The reversible part of our model consists of the following four evolution equations:

$$\begin{aligned} \frac{D\rho}{Dt} &= -\rho\nabla\cdot\mathbf{v}, \\ \frac{Ds}{Dt} &= -\frac{1}{\rho}\nabla\cdot(\rho s\chi_s\mathbf{v}_{ns}), \\ \frac{D\mathbf{v}}{Dt} &= -\frac{1}{\rho}\nabla\cdot(\rho\chi_n\chi_s\mathbf{v}_{ns}\otimes\mathbf{v}_{ns}+p\mathbf{I}), \\ \frac{D\mathbf{v}_s}{Dt} &= \chi_n\nabla\mathbf{v}_n^T\mathbf{v}_{ns}-\frac{\nabla p}{\rho}+s\nabla T, \end{aligned} \tag{1}$$

where “unknowns” ρ, s, \mathbf{v} , and \mathbf{v}_s are the density, specific entropy, coflow velocity, and superflow velocity, respectively. We denote the temperature as T and pressure as p . Dimensionless variables $\chi_n, \chi_s \in (0, 1)$ are mass fractions of normal and super components and satisfy $\chi_n + \chi_s = 1$. The coflow velocity and the counterflow velocity \mathbf{v}_{ns} satisfy the following relations:

$$\begin{aligned} \mathbf{v} &= \chi_n\mathbf{v}_n + \chi_s\mathbf{v}_s, \\ \mathbf{v}_{ns} &= \mathbf{v}_n - \mathbf{v}_s. \end{aligned} \tag{2}$$

We consider T, χ_n, χ_s , and p to be smooth functions of the unknowns. Equations (1) contain convective derivatives with respect to the overall coflow velocity

$$\frac{D\varphi}{Dt} := \frac{\partial\varphi}{\partial t} + \mathbf{v}\cdot\nabla\varphi = \frac{1}{\rho}\left(\frac{\partial(\rho\varphi)}{\partial t} + \nabla\cdot(\rho\varphi\mathbf{v})\right), \quad \forall\varphi. \tag{4}$$

This is the difference with respect to the standard Landau–Tisza model,^{49,53} where the superfluid velocity is convected only by itself (\mathbf{v}_s) and not by the whole coflow velocity. Equations (1) should, however, be superior to the Landau–Tisza model as they contain terms that at least partly take into account effects of quantum vorticity, see [Appendix A](#).

B. Irreversible forces

Equations (1) represent only the reversible part of superfluid dynamics. It can be beneficial to add some irreversibility to the system for increased realism, enhanced numerical stability, and noise suppression. We will consider two types of dissipative processes: viscosity of normal flow and parabolic thermal conduction. In future, the latter could be replaced with a complete model of quantum turbulence, which includes mutual friction. We include related entropy production terms to conserve the total energy. Thus, we write

$$\begin{aligned} \frac{D\rho}{Dt} &= -\rho\nabla\cdot\mathbf{v}, \\ \frac{Ds}{Dt} &= -\frac{1}{\rho}\nabla\cdot(\rho s\chi_s\mathbf{v}_{ns}) + \frac{\beta}{\rho}\Delta T + \frac{\zeta}{\rho T}, \\ \frac{D\mathbf{v}}{Dt} &= -\frac{1}{\rho}\nabla\cdot(\rho\chi_n\chi_s\mathbf{v}_{ns}\otimes\mathbf{v}_{ns} + p\mathbf{I}) + \frac{2\mu}{\rho}\nabla\cdot\mathbf{D}_n, \\ \frac{D\mathbf{v}_s}{Dt} &= \chi_n\nabla\mathbf{v}_n^T\mathbf{v}_{ns} - \frac{\nabla p}{\rho} + s\nabla T, \end{aligned} \quad (5)$$

where $\mu > 0$ is the dynamic viscosity, and $\beta > 0$ is a diffusion parameter,

$$\mathbf{D}_n = \frac{1}{2}(\nabla\mathbf{v}_n + \nabla\mathbf{v}_n^T) \quad (6)$$

is a normal velocity deformation tensor, and

$$\zeta = \beta|\nabla T|^2 + 2\mu|\mathbf{D}_n|^2 \quad (7)$$

is the dissipative power.

Although SPH can compute reversible flows, the stabilization of entropy helps to prevent the self-emergence of disorder. Numerical noise is a recognized problem in explicit SPH, which makes velocity converge to Boltzmann distribution and eventually leads to the unphysical gas-like behavior of simulated particles.²³ We stabilize by adding a “small Laplacian” to the right-hand side of the entropic balance. Particle shifting³² would be an alternative remedy.

C. Constitutive laws

Closing the system (5) requires the knowledge of functions p , T , and χ_n . To the best of our knowledge, there is no theory that would express the energy of helium-4 for wide range of s , ρ , v_{ns}^2 and be in agreement with experiments. However, we point out that due to extremely good heat conducting properties of helium-4,³⁰ large temperature gradients are unlikely to exist in practice. For instance, the superfluid fountain, which is the main interest of this paper, can be powered by temperature difference between a heater and a reservoir as small as 10^{-3} K.² Thus, it should be sufficient to use a linearized model, which is valid in a vicinity of certain referential temperature T_0 . For χ_n , χ_s , we use

$$\begin{aligned} \chi_n &= \chi_{n0} + \chi'(s - s_0), \\ \chi_s &= \chi_{s0} - \chi'(s - s_0), \end{aligned} \quad (8)$$

where χ' , χ_{n0} , χ_{s0} , and s_0 are constant values at T_0 .

Yet, how does the energy depend on the state variables s , ρ , \mathbf{v}_{ns} , and \mathbf{v} ? By means of Galilean invariance, it can be derived that differential of the specific total energy e must be

$$de = \mathbf{v}_n \cdot d\mathbf{v} - \chi_s\mathbf{v}_{ns} \cdot d\mathbf{v}_s + \frac{p}{\rho^2}d\rho + Tds \quad (9)$$

and that energy has to be in the form of

$$e = \frac{1}{2}v^2 + \frac{\chi_s}{2\chi_n}(v - v_s)^2 + e_0(\rho, s); \quad (10)$$

see Appendix A for details.

In the absence of any flow ($\mathbf{v} = \mathbf{v}_{ns} = \mathbf{v}_s = 0$), the last undetermined term in the formula for energy (10) can be found by comparison with experimental data. Its differential reads

$$de_0 = Tds + \frac{p}{\rho^2}d\rho. \quad (11)$$

Due to the low compressibility and thermal expansion coefficient,⁵⁷ we can estimate the pressure as an affine function of density

$$p = u_1^2(\rho - \rho_0), \quad (12)$$

where ρ_0 and u_1 are a referential density and the first speed of sound.

Similarly, in the absence of any flow, we can use

$$T = \left(1 + \frac{s - s_0}{C}\right)T_0 \quad (\text{for } \mathbf{v}_s = \mathbf{v}_n = 0), \quad (13)$$

where C is a referential heat capacity. Below T_λ , heat capacity is connected to the second speed of sound u_2 by²⁷

$$u_2^2 = \frac{\chi_{s0}T_0s_0^2}{\chi_{n0}C}. \quad (14)$$

Finally, we integrate (12) and (13) and substitute them in Eq. (10) to obtain the following approximate total-energy formula:

$$\begin{aligned} e &= \frac{1}{2}v^2 + \frac{1}{2}\frac{\chi_s}{\chi_n}(v - v_s)^2 + u_1^2\left(\ln\left(\frac{\rho}{\rho_0}\right) + \frac{\rho_0}{\rho} - 1\right) \\ &\quad + T_0(s - s_0) + \frac{T_0}{2C}(s - s_0)^2. \end{aligned} \quad (15)$$

Table I contains values of C , χ_{n0} , χ_{s0} , s_0 , χ' , ρ_0 , and u_1 for a given T_0 obtained from tabulated experimental data. For a comprehensive collection of measured values, we refer to Donnelly and Barenghi.⁶

TABLE I. Parameters used in simulations. We list only values relevant to the simulation output.

| | Cavity | Second sound | Fountain effect |
|------------------|-----------------------|-------------------------------|-------------------------------|
| T_0 | | 1.9 K | 1.65 K |
| ρ_0 | 1 | 145.5 kg/m ³ | 145.2 kg/m ³ |
| s_0 | | 725.5 J/(kg K) | 335.0 J/(kg K) |
| χ_{n0} | 1 | 0.4195 | 0.1934 |
| χ' | 0 | 5.697×10^{-4} kg K/J | 5.851×10^{-4} kg K/J |
| u_1 | 20 | 40 m/s | 40 m/s |
| u_2 | | 18.83 m/s | 20.37 m/s |
| C | | 3902 J/(kg K) | 1861 J/(kg K) |
| μ | $\frac{1}{\text{Re}}$ | 0 | 10^{-4} kg/(m s) |
| β | 0 | 0 | $\frac{d\rho_0s_0^2}{200u_2}$ |
| δr | $\frac{1}{N}$ | $\frac{L}{N}$ | $\frac{d}{40}$ |
| h | $3\delta r$ | $3\delta r$ | $2.8\delta r$ |
| δt | $\frac{h}{10u_1}$ | $\frac{h}{Mu_1}$ | $\frac{h}{5u_1}$ |
| t_{end} | 40 | $\frac{\sqrt{2}L}{u_1}$ | 0.3 s |
| H | | | 2×10^{-3} m |

D. Discrete space

In SPH, derivatives are approximated by transferring them onto a convenient *smoothing kernel* function $w = w(r)$, which satisfies

$$\int_{\mathbb{R}^d} w(r) \mathbf{d}r = 1, \quad (16)$$

where d is the geometric dimension of a simulation, usually 1 or 2 (for translationally symmetrical problems) or 3. In this paper, we will use the Wendland's kernel function:

$$w(r) = \begin{cases} \frac{q_d}{h^d} \left(1 - \frac{r}{2h}\right)^4 \left(1 + \frac{2r}{h}\right), & r \leq 2h, \\ 0, & r \geq 2h, \end{cases} \quad (17)$$

where

$$\begin{cases} q_2 = \frac{7}{4\pi}, \\ q_3 = \frac{21}{16\pi}. \end{cases} \quad (18)$$

Here, constant h is called the *smoothing length*. Wendland's kernel is often advantageous to the Gaussian kernel because it has compact support and is defined via a piece-wise polynomial functions, which are easy to evaluate.

In our numerical method, superfluid is represented by N particles with positions \mathbf{r}_a for $a = 1, 2, \dots, N$. Each particle has a certain velocity \mathbf{v}_a , superflow velocity $\mathbf{v}_{s,a}$ density ρ_a , entropy s_a , and temperature T_a and moves as a material point. At initial time, they can be arranged in a grid, such that particle a is centered in a cell of mass m_a (often, m_a can be chosen the same for every a). Replacing continuous derivatives using SPH techniques yields a system of ordinary differential equations, which are given as follows:

$$\begin{aligned} \dot{\rho}_a &= \sum_b m_b \frac{w'_{ab}}{r_{ab}} \mathbf{r}_{ab} \cdot \mathbf{v}_{ab}, \\ \dot{s}_a &= - \sum_b m_b \frac{w'_{ab}}{r_{ab}} \left(\frac{1}{\rho_a^2} \mathbf{j}_a \cdot \mathbf{r}_{ab} + \frac{1}{\rho_b^2} \mathbf{j}_b \cdot \mathbf{r}_{ab} - \frac{2\beta T_{ab}}{\rho_a \rho_b} \right) \\ &\quad + \frac{\zeta_a}{T_a \rho_a}, \\ \dot{\mathbf{v}}_a &= - \sum_b m_b \frac{w'_{ab}}{r_{ab}} \left(\frac{1}{\rho_a^2} \Pi_a + \frac{1}{\rho_b^2} \Pi_b \right) \mathbf{r}_{ab} \\ &\quad + \sum_b m_b \frac{w'_{ab}}{r_{ab}} \frac{2(d+2)\mu}{\rho_a \rho_b} \frac{\mathbf{v}_{n,ab} \cdot \mathbf{r}_{ab}}{r_{ab}^2 + \eta^2} \mathbf{r}_{ab}, \\ \dot{\mathbf{v}}_{s,a} &= - \sum_b m_b \frac{w'_{ab}}{r_{ab}} \frac{\chi_{n,a}}{\rho_a} (\mathbf{v}_{n,ab} \cdot \mathbf{v}_{ns,a}) \mathbf{r}_{ab} \\ &\quad - \sum_b m_b \frac{w'_{ab}}{r_{ab}} \left(\frac{p_a}{\rho_a^2} + \frac{p_b}{\rho_b^2} + \frac{s_a}{\rho_a} T_{ab} \right) \mathbf{r}_{ab}, \\ \dot{\mathbf{r}}_a &= \mathbf{v}_a, \end{aligned} \quad (19)$$

where for every particle indices a, b

$$\begin{aligned} \mathbf{r}_{ab} &= \mathbf{r}_a - \mathbf{r}_b, \\ r_{ab} &= |\mathbf{r}_{ab}|, \\ w_{ab} &= w(r_{ab}), \\ w'_{ab} &= \frac{dw}{dr}(r_{ab}), \\ \mathbf{v}_{ab} &= \mathbf{v}_a - \mathbf{v}_b, \\ \mathbf{v}_{n,ab} &= \mathbf{v}_{n,a} - \mathbf{v}_{n,b}, \\ T_{ab} &= T_a - T_b, \end{aligned} \quad (20)$$

the entropy flux and the momentum flux are

$$\begin{aligned} \mathbf{j}_a &= \rho_a s_a \chi_{s,a} \mathbf{v}_{ns,a}, \\ \Pi_a &= p_a \mathbf{I} + \rho_a \chi_{n,a} \chi_{s,a} \mathbf{v}_{ns,a} \otimes \mathbf{v}_{ns,a}, \end{aligned} \quad (21)$$

the normal and counterflow velocity can be expressed via

$$\begin{aligned} \mathbf{v}_{n,a} &= \frac{\mathbf{v}_a - \chi_{s,a} \mathbf{v}_{s,a}}{\chi_{n,a}}, \\ \mathbf{v}_{ns,a} &= \frac{\mathbf{v}_a - \mathbf{v}_{s,a}}{\chi_{n,a}}, \end{aligned} \quad (22)$$

and the dissipative power on particle a is

$$\zeta_a = -\beta \sum_b \frac{m_b w'_{ab}}{\rho_b r_{ab}} T_{ab}^2 - 2\mu(d+2) \sum_b \frac{m_b (\mathbf{v}_{n,ab} \cdot \mathbf{r}_{ab})^2}{\rho_b r_{ab}^2 + \eta^2} \frac{w'_{ab}}{r_{ab}}. \quad (23)$$

The entropy production term in this form is also present in the SDPD (Smoothed Dissipative Particle Dynamics) method.⁸ A numerical parameter $\eta = \frac{h}{10}$ prevents division by zero when two particles overlap. For detailed explanation of how Eqs. (19) are obtained, we refer to [Appendix B](#), where we also prove that they conserve energy and momentum and satisfy the entropic inequality. An important aspect of our method is that the do-nothing condition represents a free adiabatic surface. This means that, conveniently, free surfaces do not require any implementation and particles on this boundary do not need to be identified. Helium vapors are not modeled in this approach. Note that by this, we neglect any aerodynamic effects induced by vapors on liquid helium.

Instead of updating density iteratively, we prefer to use an equivalent closed formula

$$\rho_a = \sum_b m_b w_{ab} + C_a, \quad (24)$$

where C_a is an integration constant specified by the initial condition. This avoids accumulation of time discretization errors.

E. Discrete time

Simple explicit integrators, like leap-frog, are commonly used in SPH codes. In this paper, we employ the following scheme, which is very similar to leapfrog, except we update entropy and density using mid-time positions:

0. (initial step only) find rate of \mathbf{v} and \mathbf{v}_s
1. update \mathbf{v} and \mathbf{v}_s by $\frac{\delta t}{2}$ step
2. update \mathbf{x} by $\frac{\delta t}{2}$ step

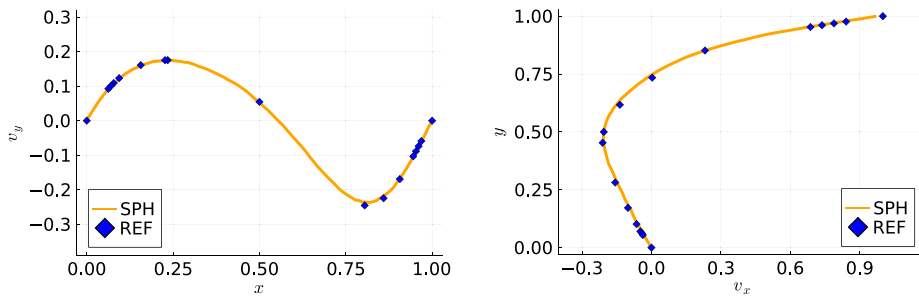


FIG. 1. SPH result compared to the referential solution for $Re = 100$ and $N = 336$. Left: y -component of velocity for $y = 0.5$. Right: x -component of velocity for $x = 0.5$.

3. recompute the cell list and find ρ
4. find the rate of s
5. update s by $\frac{\delta t}{2}$ step
6. update \mathbf{x} by $\frac{\delta t}{2}$ step
7. recompute the cell list and find ρ
8. find the rate of \mathbf{v} and \mathbf{v}_s
9. update \mathbf{v} and \mathbf{v}_s by $\frac{\delta t}{2}$ step

In each step, rates are evaluated using the most recently computed values of $s, \rho, \mathbf{v}, \mathbf{v}_s$, and \mathbf{x} .

III. NUMERICAL EXPERIMENTS

A. Lid-driven cavity

Before we jump to examples involving actual superfluidity, we assess the validity of our model for classical fluid (Navier–Stokes equations), which can be understood as a special case of system (1) for $\chi_s = 0$. Clearly, our discrete equations (19) must work for classical fluids; otherwise, there would be no hope to use them on more complex problems.

Lid-driven cavity is usually formulated as a dimensionless problem: Incompressible, viscous flow is confined in a box $(0, 1) \times (0, 1)$. No slip boundary is prescribed at the left, bottom, and right walls. At the top, velocity is $\mathbf{v} = (1, 0)^T$, density is $\rho_0 = 1$, and viscosity $\mu = \frac{1}{Re}$. Reynolds number Re has various values.

Walls are implemented using a layer of *dummy particles*, which are treated normally with the exception that their velocities are constantly zero. The lid is also implemented this way, but with velocity $\mathbf{v}_a = (1, 0)^T$ appearing in the evaluation of viscous forces. The list of simulation parameters is displayed in Table I. We measure transverse velocities along x and y centerlines and compare them to a reference solution by Ghia *et al.*¹² The results are shown in Figs. 1–3 and convergence curve in Fig. 4. Error grows approximately linearly with $\delta r = \frac{1}{N}$.

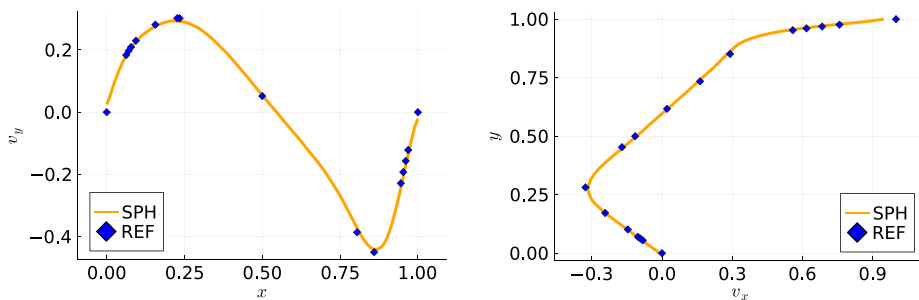


FIG. 2. SPH result compared to the referential solution for $Re = 400$ and $N = 336$. Left: y -component of velocity for $y = 0.5$. Right: x -component of velocity for $x = 0.5$.

B. Second sound waves

Contrary to the previous case, we will now investigate a situation where coflow velocity is almost zero. Let us consider a standing wave of second sound, written in terms of entropy as

$$s(\mathbf{x}, t) = s_0 + As_0 \sin\left(\frac{\pi x}{L}\right) \sin\left(\frac{\pi y}{L}\right) \cos\left(\frac{\sqrt{2}\pi u_2 t}{L}\right) \quad (25)$$

for $\mathbf{x} \in \Omega = (0, L) \times (0, L)$ and $L = 1$ cm. This is an approximate solution of continuous two-fluid equation (1) linearized around $\mathbf{v} = \mathbf{v}_s = \mathbf{0}$, $\rho = \rho_0$, and $s = s_0$. As a test of consistency, we would like to verify that our numerical model approaches (25) for fine resolution and small data ($A \rightarrow 0$). We impose initial condition

$$\begin{aligned} \rho(\mathbf{x}, 0) &= \rho_0, \\ s(\mathbf{x}, 0) &= s_0 + As_0 \sin\left(\frac{\pi x}{L}\right) \sin\left(\frac{\pi y}{L}\right), \quad \mathbf{x} \in \Omega, \\ \mathbf{v}(\mathbf{x}, 0) &= \mathbf{v}_s(\mathbf{x}, 0) = \mathbf{0} \end{aligned} \quad (26)$$

and free adiabatic boundaries. Particles are initially arranged on a Vogel spiral with spatial step $\delta r = \frac{L}{N}$. Time step is $\delta t = \frac{L}{Mu_1}$, and we end the simulation at $t = \frac{\sqrt{2}L}{u_2}$. Let us define two types of errors. First, a normalized $l^\infty \rightarrow l^2$ error

$$\epsilon_1 = \max_n \sqrt{\sum_a \left| \frac{s_a(t_n) - s_{\text{exact}}(\mathbf{x}_a, t_n)}{As_0} \right|^2}. \quad (27)$$

Second, a dimensionless energy error

$$\epsilon_2 = \max_n \left| \frac{\sum_a e_a(t_n)}{\sum_a e(0)} - 1 \right|. \quad (28)$$

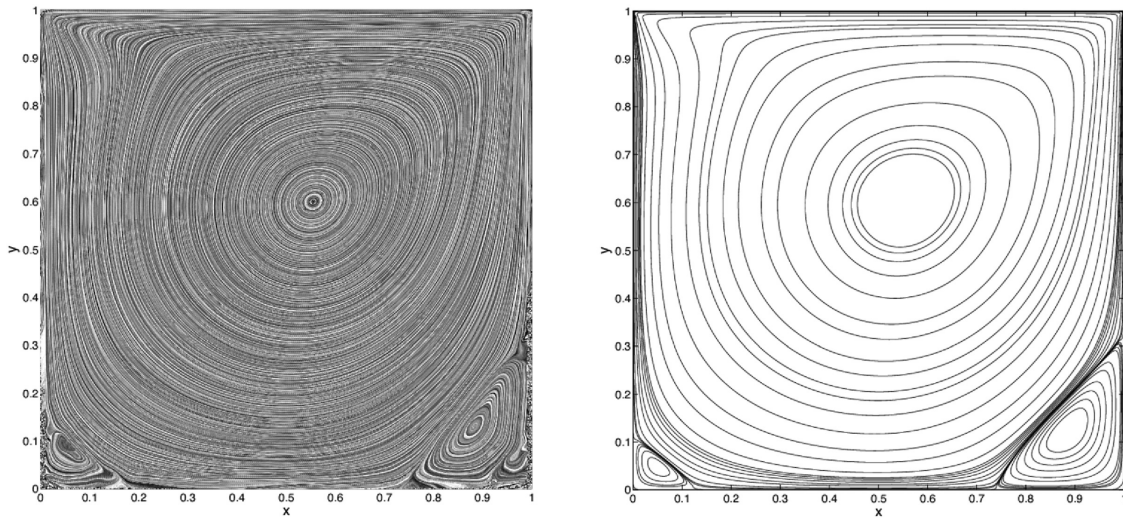


FIG. 3. The streamline plot for $Re = 400$. Left: Our SPH result. Image created using line integral convolution in Paraview.⁴⁸ Right: Reference solution.⁹

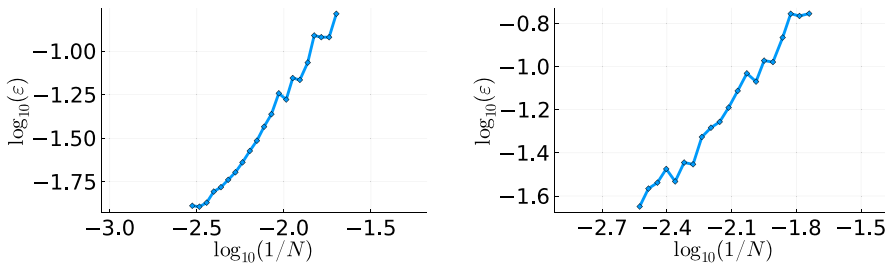


FIG. 4. Convergence curves for $Re = 100$ (left) and $Re = 400$ (right). Error is measured as a maximum distance from reference data. Regression slopes were 0.998 and 1.189, respectively, suggesting approximately linear convergence.

Figure 5 shows the results for various values of A , N , and M . We observe that energy error is very small and we can also achieve satisfactory ϵ_1 error below 1% (see Fig. 6). It is likely that the convergence rate could be improved with renormalized operators.³⁷

C. Fountain effect (two-dimensional)

Unlike the two previous examples, in superfluid fountain effect, coflow and counterflow are equally significant. Let us begin by describing our idealized setting. A cell (with shape indicated in Fig. 7) is submerged in liquid helium-4 at temperature $T_0 = 1.65$ K. In its center,

there is a point heat source of constant power \dot{W} . The cell is insulated by adiabatic walls and a thin superleak at the bottom.

In (19), we add gravitational acceleration \mathbf{g} , superleak friction force $\mathbf{f}_{\text{sup},a}$, and dissipative power from heater $\zeta_{\text{heater},a}$,

$$\begin{aligned} \dot{s}_a &= \dots + \frac{1}{T_a \rho_a} \zeta_{\text{heat},a}, \\ \dot{\mathbf{v}}_a &= \dots + \mathbf{g} + \mathbf{f}_{\text{sup},a}, \\ \dot{\mathbf{v}}_{s,a} &= \dots + \mathbf{g}, \end{aligned} \tag{29}$$

where

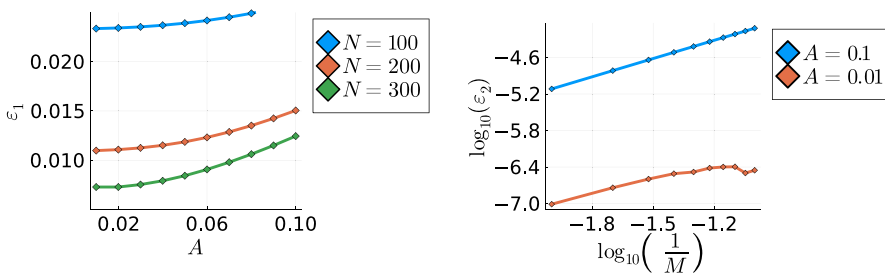


FIG. 5. Left: ϵ_1 error for $M = 50$ and different values of A and N . Right: ϵ_2 error for $N = 200$ and different values of M and A .

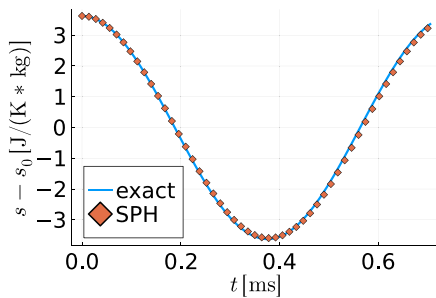


FIG. 6. Evolution of entropy at $x = y = \frac{L}{4}$ in a simulation compared to the formula (25). Result for $A = 0.01$, $M = 50$, and $N = 300$.

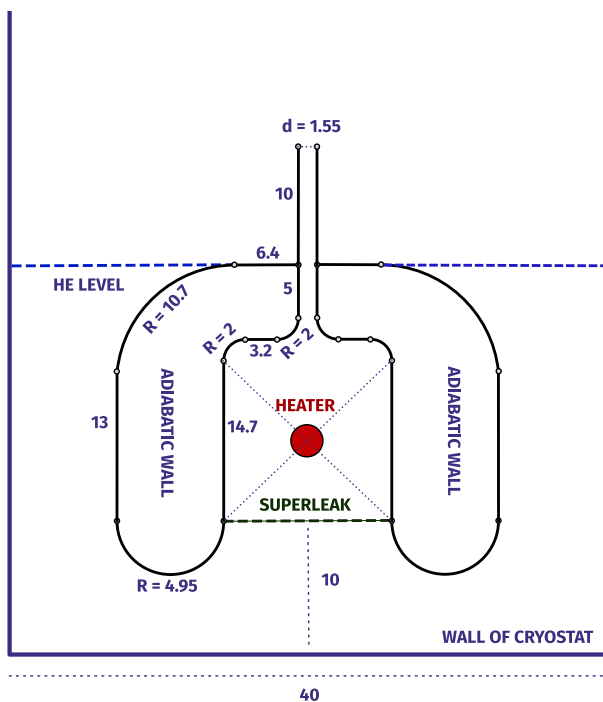


FIG. 7. Scheme of the simulated apparatus. All lengths are expressed in millimeters. Shape is composed of line segments and circular sections with indicated radii.

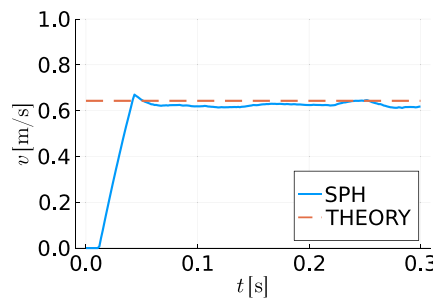
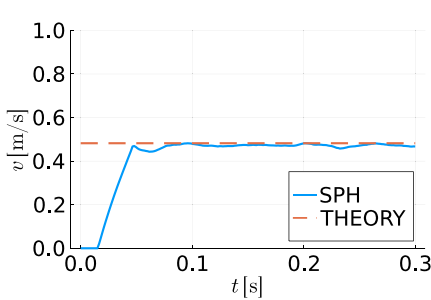


FIG. 8. Evolution of the jet speed in comparison to theoretical prediction (31). The left image is for $\dot{W} = 60 \text{ W/m}$ and the right for $\dot{W} = 80 \text{ W/m}$. The discrepancy for $t \in (0, 0.1\text{s})$ is transitional effect caused by the evolution from the initial state with constant temperature and zero velocity field. Calculating the average for $t > 0.2$, we find that the SPH prediction is smaller than (31) by 1.95% (left image) and 2.38% (right image).

$$\zeta_{\text{heat,a}} = \dot{W} (w_H * \delta_{\{x=x_{\text{heat}}, y=y_{\text{heat}}\}})(\mathbf{r}_a),$$

$$\mathbf{f}_{\text{sup,a}} = -\frac{\chi_{n,a} \mathbf{v}_{n,a}}{\tau} (w_H * \delta_{\{y=y_{\text{sup}}, |x| \leq r_{\text{sup}}\}})(\mathbf{r}_a). \quad (30)$$

Function w_H is the kernel (17) with smoothing length H and $*$ denotes the convolution operator. Mollification by w_H is necessary because it is impossible to work with Dirac distributions in SPH. To ensure that the superleak is practically impenetrable for normal component, relaxation time τ must be as small as $1 \mu\text{s}$. Therefore, it is better to split superleak friction from other forces and compute it implicitly.

Adiabatic walls of the cell are implemented using static dummy particles, which take part only in density and pressure computation. At the walls of the cryostat, let us prescribe no-slip for \mathbf{v} , free condition for \mathbf{v}_s , and Dirichlet condition $S = S_0$ for entropy (which is almost the same as $T = T_0$). Consequently, the wall acts as a cooler, preventing the temperature from growing indefinitely. This condition is implemented using dummy particles, which we force to have constant entropy and zero coflow velocity, but we allow them to conduct heat.

In the initial state, $\mathbf{v} = \mathbf{v}_s = \mathbf{0}$ and $T = T_0$ everywhere. A fountain is quickly generated. The speed of the jet is measured by counting particles that escape from the cell in a given time window. We then compare these numbers to a theoretical formula from the book by Landau and Lifshitz,²⁹ which we adapted to a two-dimensional flow

$$v_{\text{jet,ideal}} = \frac{\dot{W}}{T s \rho d}, \quad (31)$$

where T, s , and ρ are values of temperature, entropy density, and mass density inside the cell (which are nearly constant). We should emphasize that (31) is merely an approximation as it does not take into account heat loss through capillary and dissipative effects. It is not very clear whether the corrected value of v_{jet} should be above or below the theoretical estimate. Assuming stationary state, the balance of entropy yields

$$0 = \frac{d}{dt} \int_{\text{cell}} s dm = \frac{\dot{W}_{\text{heater}}}{T} + \frac{1}{T \rho} \int_{\text{cell}} \zeta dm - s \rho d v_{n,\text{jet}}, \quad (32)$$

where the dissipative power ζ is positive. This would, paradoxically, predict that $v_{\text{jet,ideal}}$ is a *lower estimate* when dissipation is considered. However, a counterflow can occur through capillary, which means that the normal speed $v_{n,\text{jet}}$ can be different from v_{jet} . Additionally, heat can partially escape through walls and superleak in practice. Measurements by Amigó *et al.*² report values both slightly lower and higher than (31).

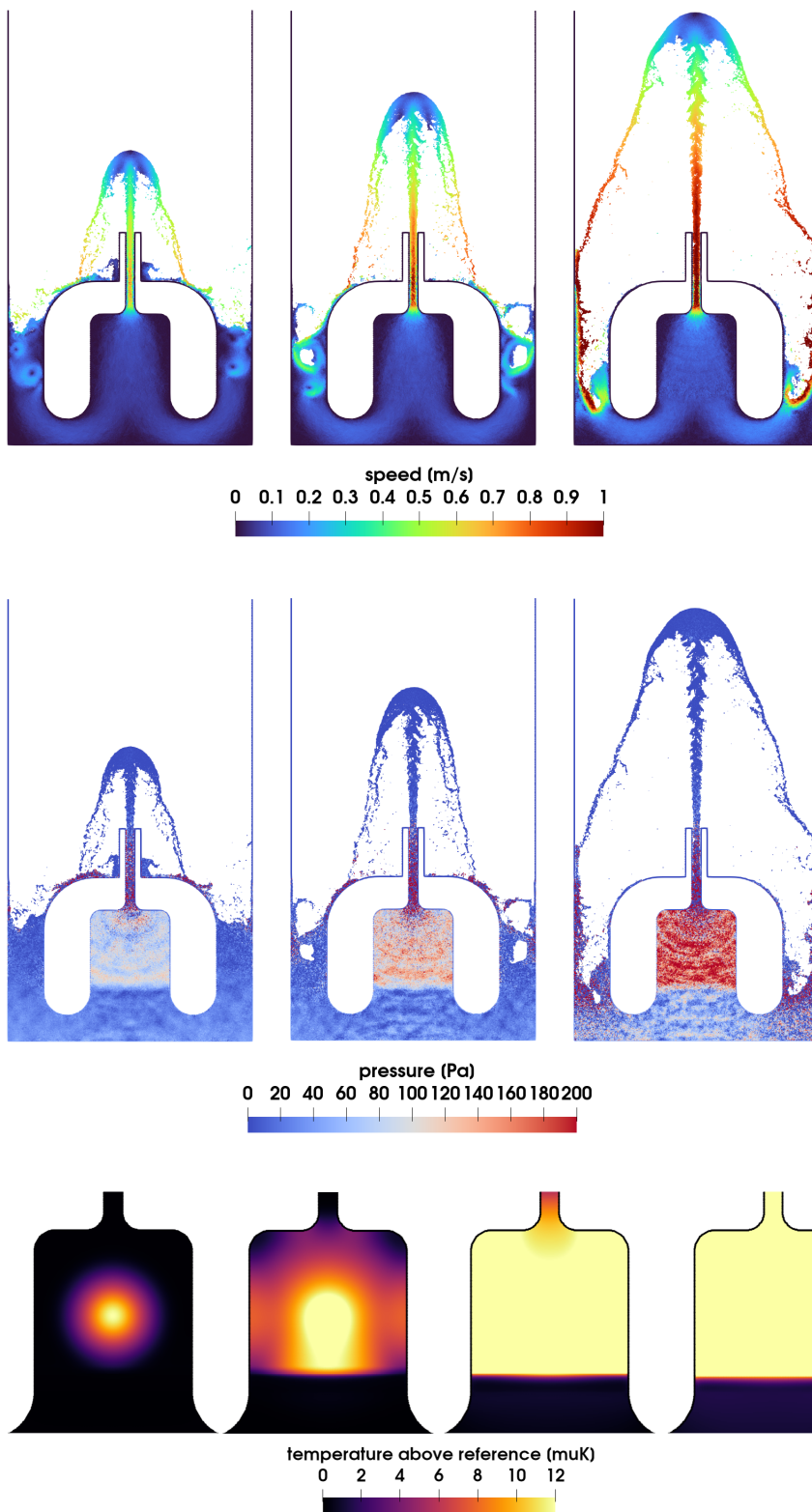


FIG. 9. Coflow velocity plot (up) and pressure plot (down) at $t = 0.3$ s for different values of heating power. From left to right: $W = 60, 80,$ and 100 W/m. Each simulation consists of approximately 200 000 particles. The pressure is very noisy, especially in the capillary and the plunge pool.

FIG. 10. Plot of temperature inside the cell at $t = 0.25, 0.5, 0.75,$ and 1 ms (from left to right).

27 September 2023 14:08:17

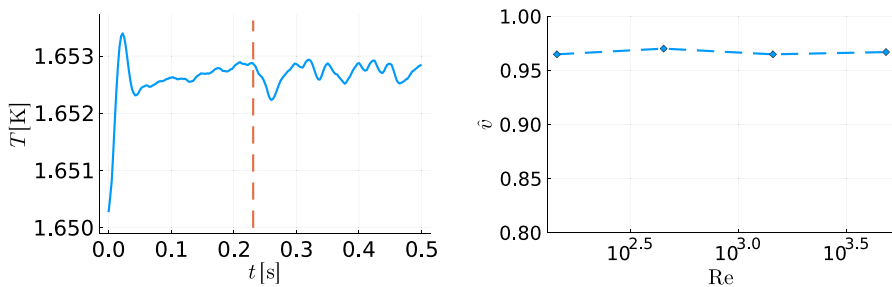


FIG. 11. Left: Evolution of temperature in time for $W = 80$ W/m. The dashed orange line indicates when the fountain connects with the cryostat. Right: Relative jet speed $\bar{v} = v_{jet}/v_{jet,ideal}$ (averaged over time) for various values of Re .

The Reynolds number can be given as follows:

$$Re = \frac{\rho_0 d v_{jet,ideal}}{\mu} = \frac{\dot{W}}{Ts\mu}. \quad (33)$$

With $\mu = 1.296 \times 10^{-6}$ Pa s, this yields Re in the range of hundreds of thousands for reasonably high values of power. Therefore, classical turbulence appears in the simulation, which is difficult to resolve without a dedicated turbulent model. We sidestep this problem by choosing an artificial μ , keeping the Reynolds number around 1500. A parameter analysis reveals that the relative jet speed does not vary significantly with Re for values in range 100–1500, which are accessible to our model—see Fig. 11.

The simulation never reaches a stationary state, but the jet speed is relatively stable after a brief transitional period. Figure 8 shows that the computed jet speed is very close to the value (31) but slightly lower

on average. Figure 9 shows the shape of the fountain, velocity, and pressure. The simulation remains stable even during the violent impact of jetted helium. Figure 10 shows the temperature in the first millisecond of simulated time. After this short period, second sound waves fill the cell, and temperature gradients vanish, except for a steep jump at the superleak. The subsequent evolution is shown in Figs. 11 and 12. When the fountain connects with colder helium in the cryostat, a temporary drop in temperature occurs. Nonetheless, the effect of the second sound traveling upstream and entering the cell through the capillary was not observed. Table I lists all simulation parameters for reproduction purposes.

IV. CONCLUSION

We described a new energy-conserving SPH-based numerical method for superfluid helium. We verified its validity in three essential

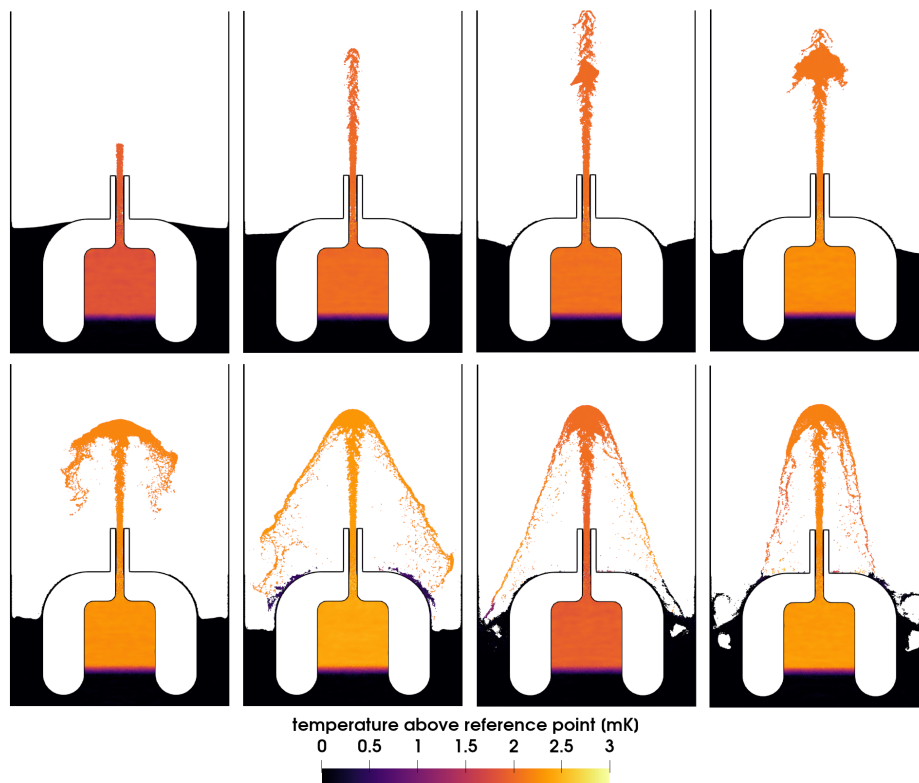


FIG. 12. Plot of temperature distribution and fountain shape for $W = 80$ W/m at equally spaced time frames from 37.5 to 300 ms.

test cases, demonstrating that the technique can accurately capture coflow and thermally driven counterflow. Our fountain effect simulation verifies the applicability of the formula for fountain jet speed by Landau and Lishitz.

The numerical scheme discretizes a Hamiltonian one-fluid formulation generalizing the Landau–Tisza two-fluid model. We also provide a closed form of the energy functional in terms of density, coflow velocity, entropy density, and superfluid velocity, which has been missing in the literature.

In the future, we would like to enrich our discrete system by implementing the dissipative effects of quantum vorticity. Particle simulation of Rollin films is another promising research direction, as well as simulation of helium droplets,²⁴ or simulation of inertial particles in superfluid helium.⁴⁵ Moreover, the mesh-free nature of SPH is advantageous in multiphase flow simulations, including phase change.^{34,63} Consequently, we expect that this method could be extended to simulate solidification and evaporation in superfluid helium.

ACKNOWLEDGMENTS

O.K. and D.S. were supported by Project No. START/SCI/053 of Charles University Research program. M.P. was supported by Czech Science Foundation, Project No. 23-05736S.

AUTHOR DECLARATIONS

Conflict of Interest

The authors have no conflicts to disclose.

Author Contributions

Ondřej Kincl: Investigation (equal); Methodology (equal); Software (equal); Visualization (lead); Writing – original draft (lead). **David Schmoranzner:** Investigation (equal); Methodology (equal); Supervision (equal); Writing – review & editing (equal). **Michal Pavelka:** Investigation (equal); Methodology (equal); Supervision (equal); Writing – review & editing (equal).

DATA AVAILABILITY

The data that support the findings of this study are available within the article.

APPENDIX A: DERIVATION OF THE MODEL

This appendix contains a derivation of model (1) from a Hamiltonian formulation of superfluid-helium dynamics.^{50,59} The field of superfluid density interacts with itself partly due to the convective term and partly due to the presence of quantum vortices. When the reversible (non-dissipative) part of interactions mediated by quantum vortices is taken into account, we obtain a system of four Hamiltonian equations for four state variables (mass density ρ , momentum density \mathbf{m} , volumetric entropy density \bar{s} , and superfluid velocity \mathbf{v}_s) as follows:

$$\frac{\partial \rho}{\partial t} = -\partial_k(\rho E_{m_k} + E_{v_{sk}}), \quad (\text{A1a})$$

$$\begin{aligned} \frac{\partial m_i}{\partial t} = & -\partial_j(m_i E_{m_j}) - \partial_j(v_{sj} E_{v_{sj}}) - \rho \partial_i E_\rho \\ & - m_j \partial_i E_{m_j} - \bar{s} \partial_i E_{\bar{s}} - v_{sk} \partial_i E_{v_{sk}} + \partial_i(E_{v_{sk}} v_{sk}), \end{aligned} \quad (\text{A1b})$$

$$\frac{\partial \bar{s}}{\partial t} = -\partial_k(\bar{s} E_{m_k}), \quad (\text{A1c})$$

$$\frac{\partial v_{sk}}{\partial t} = -\partial_k E_\rho - \partial_k(v_{sj} E_{m_j}) + (\partial_k v_{sj} - \partial_j v_{sk}) \left(E_{m_j} + \frac{1}{\rho} E_{v_{sj}} \right), \quad (\text{A1d})$$

where the total energy E with subscripts stands for functional derivatives of the energy with respect to the fields in the subscript. In particular, $E_s = T$ is the temperature, $E_m = \mathbf{v}_n$ is the normal velocity, and E_ρ is the generalized chemical potential μ . The derivative E_{v_s} has no particular name, but it is investigated below. Equations (A1) represent a Hamiltonian system generated by a Poisson bracket that is derived from quantum commutators and dynamics of vortices^{7,60} or by the requirement of unconditional validity of Jacobi identity.⁵⁰ Note that these equations differ from those of Landau and Tisza in the terms coupling the evolution of \mathbf{v}_s with the derivative of energy with respect to \mathbf{v}_s , which are a consequence of the vortex dynamics or of the Jacobi identity.

In order to close evolution equations (A1), we have to provide an energy functional $E = \int \bar{e} d\mathbf{r}$. We assume that the volumetric energy density $\bar{e}(\rho, \mathbf{m}, s, \mathbf{v}_s) = \rho e(\rho, \mathbf{v}, s, \mathbf{v}_s)$ is a smooth function of the state variables (not a function of gradients of the state variables). This assumption excludes, for instance, any explicit dependence of energy on superfluid vorticity $\boldsymbol{\omega} = \nabla \times \mathbf{v}_s$.^{7,17} Moreover, from the requirement of Galilean invariance,^{28,39} it follows that the energy must be in the form

$$\bar{e} = \bar{e}(\rho, s, \mathbf{m} - \rho \mathbf{v}_s) + (\mathbf{m} - \rho \mathbf{v}_s) \cdot \mathbf{v}_s + \frac{1}{2} \rho \mathbf{v}_s^2, \quad (\text{A2})$$

where $\bar{e}(\rho, s, \mathbf{m}_0)$, denoting $\mathbf{m}_0 = \mathbf{m} - \rho \mathbf{v}_s$, is the volumetric energy density in the frame of reference co-moving with the superfluid velocity (to be further specified below).

To obtain model (1), however, we have to transform the momentum density and volumetric entropy density to the overall velocity $\mathbf{v} = \mathbf{m}/\rho$ and entropy density per mass, $s = \bar{s}/\rho$. Derivatives of the energy density with respect to momentum density and superfluid velocity are

$$\mathbf{v}_n = \frac{\partial \bar{e}}{\partial \mathbf{m}} = \frac{\partial \bar{e}}{\partial \mathbf{m}_0} + \mathbf{v}_s, \quad (\text{A3})$$

Because the energy \bar{e} depends only on the norm of \mathbf{m}_0 , not on its direction,⁷ we can introduce an auxiliary field called normal density ρ_n

$$\rho_n \stackrel{\text{def}}{=} \frac{\mathbf{m}_0}{\mathbf{v}_n - \mathbf{v}_s}, \quad (\text{A4})$$

because the nominator and denominator are collinear due to Eq. (A3). This, in turn, allows to define superfluid density as $\rho_s \stackrel{\text{def}}{=} \rho - \rho_n$, which gives the usual formula $\mathbf{m} = \rho_s \mathbf{v}_s + \rho_n \mathbf{v}_n$. It should be kept in mind, however, that ρ_n and ρ_s are just auxiliary variables determined from the actual form of energy, not state variables. This can be seen for instance from that there are two scalar equations in Eqs. (A1) (for the overall density and entropy density),

and so if auxiliary field ρ_n were taken as a state variable, one scalar evolution equation would be missing. Nevertheless, it is customary in the two-fluid models of superfluid helium-4 to discuss superfluid and normal densities,²⁹ so we formulate our model in terms of the auxiliary fields for better readability.

When we have experimental data on the dependence $\frac{\rho_n}{\rho}(T)$, which is often the case,³ Eq. (A3) actually represents a differential equation for \bar{e}_0

$$\frac{\rho_n(\rho, s)}{\rho} = \frac{m_0}{\rho \left(\frac{\partial \bar{e}}{\partial m_0} \right)_{\rho, s}}. \quad (\text{A5})$$

A general solution to this equation is

$$\bar{e} = \frac{m_0^2}{2\rho_n(\rho, s)} + \bar{e}_0(\rho, s), \quad (\text{A6})$$

where $\bar{e}_0(\rho, s)$ is an integration constant (volumetric energy density in the absence of any flow). In terms of the auxiliary densities (ρ_n and χ_n), the energy density becomes

$$\begin{aligned} \bar{e} &= \frac{1}{2} \chi_n(\rho, s) v_n^2 + \frac{1}{2} \chi_s(\rho, s) v_s^2 + \bar{e}_0(\rho, s) \\ &= \frac{1}{2} \frac{\rho}{\chi_n(\rho, s)} (\mathbf{v}_n - \mathbf{v}_s)^2 + \bar{e}_0(\rho, s), \end{aligned} \quad (\text{A7})$$

and the overall energy density per mass is then

$$e(\rho, \mathbf{v}_s, \mathbf{v}_s) = \frac{1}{2} v^2 + \frac{1}{2} \frac{\chi_s}{\chi_n} (\mathbf{v} - \mathbf{v}_s)^2 + e_0(\rho, s), \quad (\text{A8})$$

where $e_0 = \bar{e}_0(\rho, \rho s)/\rho$ (energy density per mass in the absence of any flow) is to be determined from thermodynamic data.

The derivative of energy with respect to the superfluid density reads

$$\rho \frac{\partial e}{\partial v_s} = \frac{\partial \bar{e}}{\partial v_s} = -\rho \frac{\partial \bar{e}}{\partial m_0} + \mathbf{m} - \rho v_s = -\rho_s v_{ns}, \quad (\text{A9})$$

where $v_{ns} = \mathbf{v}_n - \mathbf{v}_s$ is the counterflow velocity. The remaining two derivatives (with respect to ρ and s) transform as

$$\frac{\partial \bar{e}}{\partial \rho} = e + \rho \left(\frac{\partial e}{\partial \rho} - \frac{\partial e}{\partial s} \frac{s}{\rho} - \frac{\partial e}{\partial \mathbf{v}} \cdot \frac{\mathbf{v}}{\rho} \right), \quad (\text{A10})$$

$$\frac{\partial \bar{e}}{\partial s} = T = \frac{\partial e}{\partial s}. \quad (\text{A11})$$

Formulas (A3), (A9), (A10), and (A11) permit us to write the differential of energy density [Eq. (9)],

$$de = \mathbf{v}_n \cdot d\mathbf{v} - \chi_s v_{ns} \cdot d\mathbf{v}_s + \frac{p}{\rho^2} d\rho + T ds. \quad (\text{A12})$$

Hamiltonian equations (A1) then transform to model (1).

In summary, the reversible part of our model [Eqs. (1)] together with the identification of derivatives of energy (9) and a form of the energy itself (determined up to the internal energy) are implied by Hamiltonian mechanics of superfluid helium-4 [Eqs. (A1)] and by the requirement of Galilean invariance. The model is more precise than the standard Landau-Tisza model because it takes into account at least the reversible interaction between the field of superfluid velocity with itself due to the quantum vortices.

This results, for instance, in the presence of convective derivative $\partial_t + \mathbf{v} \cdot \nabla$ in evolution equations for all the state variables, instead of having the superfluid velocity \mathbf{v}_s convected only by itself.⁵³

APPENDIX B: METHOD DERIVATION AND CONSERVATION LAWS

In this appendix, we describe a heuristic derivation of our discrete model from the continuous equations and prove the conservation of energy and momentum and entropic inequality. To simplify, we split the ordinary differential system (B19) into reversible and irreversible parts and establish conservation laws for each separately. This procedure works since a conservation law for a generic ordinary differential equation

$$\dot{\mathbf{y}} = \mathbf{f}(\mathbf{y}) \quad (\text{B1})$$

can be formulated as a geometric condition that \mathbf{f} belongs to the tangent space of a particular manifold. If two different right-hand sides \mathbf{f}_1 and \mathbf{f}_2 satisfy the condition, then so does their sum. A similar argument can be used for entropic inequality when we replace tangent space with a half-space.

1. Reversible part

We shall begin with the reversible part of dynamics

$$\begin{aligned} \frac{D\rho}{Dt} &= -\rho \nabla \cdot \mathbf{v}, \\ \frac{Ds}{Dt} &= -\frac{1}{\rho} \nabla \cdot (\rho s \chi_s \mathbf{v}_{ns}), \\ \frac{D\mathbf{v}}{Dt} &= -\frac{1}{\rho} \nabla \cdot (\rho \chi_n \chi_s \mathbf{v}_{ns} \otimes \mathbf{v}_{ns} + p\mathbf{I}), \\ \frac{D\mathbf{v}_s}{Dt} &= \chi_n \nabla \mathbf{v}_n^T \mathbf{v}_{ns} - \frac{\nabla p}{\rho} + s \nabla T. \end{aligned} \quad (\text{B2})$$

Let us imagine a classical solution to these equations, which lives in a time-dependent domain Ω_t and such that the boundary $\partial\Omega_t$ is an adiabatic free surface, where we assume $\mathbf{v}_{ns} \cdot \mathbf{n} = 0$ and $p = 0$. (Pressure is only relevant up to an additive constant. We fix this constant so that vapor pressure is zero.) The adiabatic free surface is our choice of do-nothing boundary condition. (Implementation of other boundary conditions, such as at the walls of a cryostat, necessitates specific treatment.)

Multiplying equations in (B2) by arbitrary smooth test functions $\tilde{\rho}$, \tilde{s} , $\tilde{\mathbf{v}}$, and $\tilde{\mathbf{v}}_s$ and integrating by parts, we infer

$$\begin{aligned} \int_{\Omega_t} \frac{D\rho}{Dt} \tilde{\rho} \, dm &= - \int_{\Omega_t} \rho \tilde{\rho} \nabla \cdot \mathbf{v} \, dm, \\ \int_{\Omega_t} \frac{Ds}{Dt} \tilde{s} \, dm &= \int_{\Omega_t} s \chi_s \mathbf{v}_{ns} \cdot \nabla \tilde{s} \, dm, \\ \int_{\Omega_t} \frac{D\mathbf{v}}{Dt} \cdot \tilde{\mathbf{v}} \, dm &= \int_{\Omega_t} \chi_n \chi_s (\mathbf{v}_{ns} \otimes \mathbf{v}_{ns}) : \nabla \tilde{\mathbf{v}} \, dm + \int_{\Omega_t} \frac{p}{\rho} \nabla \cdot \tilde{\mathbf{v}} \, dm, \\ \int_{\Omega_t} \frac{D\mathbf{v}_s}{Dt} \cdot \tilde{\mathbf{v}}_s \, dm &= \int_{\Omega_t} \chi_n (\mathbf{v}_{ns} \otimes \tilde{\mathbf{v}}_s) : \nabla \mathbf{v}_n \, dm \\ &\quad + \int_{\Omega_t} \left(\frac{p}{\rho} \nabla \cdot \tilde{\mathbf{v}}_s + s \nabla T \cdot \tilde{\mathbf{v}}_s \right) dm, \end{aligned} \quad (\text{B3})$$

where $dm = \rho dV$. In the next step, we approximate all integrals using particles as quadrature nodes

$$\int_{\Omega_i} \varphi dm \approx \sum_a m_a \varphi_a, \quad \forall \varphi \quad (B4)$$

and replace all derivatives by a discrete SPH operator

$$\partial_i \varphi|_{r=r_a} \approx \{\partial_i \varphi\}_a, \quad (B5)$$

which approximates ∂_i using particle positions and field values and which we specify later. Hence, we find the following “discrete weak formulation:”

$$\begin{aligned} \sum_a m_a \dot{\rho}_a \tilde{\rho}_a &= - \sum_a m_a \rho_a \tilde{\rho}_a \{\nabla \cdot \mathbf{v}\}_a, \\ \sum_a m_a \dot{s}_a \tilde{s}_a &= \sum_a m_a s_a \chi_{s,a} \mathbf{v}_{ns,a} \cdot \{\nabla \tilde{s}\}_a, \\ \sum_a m_a \dot{\mathbf{v}}_a \cdot \tilde{\mathbf{v}}_a &= \sum_a m_a \chi_{n,a} \chi_{s,a} (\mathbf{v}_{ns,a} \otimes \mathbf{v}_{ns,a}) : \{\nabla \tilde{\mathbf{v}}\}_a \\ &\quad + \sum_a m_a \frac{p_a}{\rho_a} \{\nabla \cdot \tilde{\mathbf{v}}\}_a, \\ \sum_a m_a \dot{\mathbf{v}}_{s,a} \cdot \tilde{\mathbf{v}}_{s,a} &= \sum_a m_a \chi_{n,a} (\mathbf{v}_{ns,a} \otimes \tilde{\mathbf{v}}_{s,a}) : \{\nabla \mathbf{v}_n\}_a \\ &\quad + \sum_a m_a \left(\frac{p_a}{\rho_a} \{\nabla \cdot \tilde{\mathbf{v}}_s\}_a + s_a \tilde{\mathbf{v}}_{s,a} \cdot \{\nabla T\}_a \right) \end{aligned} \quad (B6)$$

for all values $\tilde{\rho}_a, \tilde{s}_a, \tilde{\mathbf{v}}_a$, and $\tilde{\mathbf{v}}_{s,a}$. The next logical step is to perform a discrete analogy of integration by parts and localization and express $\tilde{\rho}_a, \tilde{s}_a, \tilde{\mathbf{v}}_a$, and $\tilde{\mathbf{v}}_{s,a}$ explicitly. Before we do that, however, we would like to use (B6) to prove conservation properties.

Definition 1 (order of consistency). A discrete operator $\{\partial_i \cdot\}_a$ is *k-order consistent* if

$$\{\partial_i \varphi\}_a = \partial_i \varphi(\mathbf{r}_a) \quad (B7)$$

for every polynomial of degree at most *k*.

Proposition 1 (conservation laws). If $\{\partial_i \cdot\}_a$ is 0-order consistent for all *a*, then the solution of (B6) satisfies conservation of energy

$$\frac{d}{dt} \left(\sum_a m_a e_a \right) = 0, \quad (B8)$$

entropy

$$\frac{d}{dt} \left(\sum_a m_a s_a \right) = 0, \quad (B9)$$

and momentum

$$\frac{d}{dt} \left(\sum_a m_a \mathbf{v}_a \right) = \mathbf{0}. \quad (B10)$$

If $\{\partial_i \cdot\}_a$ is 1-order consistent for all *a*, then the solution also conserves angular momentum:

$$\frac{d}{dt} \left(\sum_a m_a \mathbf{r}_a \times \mathbf{v}_a \right) = \mathbf{0}. \quad (B11)$$

Proof. For conservation of entropy, we set $\tilde{s}_a = 1, \forall a$ in (B6). The right-hand side of entropy balance vanishes, since $\{\nabla 1\}_a = 0$. For momentum, we proceed similarly, but instead, we choose

$$\tilde{\mathbf{v}} = \begin{pmatrix} 1 \\ 0 \\ 0 \end{pmatrix} \quad \forall a \quad (B12)$$

to show conservation of the first component of momentum, and so on. For energy, we remind that

$$de = \mathbf{v}_n \cdot d\mathbf{v} - \chi_s \mathbf{v}_{ns} \cdot d\mathbf{v}_s + \frac{p}{\rho^2} d\rho + Tds. \quad (B13)$$

Therefore, when we substitute in $\tilde{\mathbf{v}} = \mathbf{v}_n, \tilde{\mathbf{v}}_s = -\chi_s \mathbf{v}_{ns}, \tilde{\rho} = \frac{p}{\rho^2}$, and $\tilde{s} = T$ and sum the four equations, we obtain the desired conservation law.

If our discrete derivative is also first order consistent, then we set

$$\tilde{\mathbf{v}} = \begin{pmatrix} 0 \\ -z_a \\ y_a \end{pmatrix} \quad \forall a. \quad (B14)$$

The right-hand side of momentum equation vanishes due to the anti-symmetry of

$$\{\nabla \tilde{\mathbf{v}}\}_a = \begin{pmatrix} 0 & 0 & 0 \\ 0 & 0 & -1 \\ 0 & 1 & 0 \end{pmatrix} \quad \forall a \quad (B15)$$

and the fact that the double dot product of symmetric and anti-symmetric matrix equals zero. This demonstrates conservation of *x*-component of angular momentum. Conservation of *y* and *z* components follows analogically. \square

In this paper, in sake of simplicity, we use a simple and standard SPH operator

$$\{\partial_i \varphi\}_a := -\frac{1}{\rho_a} \sum_b m_b \frac{w'_{ab}}{r_{ab}} x_{ab}^i \quad (B16)$$

(x^i denotes *i*th component of vector \mathbf{r}), which is merely 0-order consistent. Thus, we conserve all quantities above except for angular momentum. However, operators of order 1 and higher exist and can be found in the literature.³⁷

Proposition 2 (dual operator). For any pair of discrete variables φ, ψ and any coordinate index *i*,

$$\sum_a \frac{m_a}{\rho_a} \{\partial_i \varphi\}_a \psi_a = - \sum_a \frac{m_a}{\rho_a} \varphi_a \{\partial_i \psi\}_a^*, \quad (B17)$$

where $\{\partial_i \varphi\}_a$ is given by (B15) and

$$\{\partial_i \psi\}_a^* := \rho_a \sum_b m_b \left(\frac{\psi_a}{\rho_a^2} + \frac{\psi_b}{\rho_b^2} \right) \frac{w'_{ab}}{r_{ab}} x_{ab}^i. \quad (B18)$$

Proof. Can be found in Ref. 58. \square

Using the dual operator, we can easily solve the algebraic system (B6) and we immediately obtain

$$\begin{aligned} \dot{\rho}_a &= -\rho_a \{\nabla \cdot \mathbf{v}\}_a, \\ \dot{s}_a &= -\frac{1}{\rho_a} \{\nabla \cdot (\rho s \chi_s \mathbf{v}_{ns})\}_a^*, \\ \dot{\mathbf{v}}_a &= -\frac{1}{\rho_a} \{\nabla \cdot (\rho \chi_n \chi_s \mathbf{v}_{ns} \otimes \mathbf{v}_{ns} + p\mathbf{I})\}_a^*, \\ \dot{\mathbf{v}}_{s,a} &= \chi_{n,a} \{\nabla \mathbf{v}_n^T\}_a \mathbf{v}_{ns,a} - \frac{1}{\rho_a} \{\nabla p\}_a^* + s_a \{\nabla T\}_a, \end{aligned} \quad (B19)$$

and this is precisely the reversible component of (B19).

2. Irreversible part

Next, we turn our attention to the irreversible part of dynamics, which is

$$\begin{aligned} \frac{\partial \rho}{\partial t} &= 0, \\ \frac{\partial s}{\partial t} &= \frac{\beta}{\rho} \Delta T + \frac{\zeta}{\rho T}, \\ \frac{\partial \mathbf{v}}{\partial t} &= \frac{2\mu}{\rho} \nabla \cdot \mathbf{D}_n, \\ \frac{\partial \mathbf{v}_s}{\partial t} &= s \nabla T. \end{aligned} \tag{B20}$$

We will need two additional operators, both of which are well known and established.

Definition 2 (discrete Laplace operator³⁶).

$$\{\Delta \varphi\}_a := 2 \sum_b \frac{m_b w'_{ab}}{\rho_b r_{ab}} \varphi_{ab}. \tag{B21}$$

Definition 3 (Monaghan’s viscosity operator³³).

$$\{\nabla \cdot \mathbf{D}\}_a^M := (d+2) \sum_b \frac{m_b \mathbf{v}_{n,ab} \cdot \mathbf{r}_{ab}}{\rho_b r_{ab}^2 + \eta^2}. \tag{B22}$$

In analogy to (B18), we define

Definition 4 (dissipation duals).

$$\{|\nabla \varphi|^2\}_a := - \sum_b \frac{m_b w'_{ab}}{\rho_b r_{ab}} (\varphi_{ab})^2, \tag{B23}$$

$$\{|\mathbf{D}|^2\}_a^M := - \frac{d+2}{2} \sum_b \frac{m_b (\mathbf{v}_{n,ab} \cdot \mathbf{r}_{ab})^2 w'_{ab}}{\rho_b r_{ab}^2 + \eta^2} \frac{1}{r_{ab}} \tag{B24}$$

such that

Proposition 3.

$$\sum_a \frac{m_a}{\rho_a} \{\Delta \varphi\}_a \varphi_a = - \sum_a \frac{m_a}{\rho_a} \{|\nabla \varphi|^2\}_a, \tag{B25}$$

$$\sum_a \frac{m_a}{\rho_a} \mathbf{v}_{n,a} \cdot \{\nabla \cdot \mathbf{D}\}_a^M = - \sum_a \frac{m_a}{\rho_a} \{|\mathbf{D}|^2\}_a^M. \tag{B26}$$

Now, we are able to write the discrete irreversible part of dynamics as follows:

$$\begin{aligned} \dot{\rho}_a &= 0, \\ \dot{s}_a &= \frac{\beta}{\rho_a} \{\Delta T\}_a + \frac{\zeta_a}{T_a \rho_a}, \\ \dot{\mathbf{v}}_a &= \frac{2\mu}{\rho_a} \{\nabla \cdot \mathbf{D}\}_a^M, \\ \dot{\mathbf{v}}_{s,a} &= 0, \end{aligned} \tag{B27}$$

where

$$\zeta_a = \beta \{|\nabla T|^2\}_a + 2\mu \{|\mathbf{D}|^2\}_a^M. \tag{B28}$$

This gives the remaining irreversible component of (B19).

Proposition 4 (conservation laws—irreversible part). Solution of irreversible equations (B27) and (B28) satisfies conservation of energy

$$\frac{d}{dt} \left(\sum_a m_a e_a \right) = 0, \tag{B29}$$

momentum

$$\frac{d}{dt} \left(\sum_a m_a \mathbf{v}_a \right) = 0, \tag{B30}$$

and angular momentum

$$\frac{d}{dt} \left(\sum_a m_a \mathbf{r}_a \times \mathbf{v}_a \right) = 0. \tag{B31}$$

Also, it satisfies entropic inequality:

$$\frac{d}{dt} \left(\sum_a m_a s_a \right) \geq 0. \tag{B32}$$

Proof. Energy conservation law follows immediately from

$$\dot{e}_a = \mathbf{v}_{n,a} \cdot \dot{\mathbf{v}}_a - \chi_{s,a} \mathbf{v}_{n,s,a} \cdot \mathbf{d}\mathbf{v}_{s,a} + \frac{P_a}{\rho_a^2} \dot{\rho}_a + T_a \dot{s}_a, \tag{B33}$$

Eqs. (B27), and the duality relationships (B25) and (B26). As in classical SPH method for Navier–Stokes equations, conservation of momentum follows from

$$\sum_a \frac{m_a}{\rho_a} \{\nabla \cdot \mathbf{D}\}_a^M = 2(d+2) \sum_{a,b} \frac{m_a m_b \mathbf{v}_{n,ab} \cdot \mathbf{r}_{ab}}{\rho_a \rho_b r_{ab}^2 + \eta^2} \nabla_{ab} w = 0 \tag{B34}$$

(the summand is anti-symmetric in a, b). Similarly, conservation of angular momentum is obtained from

$$\begin{aligned} \sum_a \frac{m_a}{\rho_a} \mathbf{r}_a \times \{\nabla \cdot \mathbf{D}\}_a^M \\ = 2(d+2) \sum_{a,b} \frac{m_a m_b \mathbf{v}_{n,ab} \cdot \mathbf{r}_{ab}}{\rho_a \rho_b r_{ab}^2 + \eta^2} (\mathbf{r}_{ab} \times \nabla_{ab} w) \\ = 0. \end{aligned} \tag{B35}$$

Same technique can be used to show that

$$\sum_a m_a \frac{\beta}{\rho_a} \{\Delta T\}_a = 0. \tag{B36}$$

Since w'_{ab} is always non-positive, $\zeta_a \geq 0$ for every a . Therefore, we obtain the entropic inequality. □

REFERENCES

- ¹J. F. Allen and H. Jones, “New phenomena connected with heat flow in helium II,” *Nature* **141**(3562), 243–244 (1938).
- ²M. L. Amigó, T. Herrera, L. Neñer, L. Peralta Gavensky, F. Turco, and J. Luzuriaga, “A quantitative experiment on the fountain effect in superfluid helium,” *Eur. J. Phys.* **38**(5), 055103 (2017).
- ³C. F. Barenghi, L. Skrbek, and K. R. Sreenivasan, “Introduction to quantum turbulence,” *Proc. Natl. Acad. Sci. U. S. A.* **111**, 4647–4652 (2014).
- ⁴C. F. Barenghi, *Introduction to Superfluid Vortices and Turbulence* (Springer, Berlin/Heidelberg, 2001).
- ⁵I. L. Bekarevich and I. M. Khalatnikov, “Phenomenological derivation of the equations of vortex motion in He II,” *Sov. Phys. JETP* **13**(3), 67 (1961).
- ⁶R. J. Donnelly and C. F. Barenghi, “The observed properties of liquid helium at the saturated vapor pressure,” *J. Phys. Chem. Ref. Data* **27**(6), 1217–1274 (1998).

- ⁷I. E. Dzyaloshinskii and G. E. Volovick, "Poisson brackets in condensed matter physics," *Ann. Phys.* **125**(1), 67–97 (1980).
- ⁸P. Español and M. Revenga, "Smoothed dissipative particle dynamics," *Phys. Rev. E* **67**, 026705 (2003).
- ⁹J. Evans and T. Hughes, "Isogeometric divergence-conforming B-splines for the steady Navier-Stokes equations," *J. Comput. Phys.* **241**, 141–167 (2013).
- ¹⁰L. Galantucci, A. W. Baggaley, C. F. Barenghi, and G. Krstulovic, "A new self-consistent approach of quantum turbulence in superfluid helium," *Eur. Phys. J. Plus* **135**(7), 547 (2020).
- ¹¹F. Gay-Balmaz and T. S. Ratiu, "The geometric structure of complex fluids," *Adv. Appl. Math.* **42**(2), 176–275 (2009).
- ¹²U. Ghia, K. N. Ghia, and C. T. Shin, "High-Re solutions for incompressible flow using the Navier-Stokes equations and a multigrid method," *J. Comput. Phys.* **48**(3), 387–411 (1982).
- ¹³G. Greenstein, "Superfluid turbulence in neutron stars," *Nature* **227**(5260), 791 (1970).
- ¹⁴A. Guthrie, S. Kafanov, M. T. Noble, Y. A. Pashkin, G. R. Pickett, V. Tsepelin, A. A. Dorofeev, V. A. Krupenin, and D. E. Presnov, "Nanoscale real-time detection of quantum vortices at millikelvin temperatures," *Nat. Commun.* **12**(1), 2645 (2021).
- ¹⁵H. E. Hall, W. F. Vinen, and D. Shoenberg, "The rotation of liquid helium II. The theory of mutual friction in uniformly rotating helium II," *Proc. R. Soc. London, Ser. A* **238**(1213), 215–234 (1956).
- ¹⁶H. London, "Thermodynamics of the thermomechanical effect of liquid He II," *Proc. R. Soc. London, Ser. A* **171**, 484–496 (1939).
- ¹⁷D. D. Holm, *Introduction to HVBK Dynamics* (Springer, Berlin/Heidelberg, 2001), pp. 114–130.
- ¹⁸D. D. Holm and B. A. Kupersmidt, "Superfluid plasmas: Multivelocit nonlinear hydrodynamics of superfluid solutions with charged condensates coupled electromagnetically," *Phys. Rev. A* **36**, 3947–3956 (1987).
- ¹⁹R. Hänninen and A. W. Baggaley, "Vortex filament method as a tool for computational visualization of quantum turbulence," *Proc. Natl. Acad. Sci.* **111**, 4667–4674 (2014).
- ²⁰T. Kamppinen and V. B. Eltsov, "Nanomechanical resonators for cryogenic research," *J. Low Temp. Phys.* **196**(1–2), 283–292 (2019).
- ²¹I. M. Khalatnikov, *An Introduction to the Theory of Superfluidity* (Avalon Publishing, 1989).
- ²²T. W. B. Kibble, "Topology of cosmic domains and strings," *J. Phys. A* **9**(8), 1387–1398 (1976).
- ²³O. Kincl and M. Pavelka, "Globally time-reversible fluid simulations with smoothed particle hydrodynamics," *Comput. Phys. Commun.* **284**, 108593 (2023).
- ²⁴K. Kolatzki, M. L. Schubert, A. Ulmer, T. Müller, D. Rupp, and R. M. P. Tanyag, "Micrometer-sized droplets from liquid helium jets at low stagnation pressures," *Phys. Fluids* **34**(1), 012002 (2022).
- ²⁵M. La Mantia, "Particle dynamics in wall-bounded thermal counterflow of superfluid helium," *Phys. Fluids* **29**(6), 065102 (2017).
- ²⁶M. La Mantia, P. Svancara, D. Duda, and L. Skrbek, "Small-scale universality of particle dynamics in quantum turbulence," *Phys. Rev. B* **94**(18), 184512 (2016).
- ²⁷L. Landau, "Theory of the superfluidity of helium II," *Phys. Rev.* **60**, 356–358 (1941).
- ²⁸L. D. Landau and E. M. Lifshitz, *Statistical Physics, Part 1 in Course of Theoretical Physics* (Pergamon Press, 1969).
- ²⁹L. D. Landau and E. M. Lifshitz, *Fluid Mechanics* (Elsevier Science, 2013).
- ³⁰P. Lebrun and L. Tavian, "Cooling with superfluid helium," [arXiv:1501.07156](https://arxiv.org/abs/1501.07156) (2015).
- ³¹S. J. Lind, B. D. Rogers, and P. K. Stansby, "Review of smoothed particle hydrodynamics: Towards converged Lagrangian flow modelling," *Proc. R. Soc. A* **476**(2241), 20190801 (2020).
- ³²S. J. Lind, R. Xu, P. K. Stansby, and B. D. Rogers, "Incompressible smoothed particle hydrodynamics for free-surface flows: A generalised diffusion-based algorithm for stability and validations for impulsive flows and propagating waves," *J. Comput. Phys.* **231**(4), 1499–1523 (2012).
- ³³J. J. Monaghan, "Smoothed particle hydrodynamics," *Annu. Rev. Astron. Astrophys.* **30**(1), 543–574 (1992).
- ³⁴J. J. Monaghan, H. E. Huppert, and M. G. Worster, "Solidification using smoothed particle hydrodynamics," *J. Comput. Phys.* **206**(2), 684–705 (2005).
- ³⁵M. S. Mongioli, D. Jou, and M. Sciacca, "Non-equilibrium thermodynamics, heat transport and thermal waves in laminar and turbulent superfluid helium," *Phys. Rep.* **726**, 1–71 (2018).
- ³⁶J. P. Morris, P. J. Fox, and Y. Zhu, "Modeling low Reynolds number incompressible flows using SPH," *J. Comput. Phys.* **136**(1), 214–226 (1997).
- ³⁷G. Oger, M. Doring, B. Alessandrini, and P. Ferrant, "An improved SPH method: Towards higher order convergence," *J. Comput. Phys.* **225**(2), 1472–1492 (2007).
- ³⁸O. Outrata, M. Pavelka, J. Hron, M. La Mantia, J. I. Polanco, and G. Krstulovic, "On the determination of vortex ring vorticity using Lagrangian particles," *J. Fluid Mech.* **924**, A44 (2021).
- ³⁹S. J. Putterman, *Superfluid Hydrodynamics* (North Holland, Amsterdam, 1974).
- ⁴⁰B. Rousset, P. Bonnaud, P. Diribarne, A. Girard, J. M. Poncet, E. Herbert, J. Salort, C. Baudet, B. Castaing, L. Chevillard, F. Daviaud, B. Dubrulle, Y. Gagne, M. Gibert, B. Hébral, T. Lehner, P. E. Roche, B. Saint-Michel, and M. Bon Mardion, "Superfluid high Reynolds von Karman experiment," *Rev. Sci. Instrum.* **85**(10), 103908 (2014).
- ⁴¹J. Salort, C. Baudet, B. Castaing, B. Chabaud, F. Daviaud, T. Didelot, P. Diribarne, B. Dubrulle, Y. Gagne, F. Gauthier, A. Girard, B. Hébral, B. Rousset, P. Thibault, and P. E. Roche, "Turbulent velocity spectra in superfluid flows," *Phys. Fluids* **22**(12), 125102 (2010).
- ⁴²H. Sanavandi, S. Bao, Y. Zhang, R. Keijzer, W. Guo, and L. N. Cattafesta, III, "A cryogenic-helium pipe flow facility with unique double-line molecular tagging velocimetry capability," *Rev. Sci. Instrum.* **91**, 053901 (2020).
- ⁴³D. Schmoranzler, M. J. Jackson, S. Midlik, M. Skyba, J. Bahyl, T. Skokankova, V. Tsepelin, and L. Skrbek, "Dynamical similarity and instabilities in high-Stokes-number oscillatory flows of superfluid helium," *Phys. Rev. B* **99**(5), 054511 (2019).
- ⁴⁴J. Schumacher and K. R. Sreenivasan, "Colloquium: Unusual dynamics of convection in the Sun," *Rev. Mod. Phys.* **92**(4), 041001 (2020).
- ⁴⁵S. Shukla, A. K. Verma, V. Shukla, A. Bhatnagar, and R. Pandit, "Inertial particles in superfluid turbulence: Coflow and counterflow," *Phys. Fluids* **35**(1), 015153 (2023).
- ⁴⁶V. Shukla, R. Pandit, and M. Brachet, "Particles and fields in superfluids: Insights from the two-dimensional Gross-Pitaevskii equation," *Phys. Rev. A* **97**, 013627 (2018).
- ⁴⁷L. Skrbek, D. Schmoranzler, S. Midlik, and K. R. Sreenivasan, "Phenomenology of quantum turbulence in superfluid helium," *Proc. Natl. Acad. Sci. U. S. A.* **118**(16), e2018406118 (2021).
- ⁴⁸A. Henderson Squillacote, J. Ahrens, C. Law, B. Geveci, K. Moreland, and B. King, *The Paraview Guide* (Kitware, Clifton Park, NY, 2007), Vol. 366.
- ⁴⁹C. F. Squire, *Macroscopic Theory of Superfluid Helium*, *Superfluids* (Wiley/Chapman & Hall, New York/London, 1954), Vol. 2; *Science* **121**(3146), 554–555 (1955).
- ⁵⁰M. Šykora, M. Pavelka, M. La Mantia, D. Jou, and M. Grmela, "On the relations between large-scale models of superfluid helium-4," *Phys. Fluids* **33**(12), 127124 (2021).
- ⁵¹L. Tisza, "Transport phenomena in helium II," *Nature* **141**(3577), 913–913 (1938).
- ⁵²J. T. Tough, *Progress in Low Temperature Physics* (North-Holland Publ. Co., 1982), Vol. 8.
- ⁵³M. Tsubota, K. Fujimoto, and S. Yui, "Numerical studies of quantum turbulence," *J. Low Temp. Phys.* **188**(5), 119–189 (2017).
- ⁵⁴S. Tsuzuki, "Particle approximation of the two-fluid model for superfluid 4He using smoothed particle hydrodynamics," *J. Phys. Commun.* **5**(3), 035001 (2021).
- ⁵⁵S. Tsuzuki, "Reproduction of vortex lattices in the simulations of rotating liquid helium-4 by numerically solving the two-fluid model using smoothed-particle hydrodynamics incorporating vortex dynamics," *Phys. Fluids* **33**(8), 087117 (2021).
- ⁵⁶S. Tsuzuki, "Theoretical framework bridging classical and quantum mechanics for the dynamics of cryogenic liquid helium-4 using smoothed-particle hydrodynamics," *Phys. Fluids* **34**(12), 127116 (2022).
- ⁵⁷S. W. Van Sciver, *Helium Cryogenics*, International Cryogenics Monograph Series (Springer, New York, 2012).
- ⁵⁸D. Violeau, *Fluid Mechanics and the SPH Method: Theory and Applications* (Oxford University Press, Oxford, UK, 2012).

- ⁵⁹G. E. Volovik, "Poisson bracket scheme for vortex dynamics in superfluids and superconductors and the effect of the band structure of the crystal," *J. Exp. Theor. Phys. Lett.* **64**(11), 845–852 (1996).
- ⁶⁰G. E. Volovik and V. S. Dotsenko, Jr., "Poisson brackets and continuous dynamics of the vortex lattice in rotating He II," *JETP Lett.* **29**(10), 5 (1979).
- ⁶¹G. E. Volovik and V. S. Dotsenko, Jr., "Hydrodynamics of defects in condensed media, using as examples vortices in rotating He II and disclinations in a planar magnet," *Sov. Phys.-JETP* **51**(1), 65 (1980).
- ⁶²G. E. Volovik, *The Universe in a Helium Droplet*, International Series of Monographs on Physics (OUP, Oxford, 2009).
- ⁶³X. Yang and S.-C. Kong, "Smoothed particle hydrodynamics method for evaporating multiphase flows," *Phys. Rev. E* **96**(3), 033309 (2017).
- ⁶⁴P. R. Zilsel, "Liquid helium II: The hydrodynamics of the two-fluid model," *Phys. Rev.* **79**, 309–313 (1950).
- ⁶⁵W. H. Zurek, "Cosmological experiments in superfluid-helium," *Nature* **317**(6037), 505–508 (1985).